Nonlinear Rock Mass Behaviour and Application to Stability of Underground Haulage Drift

by

Yaohua Zhang, B.Eng.

A thesis submitted to the
Graduate and Postdoctoral Studies Office
in partial fulfilment of the requirements
for the Degree of Master of Engineering

Department of Mining, Metals and Materials Engineering

McGill University

Montreal, Quebec, Canada

March, 2006

Your file Votre référence
ISBN: 978-0-494-25022-8
Our file Notre référence
ISBN: 978-0-494-25022-8

Abstract

Numerical methods of analysis such as the finite element method and finite difference method have seen increasing use in recent years as tools for geomechanical mine design to predict problems of ground caving and failure. As a result of recent advances in computer technology, it is now possible to handle large-scale problems involving complex material and geometric nonlinearities at an affordable computational cost. The scope of this study is the stability of underground mine haulage drifts associated with sublevel stoping method with delayed backfill. This is one of the most popular mining methods today in Canadian underground metal mines. In this method, blasted ore is mucked with load-haul-dump vehicles and transported to the nearest dump through a nearby haulage drift. Therefore, it is crucial in a mining operation that a haulage drift remains functional during the life of the stope.

This study is focused on studying the interaction between the haulage drift and nearby mining activity. The stability of the haulage drift is examined through a detailed parametric study of a finite element model representing typical mining layout most commonly adopted in Canadian underground metal mines. The model parametric study examines the influence of critical factors such as the stope mining sequences, mining depth and the distance between the stope and the haulage drift. The model is set up for nonlinear behaviour of the rock mass taking into account elastoplasticity of the rock mass and non-associated plasticity using Mohr Coulomb and Drucker Prager yield functions. Stability indicators are defined in terms of displacement, stress and the extent of yield zones. These indicators serve as a basis for assessing the effect of different parameters on the stability of the haulage drift.

From the model parametric study, it is found that stope mining causes a lateral movement of the entire drift. The severity of such movement is increased with shorter distance between the stope and haulage drift. Of all mining sequences examined, same-level mining is the most critical step. It is also found that more yield zones develop around the

haulage drift as the mining depth increases and as distance between haulage drift and the stope decreases.

A 3-centre arc drift is compared with a rectangular one of the same cross sectional area. It is found that the 3-centre arc drift shape is more stable. This study also demonstrates that the nonlinear elastoplastic analysis gives more realistic results than traditional linear elastic analysis in terms of stress and displacement behaviour of the haulage drift.

Résumé

Au cours des dernières années, les méthodes numériques telles que les éléments finis et les différences finies ont connu un intérêt croissant dans le domaine de la géomécanique appliquée aux mines, spécialement pour la prédiction des problèmes de « caving » et de rupture. Grâce aux capacités des dernières générations d'ordinateurs, il est désormais possible d'analyser des problèmes de grande taille impliquant des matériaux complexes et des géométries non linéaires. Le sujet de cette recherche est l'étude de la stabilité de galeries de transport (haulage drift) des mines souterraines associée aux méthodes d'abatage de sous niveau avec du remblai. Actuellement, cette méthode est une des plus utilisées dans les mines de sulfures souterraines canadiennes. Dans cette méthode, le minerai préalablement dynamité est déblayé avec des véhicules de type « load-haul-dump » et transporté jusqu'à la zone de décharge par la conduite de halage la plus proche.

Cette étude s'intéresse, plus particulièrement, aux interactions entre la galerie de transport et les zones d'activités minières avoisinantes. La stabilité de la galerie de transport est examinée grâce à une étude paramétrique détaillée d'un modèle en éléments finis représentant une conduite typique des mines de sulfures souterraines au Canada. Le modèle synthétique permet d'examiner l'influence des paramètres critiques tels que la séquence de chantier d'abatage, la profondeur de la mine et la distance entre le chantier d'abatage et la galerie de transport. Le modèle utilisé est un modèle non linéaire prenant en compte les propriétés élasto-plastiques de la roche et la plasticité non associée. Ce modèle utilise les fonctions de rupture de Mohr-Coulomb et de Drucker-Prager. Les indices de stabilité sont définis en termes de déplacement, de contraintes et d'extension de la zone plastique. Ces indices permettent de quantifier les effets des différents paramètres sur la conduite de halage.

Grâce au modèle synthétique, il a été démontré que l'exploitation d'un chantier d'abatage provoque un mouvement latéral de la galerie de transport tout entière. La sévérité du déplacement est amplifiée plus la distance entre la stope et la galerie de transport est courte. De toutes les séquences de minage étudiées, l'exploitation au même niveau est la

plus critique. Il a été démontré que les zones plastiques sont plus nombreuses si la profondeur de la mine est grande et si la distance entre la stope et la conduite de halage est petite.

Une galerie de transport de type « 3-centre arcs » est comparée avec une galerie à section rectangulaire de surface équivalente. Il est démontré que la galerie de transport de type « 3-centre arcs » est plus stable. Cette étude démontre aussi que la modélisation par un modèle non linéaire élasto-plastique donne des résultats plus réalistes que les modèles linéaires élastiques, en termes de contraintes et de déplacement de la conduite de halage.

Acknowledgement

I wish to express my sincere appreciation to my supervisor, Professor Hani S. Mitri, for his endless encouragement, support and guidance throughout my studies. I wish to thank my colleague Xiaoyou Yun for his encouragement and the many technical discussions that we have had during my study. Thanks also give to Dr. Erwan Gloaguen for his help to translate the *Abstract* of this thesis into French. Last but not least, I am very grateful to my dear wife, Yan Ding, who has been extremely supportive throughout my graduate studies.

Table of Contents

List of Figures

List of Tables

Nomenclature

A zero order in tensor notation, scalar in matrix notation

A_i first order in tensor notation

A_{ij} second order in tensor notation

$\{A\}$ column vector in matrix notation

$\{A\}^T$ row vector in matrix notation

$[A]$ matrix or row vector in matrix notation

$[A]^T$ transpose matrix in matrix notation

$[A]^{-1}$ inverse matrix in matrix notation

σ stress

σ_{ij} stress at plane i in the direction of j

if i=j, σ_{ii} is normal stress, and $\sigma_{xx}=\sigma_x$, $\sigma_{yy}=\sigma_y$, $\sigma_{zz}=\sigma_z$

if i≠j, σ_{ij} is shear stress, and $\sigma_{ij}=\tau_{ij}$

τ_{ij} shear stress

σ_1, σ_2, σ_3 major, intermediate, and minor principal stress, respectively

σ_m mean stress or hydrostatic stress

$$\sigma_m = \frac{1}{3} J_1$$

s_{ij} deviatoric stress at plane i in the direction of j

$$s_{ij} = \sigma_{ij} - \sigma_m$$

$\bar{\sigma}$ deviatoric stress in triaxial test

θ Lode angle in Mohr-Coulomb model

σ_Y yield strength

σ_c uniaxial compressive strength of intact rock (UCS)

σ_{bc} uniaxial compressive strength of rock mass

σ^0 initial stress

σ_t tensile strength

ε	strain
ε_{ij}	stain at plane i in the direction of j
	if i=j, $\varepsilon_{xx}=\varepsilon_x$, $\varepsilon_{yy}=\varepsilon_y$, $\varepsilon_{zz}=\varepsilon_z$
	if i≠j, $\varepsilon_{ij}=\frac{1}{2}\gamma_{ij}$
γ_{ij}	engineering shear strain
ε_1, ε_2, ε_3	major, intermediate, and minor principal strain, respectively
ε^0	initial strain
ε_V	volumetric strain
	$\varepsilon_v = \varepsilon_x + \varepsilon_y + \varepsilon_z$
ε^e	elastic strain
ε^p	plastic strain
$d\varepsilon$	strain increment
$d\varepsilon^e$	elastic strain increment
$d\varepsilon^p$	plastic strain increment
$d\varepsilon_V$	volumetric strain increment
$\dot{\varepsilon}$	strain rate
$\Delta\varepsilon^{vp}$	accumulated viscoplastic strain
ε_m	mean strain
e_{ij}	deviatoric strain
	$e_{ij} = \varepsilon_{ij} - \varepsilon_m$
E	Young's modulus
ν	Poison's ratio
γ	material specific gravity
ρ	material density
G	shear modulus

$$G = \frac{E}{2(1+\nu)}$$

K bulk modulus

$$K = \frac{E}{3(1-2\nu)}$$

Λ Lame's constant

$$\Lambda = \nu E \big/ (1+\nu)(1-2\nu)$$

ϕ angle of internal friction

c cohesion

ψ dilation angle

α, k material constants of Drucker-Prager yield function

α_Q, k_Q material constants of Drucker-Prager plastic potential function

m, s, a material constants of Hoek-Brown failure criterion

m_i intact rock material constant of Hoek-Brown failure criterion

m_b broken rock material constant of Hoek-Brown failure criterion

RMR Rock Mass Rating

GSI Geological Strength Index

D disturbance factor of Hoek-Brown failure criterion

F yield function

F_{TC} yield function in the state of triaxial compression for Drucker-Prager model

F_{TE} yield function in the state of triaxial extension for Drucker-Prager model

Q plastic potential function

λ hardening/softening parameter or plastic multiplier

[D] constitutive matrix

[C] compliance of constitutive matrix

$[C] = [D]^{-1}$

$[D_t]$ trajectory dependent constitutive matrix

$[D^e]$ elastic constitutive matrix

$[D^p]$ plastic constitutive matrix

$[D^{ep}]$ elastoplastic constitutive matrix

$[J]$ Jacobian matrix

$X_i / x_i, Y_i / y_i$ coordinates in global system at node i

ξ, η coordinates in local system

N / N_i shape function

$[k^e]$ element stiffness matrix

$[K]$ global stiffness matrix

$[B]$ strain-displacement matrix

u, v displacement in x, y direction, respectively

$\{d\}$ generalized displacement vector

$\{\Delta d\}$ vector of displacement increments

$\{F\}/\{f\}/\{P\}$ load vector

$\{\Delta F\}/\{\Delta f\}$ vector of load increments

nip total integration points

W_i / W_j wighting factor of sampling point

Δt time step

ΔR imbalanced force or load

r^{int} internal force

J_1 first invariant of stress tensor

$$J_1 = \sigma_{ii} = \sigma_x + \sigma_y + \sigma_z = tr(\sigma) = \sigma_1 + \sigma_2 + \sigma_3$$

J_2 second invariant of stress tensor

$$J_2 = \frac{1}{2}(\sigma_{ii}\sigma_{jj} - \sigma_{ij}\sigma_{ji})$$
$$= \sigma_x\sigma_y + \sigma_y\sigma_z + \sigma_z\sigma_x - (\tau_{xy}^2 + \tau_{yz}^2 + \tau_{zx}^2)$$
$$= \sigma_1\sigma_2 + \sigma_2\sigma_3 + \sigma_3\sigma_1$$

J_3 third invariant of stress tensor

$$J_3 = \frac{1}{3}\sigma_{ij}\sigma_{jk}\sigma_{ki} = \frac{1}{3}tr(\sigma)^3$$
$$= \sigma_x\sigma_y\sigma_z + \sigma_{xy}\sigma_{yz}\sigma_{zx} + \sigma_{yx}\sigma_{zy}\sigma_{xz}$$
$$- (\sigma_x\sigma_{yz}\sigma_{zy} + \sigma_y\sigma_{zx}\sigma_{xz} + \sigma_z\sigma_{xy}\sigma_{yx})$$
$$= \sigma_1\sigma_2\sigma_3$$

J_{1D} first invariant of deviatoric stress tensor

$J_{1D} = 0$

J_{2D} second invariant of deviatoric stress tensor

$$J_{2D} = \tfrac{1}{6}[(\sigma_x - \sigma_y)^2 + (\sigma_y - \sigma_z)^2 + (\sigma_z - \sigma_x)^2] + \tau_{xy}{}^2 + \tau_{yz}{}^2 + \tau_{zx}{}^2$$

or

$$J_{2D} = \tfrac{1}{6}[(\sigma_1 - \sigma_2)^2 + (\sigma_2 - \sigma_3)^2 + (\sigma_3 - \sigma_1)^2]$$

J_{3D} third invariant of deviatoric stress tensor

$$J_{3D} = \frac{1}{3}s_{ij}s_{jk}s_{ki} = \frac{1}{3}tr(s)^3$$
$$= \frac{1}{3}(\sigma_{ij} - \sigma_m\delta_{ij})(\sigma_{jk} - \sigma_m\delta_{ij})(\sigma_{ki} - \sigma_m\delta_{ij})$$
$$= J_3 - \frac{2}{3}J_1J_2 + \frac{2}{27}J_1^3$$
$$= (\sigma_x - \sigma_m)(\sigma_y - \sigma_m)(\sigma_z - \sigma_m) + 2\tau_{xy}\tau_{yz}\tau_{zx}$$
$$- (\sigma_x - \sigma_m)\tau_{yz}^2 - (\sigma_y - \sigma_m)\tau_{zx}^2 - (\sigma_z - \sigma_m)\tau_{xy}^2$$

δ_{ij} Kronecker delta

$$\delta_{ij} = \begin{cases} 1 & when \quad i = j \\ 0 & when \quad i \neq j \end{cases}$$

σ_v vertical in situ stress

σ_h	horizontal in situ stress (average)
$\sigma_{H\max}$	maximum horizontal in situ stress
$\sigma_{H\min}$	minimum horizontal in situ stress
H	overburden depth
D	distance between stope and haulage drift
W	stope width
k	the ratio of horizontal stress to vertical stress $k = {}^{\sigma_h}\!/_{\sigma_v}$
SCF	stress concentration factor
WCR	wall convergence ratio
RSR	roof sag ratio
FHR	floor heave ratio

Chapter 1 Introduction

1.1 General

Many Canadian metal mines have adopted sublevel stoping method or one of its variations, such as blasthole stoping and vertical crater retreat, for the extraction of deeply stipping orebodies. The Canadian Mining Journal's 2005 Mining Sourcebook reported that 17 out of 23 underground metal mines use sublevel stoping methods. In sublevel stoping methods, the orebody is mined out in blocks (stopes), which are drilled and blasted in various patterns of long holes. Blasted ore from each block is mucked out with loading equipment and transported to dumps with trucks or load-haul-dump vehicles. These mining methods, also commonly known as long-hole methods have the advantages of safety, high production rate, and high percentage of ore recovery. Mining companies like Inco, Falconbridge, Place Dome, Agnico-Eagle and Cambior have mines where long-hole mining method is adopted.

In sublevel stoping methods, trucks and/or loaders must travel through haulage drifts in order to load the blasted ore from the draw point and transport the ore out of mining zone. As drilling, blasting, and drawing mining activity progresses upwards in stopes, there is less rock mass to support the mine structure and hence the condition of the haulage drift deteriorates. This can be attributed primarily to the stress redistribution caused by the sequenced removal of the ore rock from the stope. Under these conditions, there is a strong possibility that the haulage drift could suffer from one or more types of ground instability.

Haulage drifts are the arteries of a mine as they transport the valuable mineral (blasted ore) to the dump and hence out of the mining zone. Therefore, it is crucial in a mining operation that a haulage drift remains functional at all times. Ground caving in a haulage drift can have serious consequences from injuries to delayed production and increased operational cost.

The factors that may influence the stability of haulage drift are:

- Strength and quality of ore and host rock masses.

- Mining depth. As mines continue to reach deeper deposits, haulage drifts at those depths are expected to experience high pre-mining stress conditions, thus causing more stability problems to haulage drift.

- The distance between the haulage drift and the mining stope is another important factor affecting the stability of the haulage drift. It is known that there exists a trade-off between the stability level (favouring long distance) and mining costs (which favour short distance).

- Mining sequence is a complicated influencing factor to the stability of haulage drift in that different mining sequences will result in different mining-induced stresses, which result from the redistribution of pre-mining or field stresses.

- The dip and thickness of orebody.

- Geometry of the haulage drift.

As is recognized, analytical methods cannot provide solution for complicated mining problems such as the one citied here. At this time, there are no existing empirical methods taking all the important influence factors into account to evaluate the stability of haulage drift.

In recent years, taking advantage of modern computer technology, numerical methods become widely accepted in mine design and feasibility studies. Numerical methods not only have the potential to solve complex mining problems, but also help engineers and researchers to better understand and assess failure mechanisms, estimate geomechanical risks, and design rock support system more effectively.

On the one hand, although linear elastic models provide some helpful results for mine development and support design, they do not give full explanation about the true stress state around underground openings (i.e. resulting stresses are often much higher than rock mass strength), the relatively large displacements, as well as volumetric strains. On the other hand, material elastoplasticity models can make up for the shortcomings of elastic models. There are only a few documented studies which involved comprehensive analysis of the stability of haulage drift responding to mining activities.

The scope of this thesis is the stability of haulage drift during mining activities in the context of sublevel stoping method with delayed backfill, as shown in Figure 1.1. Elaborate elastoplasticity models will be implemented in this study and a fundamental solution to keep the haulage drift safe and functional is yet to be found by taking into account the various influence factors through detailed parametric studies.

1.2 Research objectives

Based on a comprehensive literature review on rock material elastic-plastic behaviour and finite element analysis in rock mechanics and geomechanics, this research will focus on studying the stability of haulage drift influenced by sublevel stoping mining activities. The stability of the haulage drift will be examined through model parametric studies of a finite element model representing typical mining scenario, most commonly adopted in Canadian metal mines. More specifically, the principal objectives of this study are as follows.

- Investigate the application of sublevel stoping method with delayed backfills in Canadian underground mines;
- Delineate the critical parameters of stopes and drifts for each application;
- Build nonlinear characteristic models using elastoplasticity and finite element analysis techniques;
- Perform detailed parametric studies;
- Reveal the most influential parameters on the stress and displacement behaviour of haulage drift.

1.3 Thesis structure

Chapter 1 is an introduction; it describes the study problem as well as the scope and objectives of the study

Chapter 2 reviews the elastic-plastic behaviour of rock materials, plasticity theories and widely used elastoplastic constitutive models in rock mechanics.

Chapter 3 presents the techniques of finite element analysis. The characteristics of finite element equations in mining problems are discussed and algorithms in sequenced mining problems are outlined.

Chapter 4 describes the selected characteristic model for mine haulage drift in sublevel stoping method with delayed backfill. It introduces the sublevel stoping method, and then based on the investigation of sublevel stope and haulage drift parameters adopted in Canadian underground mines, the characteristic models are proposed.

Chapter 5 presents the results of model parametric studies. The effects of different parameters to the stability of haulage drift are investigated.

Chapter 6 summarizes the conclusions of the study. Recommendations for future work are also presented.

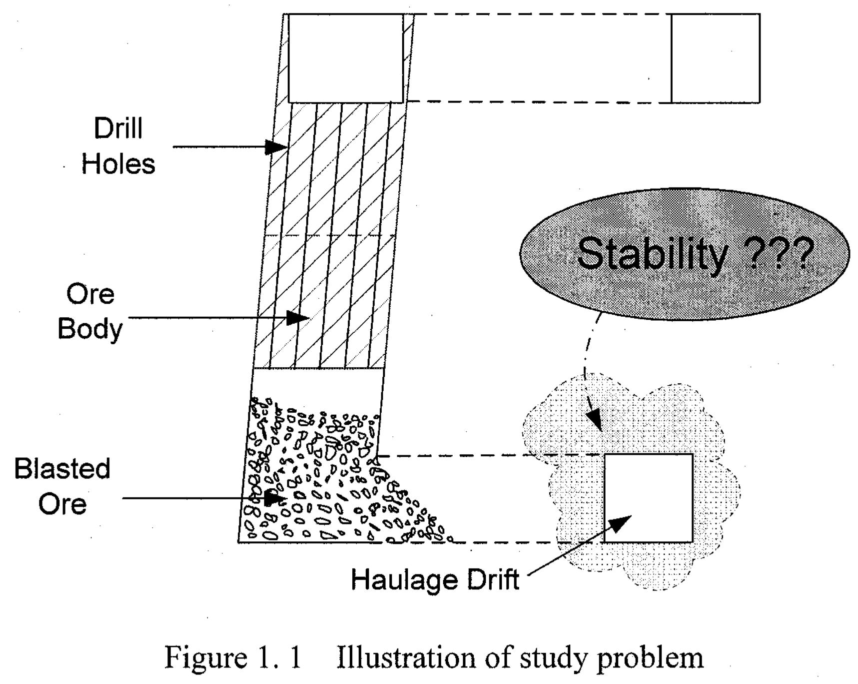

Figure 1. 1 Illustration of study problem

Chapter 2 Elastic-Plastic Behaviour of Rock Material

The behaviour of rock material under different loading conditions can be described in different models such as Mohr-Coulomb model (Coulomb, 1776), Drucker-Prager models (Drucker & Prager, 1952), Hoek-Brown empirical failure criteria (Hoek & Brown, 1980a, 1980b, 1988, 1997; Hoek, Carranza-Torres, & Corkum, 2002; Hoek, Marinos, & Marinos, 2004), semi-empirical failure criterion (Kaiser, Diederichs, Martin, Sharp, & Steiner, 2000), Rock Mass Bulking Model (RMBM) (Gomez-Hernandz & Kaiser, 2003), Single Hardening/Softening Constitutive Model (Lade & Jackobsen, 2002), Cohesion Weakening and Frictional Strengthening Model (CWFS) (Hajiabdolmajid, Kaiser, & Martin, 2002a, 2002b; Hajiabdolmajid & Kaiser, 2003), etc. But the most popular ones to describe elastoplastic behaviour, especially implemented in computer programs, are the first three models, namely Mohr-Coulomb, Drucker-Prager and Hoek-Brown models. Thus, in this chapter, they will be presented in detail.

2.1 General behaviour of rock material

Under different loading conditions and confinements, the rock material may exhibit elastic behaviour; viscous behaviour or plastic behaviour. Also, the behaviour can be classified as linear or nonlinear, partly linear and partly nonlinear, as shown in Figure 2.1. One can divide the response into several characteristic regions which are a result of the following microstructural changes in a rock sample (Carnavas, 2000).

Region I: marked by the closure of pre-existing cracks, manifested in the slightly convex upward path of the axial stress-strain curve.

Region II: characterized by an approximately linear elastic behaviour.

Region III: describing crack growth and sliding on existing crack interfaces, and the occurrence of the first local micro-fractures. The micro-fractures are preferably oriented along the axis through which the load is applied.

Region IV: showing a rapid increase in the microcrack density leading to the failure or ultimate strength of the specimen. The small fractures are built on those cracks which opened as stress rises during region III. These cracks lead to the onset of spalling in the beginning of Region V.

Region V: characterized by the formation of the macroscopic fracture plane. The rapid drop in the load bearing capacity can be attributed to the failure of existing material bridges ahead of the macroscopic failure plane.

Region VI: Sliding along macroscopic fracture planes with increased deterioration and crushing. The result is a loose mass of broken material.

Viscous models can be used to simulate the behaviour of region I, elastic models to simulate the behaviour of region II and III, plastic models and/or viscous models to simulate the behaviour start and after region IV, called post peak behaviour region.

2.1.1 Viscous behaviour of rock material

In general, viscous behaviour, or creep, stands for time-dependent behaviour of rock materials. Soils and weak rocks, such as sedimentary and metamorphic rocks, often exhibit significant viscous behaviours.

For a weak rock material, before the rock material exhibits linear elastic behaviour, it could first experience a viscous process. After yielding, it could experience another stage of viscous behaviour.

For a typical viscous rock material, when it is under viscous phase, we can divide this process into three stages, as shown in Figure 2.2.

2.1.2 Elastic behaviour of rock material

Figure 2.3 shows the elastic behaviour of rock materials: a) represents the linear elastic behaviour of rock materials, in which Hooke's law is the constitutive relation; b) represents the nonlinear elastic behaviour of rock materials, which constitutive relation follows generalized Hooke's law.

2.1.2.1 Hooke's Law

For linear elastic behaviour, on uniaxial loading, the constitutive law can be presented as well-known Hooke's law, expressed as:

$$\sigma = E\varepsilon \tag{2.1}$$

where σ is the stress, ε the strain, and E the Young's modulus, respectively.

2.1.2.2 Generalized Hooke's Law

For three-dimensional bodies, the generalized Hooke's law, or linear elastic constitutive relations can be expressed as (Creus, 1986):

$$\sigma_{ij} = E_{ijkl}\varepsilon_{kl} \tag{2.2}$$

where E_{ijkl} is the forth-order material stiffness tensor.

For isotropic materials, equation (2.2) reduces to

$$\sigma_{ij} = \tfrac{1}{3}\Lambda\varepsilon_v\delta_{ij} + 2G\varepsilon_{ij} \tag{2.3}$$

where Λ is the Lame's constant, G the shear modulus, and ε_v the volumetric strain, respectively.

$$\varepsilon_v = \varepsilon_{ii} = \varepsilon_x + \varepsilon_y + \varepsilon_z \tag{2.4}$$

Equation (2.3) may also be written in the form

$$\sigma_{ij} = \sigma_m\delta_{ij} + s_{ij} \tag{2.5}$$

where σ_m is the mean stress, or spherical components of σ_{ij}, or hydrostatic stress.

$$\sigma_m = \frac{1}{3}\sigma_{ii} = \frac{1}{3}(\sigma_x + \sigma_y + \sigma_z) \tag{2.6}$$

s_{ij} is the deviatoric components of σ_{ij}, $s_{ij} = 2Ge_{ij}$,

e_{ij} is the deviatoric strain tensor,

δ_{ij} is the Kronecker delta.

In finite element analysis, these constitutive relations are often written in matrix form

$$\{\sigma\} = [D]\ \{\varepsilon\} \tag{2.7}$$

where

$$\{\sigma\} = \{\sigma_x, \sigma_y, \sigma_z, \tau_{xy}, \tau_{yx}, \tau_{zx}\} \tag{2.8}$$

$$\{\varepsilon\} = \{\varepsilon_x, \varepsilon_y, \varepsilon_z, \gamma_{xy}, \gamma_{yz}, \gamma_{zx}\} \tag{2.9}$$

[D] is the material constitutive matrix;

τ_{ij} are sheer stresses;

γ_{ij} are engineering sheer strains.

$$[D]=\frac{E}{(1+\nu)(1-2\nu)}\begin{vmatrix} 1-\nu & \nu & \nu & 0 & 0 & 0 \\ \nu & 1-\nu & \nu & 0 & 0 & 0 \\ \nu & \nu & 1-\nu & 0 & 0 & 0 \\ 0 & 0 & 0 & \frac{1}{2}(1-2\nu) & 0 & 0 \\ 0 & 0 & 0 & 0 & \frac{1}{2}(1-2\nu) & 0 \\ 0 & 0 & 0 & 0 & 0 & \frac{1}{2}(1-2\nu) \end{vmatrix} \tag{2.10}$$

where v is the Poison's ratio.

For the plane stress case:

$$[D]=\frac{E}{1-\nu^2}\begin{vmatrix} 1 & \nu & 0 \\ \nu & 1 & 0 \\ 0 & 0 & \frac{1-\nu}{2} \end{vmatrix} \tag{2.11}$$

For the plane strain case:

$$[D] = \frac{E}{(1+\nu)(1-2\nu)} \begin{vmatrix} 1-\nu & \nu & 0 \\ \nu & 1-\nu & 0 \\ 0 & 0 & \frac{1-2\nu}{2} \end{vmatrix} \tag{2.12}$$

In general, for nonlinear elastic material, the constitutive law can be expressed as:

$$\sigma_{ij} = f_{ij}(\varepsilon_{kl}) \tag{2.13}$$

or incremental form

$$\{d\sigma_{ij}\} = [D_t]\,\{d\varepsilon_{ij}\} \tag{2.14}$$

where f_{ij} are material response functions, $[D_t]$ is stress trajectory-dependent constitutive matrix.

If we take into account initial stress and initial strain, equation (2.7) will become

$$\{\sigma\} = [D]\,(\{\varepsilon\}-\{\varepsilon^0\})+\left\{\sigma^0\right\} \tag{2.15}$$

where $\left\{\sigma^0\right\}$, $\{\varepsilon^0\}$ are initial stress and initial strain tensors, respectively. In underground mining 2-dimentional problems, usually $\{\varepsilon^0\}=0$, $\left\{\sigma^0\right\}$ mainly comes from in situ stresses and gravity, called gravity induced stress.

2.1.3 Plastic behaviour of rock material

For plastic behaviour, it can be further divided as perfectly plastic behaviour, hardening behaviour, and softening behaviour. Many hard rocks in Canadian shields, i.e. basalt, granite, andesite, rhyolite, present predominant elastoplastic behaviour. These are the focus of this research project and will be elaborated in the following sections.

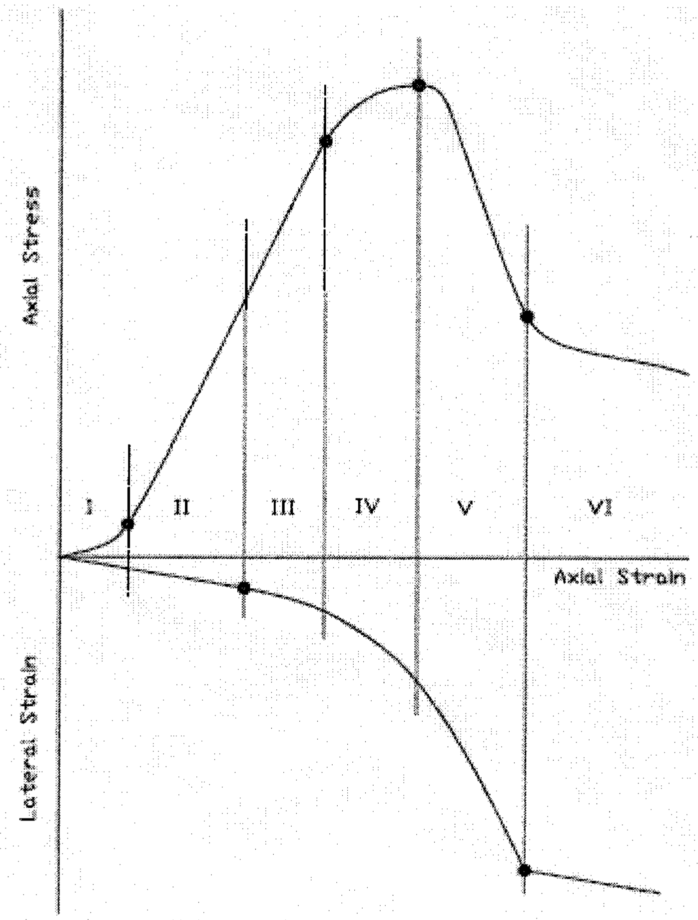

Figure 2. 1 Ideal, complete axial stress-strain curve for uniaxial compression of rock materials (Hallbauer, Wagner, & Cook, 1973)

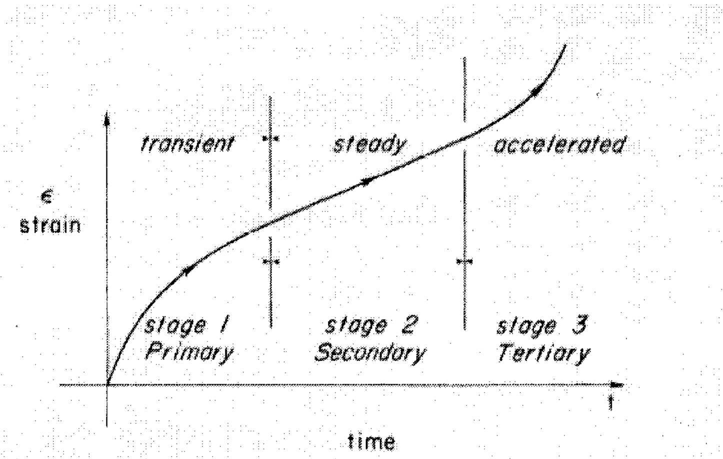

Figure 2. 2 Three stages of viscous process (Pariseau, 1992a)

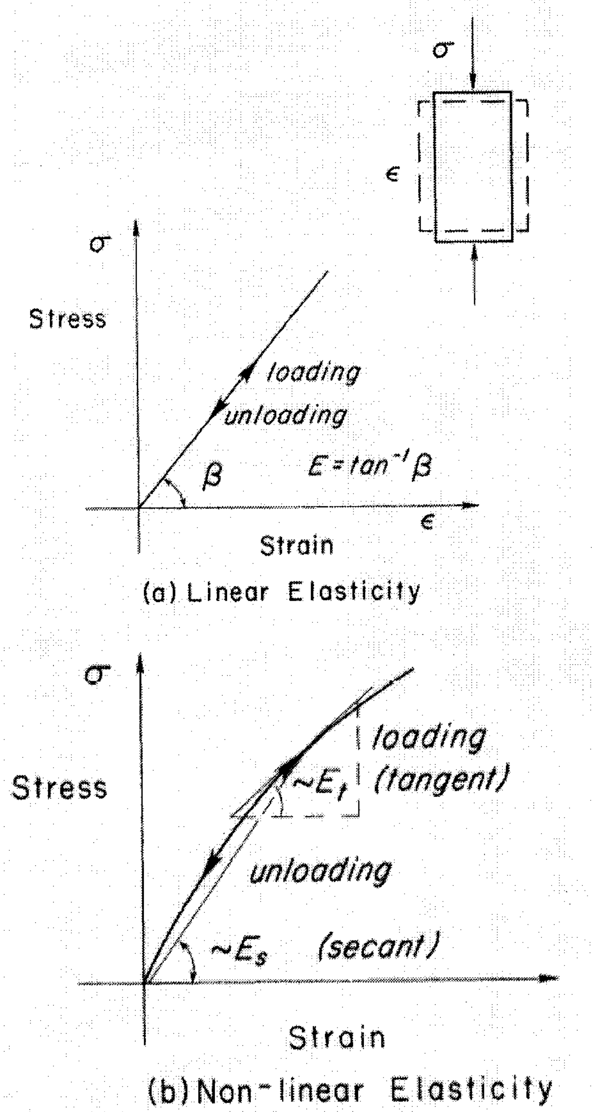

Figure 2. 3 Elastic Behaviour of Rock Materials (Pariseau, 1992b)

2.2 Plasticity theory

In general, a classical plastic theory includes three main components: (1) yield function, represented by one or more surfaces, called yield surfaces, in stress space, most commonly described in the principal stress space and /or π plane; (2) hardening/softening law, controlling the possible changes in size (increase or decrease), shape and position of the yield surface after its elastic peak strength has been reached; (3) flow rule, controlling the progression of the plasticity in rock material.

Generally, plastic flow rule related to strain rates ($\dot{\varepsilon}$) or strain increments ($d\varepsilon_{ij}$), and stresses (σ_{ij}) or deviatoric stresses (s_{ij}).

In elastoplastic nonlinear range, the total strain, ε, or total strain increment, $d\varepsilon$, consists of the elastic part, ε^e or $d\varepsilon^e$, and plastic part ε^p or $d\varepsilon^p$. Thus,

$$\varepsilon = \varepsilon^e + \varepsilon^p \tag{2.16}$$

or

$$d\varepsilon = d\varepsilon^e + d\varepsilon^p \tag{2.17}$$

and the correspondent stress increment, $d\sigma$, is directly expressed on the basis of the elastic constitutive law.

$$\mathrm{d}\sigma = [\mathrm{D}]\mathrm{d}\varepsilon^e = [\mathrm{D}](\mathrm{d}\varepsilon - \mathrm{d}\varepsilon^p) \tag{2.18}$$

If the rock material follows associated flow rule,

$$d\varepsilon^p = F(F, \lambda) \tag{2.19}$$

If the rock material follows nonassociated flow rule,

$$d\varepsilon^p = Q(Q, \lambda) \tag{2.20}$$

where λ is the hardening parameter; F and Q are the yield function and plastic potential function respectively, which are the functions of stress invariants and hardening/softening parameter and are model-dependent (will be discussed in details in next section).

The generalized yield function, F, can be expressed as follows:

$$F = F[\sigma, h(\varepsilon^p)] \tag{2.21}$$

where $h(\varepsilon^p)$ is the hardening function, governing the changes of yield surfaces with the increase or decrease of the plastic strains.

As shown in Figure 2.4, if F = 0, the stress state of the material satisfies the yield condition, that is, on the yield surface. If F < 0, the stress state of the material is in the elastic stress state. If F > 0, in Drucker's sense (Drucker & Prager, 1952), the stress state of the material is in an unstable stress state.

Similarly, the generalized plastic potential function, Q, can be expressed as:

$$Q=Q[\sigma, h(\varepsilon^p)] \tag{2.22}$$

It should be noted that $d\varepsilon^p$ is always perpendicular to the plastic potential surface, Q. If F =Q, $d\varepsilon^p$ will be perpendicular to the yield surface, and the associated flow rule will be conformed to.

If $h(\varepsilon^p) = 0$, it is called perfect plasticity. In this stress state, the yield function and plastic potential functions are only related to stress invariants.

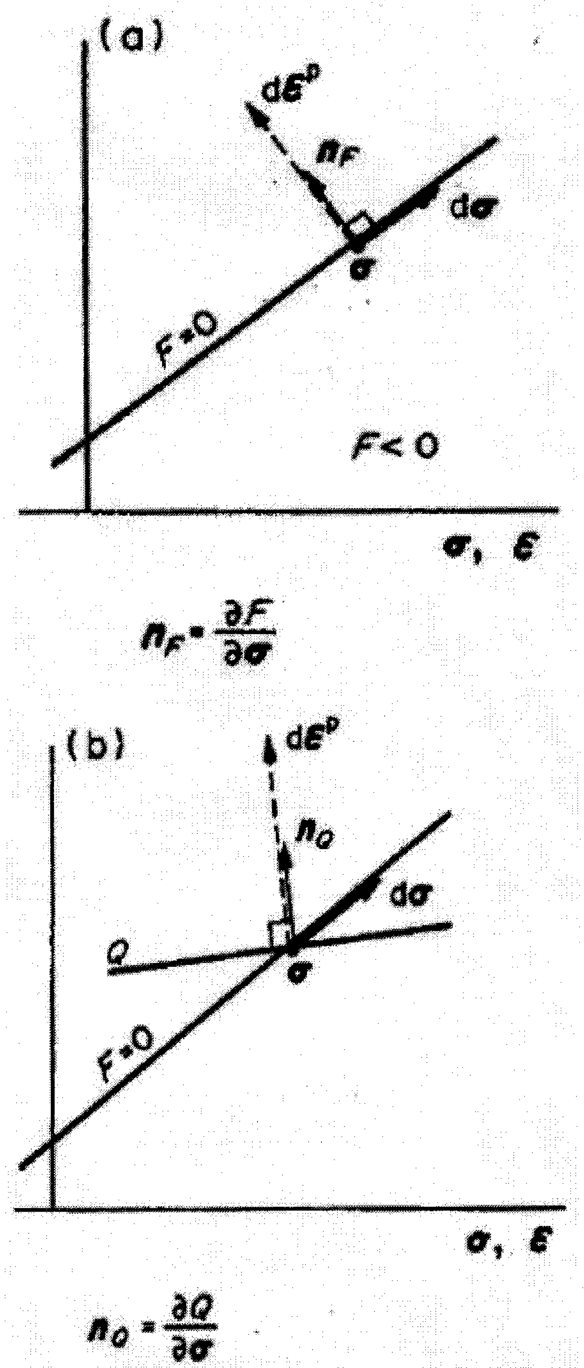

Figure 2. 4 Elastoplastic material behaviour with flow rules
(a) Associated flow rule, (b) Nonassociated flow rule.
F, yield function; Q, plastic potential function (Cividini, 1992)

2.3 Mohr-Coulomb model

As discussed previously, rock material elastoplasticity models are versatile. In this section, the focus is Coulomb materials (Coulomb, 1776) and how to implement Mohr-Coulomb model in rock mechanics. Due to the corners of M-C yield surfaces and plastic potential surfaces in 2D and 3D problems, the mathematical discontinuities of the first derivatives at the corners pose difficulties in computer programming. To deal with this problem, a rounded corner approach by using Drucker-Prager models will be adopted (Drucker & Prager, 1952). Furthermore, it will be centered on elastic perfectly-plastic model with nonassociated flow rule to model rock material hardening/softening behaviours (Vermeer, 1998). Figure 2.5 shows the elastic perfectly-plastic stress-strain relationship.

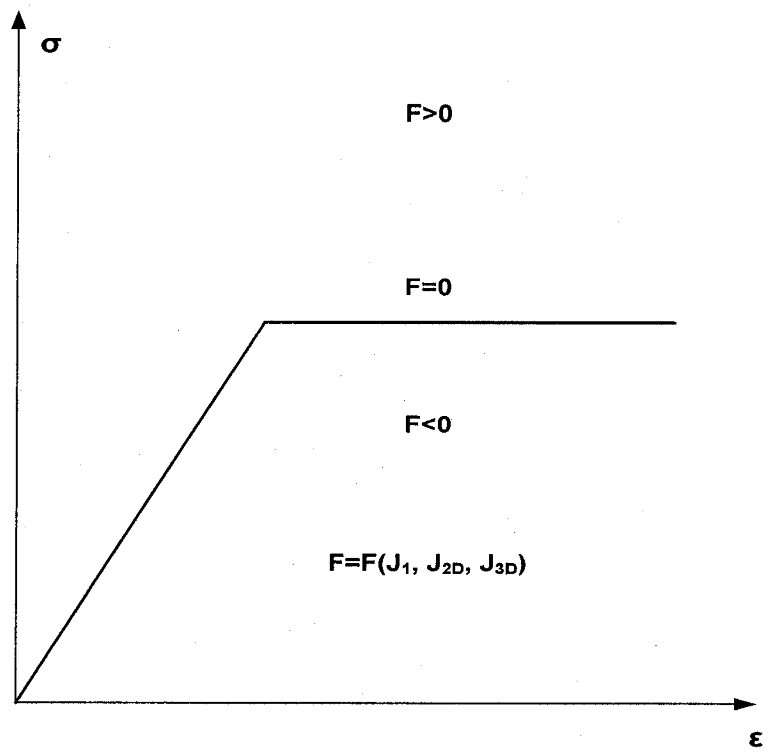

Figure 2. 5 Elastic perfectly-plastic stress-strain relationship

2.3.1 Stress invariants

Defining the mean stress or hydrostatic stress σ_m as:

$$\sigma_m = \frac{1}{3}(\sigma_x + \sigma_y + \sigma_z) = \frac{1}{\sqrt{3}} s \tag{2.23}$$

where

$$s = \frac{1}{\sqrt{3}}(\sigma_x + \sigma_y + \sigma_z) \tag{2.24}$$

Defining deviatoric stress $\bar{\sigma}$ in triaxial test as:

$$\bar{\sigma} = \sqrt{\frac{3}{2}} t \tag{2.25}$$

$$\bar{\sigma} = \sqrt{3}\sqrt{J_{2D}} \tag{2.26}$$

where J_{2D} is the second invariant of deviatoric stress tensor.

$$\mathrm{J}_{2\mathrm{D}} = \frac{1}{6}[(\sigma_x - \sigma_y)^2 + (\sigma_y - \sigma_z)^2 + (\sigma_z - \sigma_x)^2] + \tau_{xy}{}^2 + \tau_{yz}{}^2 + \tau_{zx}{}^2 \tag{2.27}$$

or

$$\mathrm{J}_{2\mathrm{D}} = \frac{1}{6}[(\sigma_1 - \sigma_2)^2 + (\sigma_2 - \sigma_3)^2 + (\sigma_3 - \sigma_1)^2] \tag{2.28}$$

and

$$t = \frac{1}{\sqrt{3}}\left[(\sigma_x - \sigma_y)^2 + (\sigma_y - \sigma_z)^2 + (\sigma_z - \sigma_x)^2 + 6\tau_{xy}^2 + 6\tau_{yz}^2 + 6\tau_{zx}^2\right]^{\frac{1}{2}} \tag{2.29}$$

Defining the Lode angle θ as:

$$\theta = \frac{1}{3}\arcsin\left(\frac{-3\sqrt{6}J_{3D}}{t^3}\right) = \frac{1}{3}\arcsin\left(\frac{-3\sqrt{3}J_{3D}}{2J_{2D}{}^{3/2}}\right) \tag{2.30}$$

$$-\pi/6 \leqslant \theta \leqslant \pi/6$$

where J_{3D} is the third invariant of deviatoric stress tensor.

$$J_{3D} = s_x s_y s_z - s_x\tau_{yz}^2 - s_y\tau_{zx}^2 - s_z\tau_{xy}^2 + 2\tau_{xy}\tau_{yz}\tau_{zx} \tag{2.31}$$

and deviatoric stress

$$s_x = (\sigma_x - \sigma_m) = \frac{2\sigma_x - \sigma_y - \sigma_z}{3} \qquad etc. \tag{2.32}$$

The physical meanings of s and t can be explained with Figure 2.6 and 2.7. For stress point P in stress space, s is the stress component along the hydrostatic line and t is the stress component to the hydrostatic line (in π plane is the radius of stress envelope). In π plane, θ is the angle from bisection to the stress component t. If stress point P is between the bisection and the principal stress axis, θ is positive, otherwise, negative (Figure 2.7).

In 2D problem, due to $\tau_{yz} = \tau_{zx} = 0$, equation (2.29) and (2.31) can be simplified, which will be extensively used in 2D problem programming, as:

$$t = \frac{1}{\sqrt{3}}\left[(\sigma_x - \sigma_y)^2 + (\sigma_y - \sigma_z)^2 + (\sigma_z - \sigma_x)^2 + 6\tau_{xy}^2\right]^{\frac{1}{2}} \tag{2.33}$$

$$J_{3D} = s_x s_y s_z - s_z \tau_{xy}^2 \tag{2.34}$$

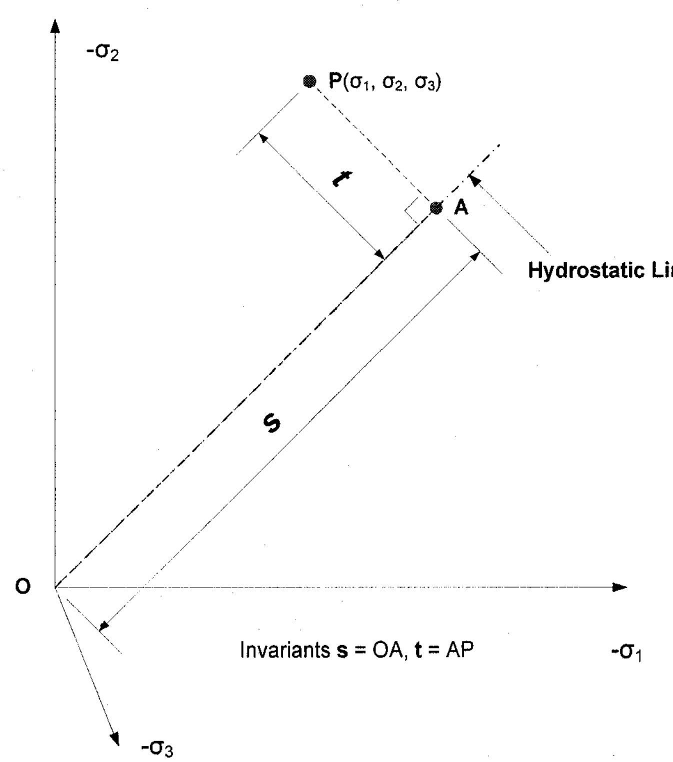

Figure 2. 6 Stress components of s and t in stress space

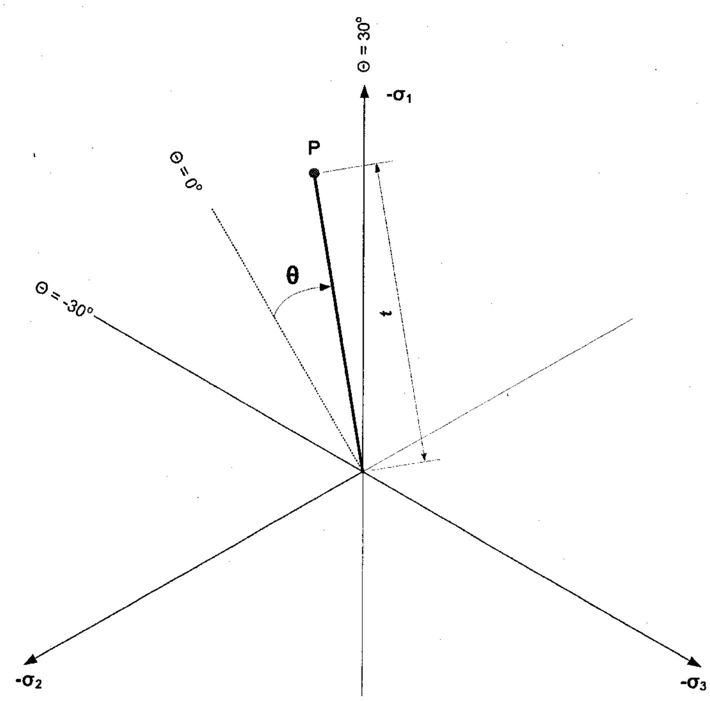

Figure 2. 7 Lode angle and stress component t in π plane

By using stress invariants, the relationship between principal stresses and stress invariants can be easily expressed as follows:

$$\begin{aligned} \sigma_1 &= \sigma_m + \frac{2}{3}\bar{\sigma}\sin(\theta - \frac{2\pi}{3}) \\ \sigma_2 &= \sigma_m + \frac{2}{3}\bar{\sigma}\sin\theta \\ \sigma_3 &= \sigma_m + \frac{2}{3}\bar{\sigma}\sin(\theta + \frac{2\pi}{3}) \end{aligned} \tag{2.35}$$

Equation (2.35) ensures that σ_1 is the most compressive stress and σ_3 is the least compressive stress. Lode angle, θ, ranges $-\pi/6 \leq \theta \leq \pi/6$

2.3.2 Mohr-Coulomb yield function and plastic potential function

Mohr-Coulomb yield criterion can be expressed as:

$$F = \sigma_m \sin\phi + \bar{\sigma}(\frac{\cos\theta}{\sqrt{3}} - \frac{\sin\theta \sin\phi}{3}) - c\cos\phi \tag{2.36}$$

where ϕ and c are material friction angle and cohesion, respectively.

The yield function, F, can be interpreted as follows (see Figure 2.5).

If $F < 0$, stress state is inside the yield surface—elastic;

If $F = 0$, stress state is on the yield surface—yielding;

If $F > 0$, stress state is outside the yield surface—yielding (and/or with hardening) and the stresses must be redistributed and back to the yield surface.

Mohr-Coulomb material plastic potential function is similar to yield function, but ϕ is replace by dilation angle, ψ.

$$Q = \sigma_m \sin\psi + \bar{\sigma}(\frac{\cos\theta}{\sqrt{3}} - \frac{\sin\theta \sin\psi}{3}) - c\cos\psi \tag{2.37}$$

If $\psi < 0$, the material volume will decrease during yielding—contraction state;

If $\psi > 0$, the material volume will increase during yielding—dilation state;

If $\psi = 0$, the material volume will not change during yielding—constant volume state;

If $\psi = \phi$, the material will have maximum volume change—associated flow rule. So associated flow rule is a special case of nonassociated flow rule.

In principal stress space, Mohr-Coulomb yield surface is shown in Figure 2.8.

2.3.3 Dilation angle

Dilation angle is defined as (Vermeer, 1998):

$$\psi = \sin^{-1}\frac{\dot{\varepsilon}_v^p}{-2\dot{\varepsilon}_1^p + \dot{\varepsilon}_v^p} \tag{2.38}$$

For plain strain problem:

$$\psi = \sin^{-1}\frac{\dot{\varepsilon}_v^p}{\dot{\gamma}^p} \tag{2.39}$$

where $\dot{\varepsilon}_v^p$ and $\dot{\gamma}^p$ are the plastic volumetric strain rate and plastic distortion rate respectively, and

$$\begin{aligned}\dot{\varepsilon}_v^p &= \dot{\varepsilon}_x^p + \dot{\varepsilon}_y^p + \dot{\varepsilon}_z^p \\ &= \dot{\varepsilon}_x^p + \dot{\varepsilon}_y^p \quad (for \quad plane \quad strain)\end{aligned} \tag{2.40}$$

$$\dot{\gamma}^p = \sqrt{(\dot{\varepsilon}_x^p - \dot{\varepsilon}_y^p)^2 + (\dot{\gamma}_{xy}^p)^2} \tag{2.41}$$

where $\dot{\varepsilon}_i^p$ is the plastic strain rate in i's direction.

For rock materials, $\psi = 12 - 20^o$ (Vermeer, 1998).

Hoek and Brown (1997) suggest that if rock mass quality is very good (GSI $\geq$ 75), $\psi \approx 1/4\Phi$; if rock mass quality is average (GSI $\approx$ 50), $\psi \approx 1/8\Phi$ and if rock mass quality is very poor (GSI $\leq$ 30), $\psi = 0$.

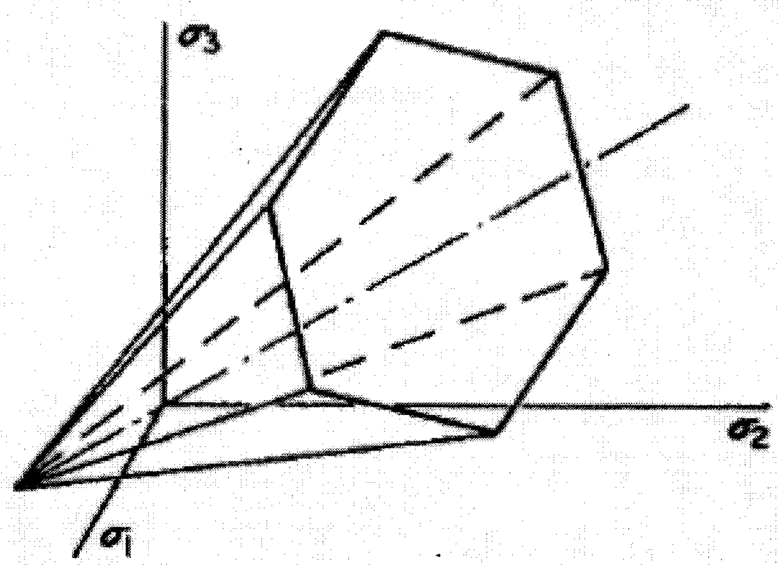

Figure 2. 8 Mohr-Coulomb yield surface in the principal stress space (Pariseau, 1992b)

2.3.4 Corner solver of Mohr-Coulomb model—Drucker-Prager models

Because the derivatives of the yield function and plastic potential function are normal to their surfaces, such derivatives can not be determined at the vertices of the hexagonal surfaces in the π-plane. These vertices correspond to triaxial stress states. To solve the corner problems, Zienkiewicz and Humphson proposed the rounded corner approach (Zienkiewicz & Humpheson, 1977). This means that if the angular invariant θ is approaching ±30° with some tolerance, smoothed cone surfaces, e.g. Drucker-Prager yield surfaces, are to be used to approximate the Mohr-Coulomb yield surface and plastic potential surface. One choice is that when θ = 30°, the stress states are approximated by D-P outer cone (F_{OC}); when θ = -30°, the stress states are approximated by D-P inner cone (F_{IC}).

In the present work, Drucker-Prager yield function and plastic potential function are used as the rounded cone versions when

$$|\sin\theta| > 0.49, \qquad or \quad |\theta| > 29.34^0$$

$$F_{D-P} = \alpha J_1 + \sqrt{J_{2D}} - k \tag{2.42}$$

$$Q_{D-P} = \alpha_Q J_1 + \sqrt{J_{2D}} - k_Q \tag{2.43}$$

where α ,k, α_Q and k_Q are material constants; J_1 *and* J_{2D} are the first invariant of stress tensor and the second invariant of deviatoric stress tensor, respectively.

Drucker-Prager yield surface and plastic potential surface in principal stress space are cone shape, as shown in Figure 2.9.

For an outer cone:

$$\begin{aligned} \alpha &= \frac{2\sin\phi}{\sqrt{3}(3-\sin\phi)} \\ k &= \frac{6c\cos\phi}{\sqrt{3}(3-\sin\phi)} \end{aligned} \tag{2.44}$$

$$\alpha_Q = \frac{2\sin\psi}{\sqrt{3}(3-\sin\psi)}$$
$$k_Q = \frac{6c\cos\psi}{\sqrt{3}(3-\sin\psi)} \tag{2.45}$$

For an inner cone:

$$\alpha = \frac{2\sin\phi}{\sqrt{3}(3+\sin\phi)}$$
$$k = \frac{6c\cos\phi}{\sqrt{3}(3+\sin\phi)} \tag{2.46}$$

$$\alpha_Q = \frac{2\sin\psi}{\sqrt{3}(3+\sin\psi)}$$
$$k_Q = \frac{6c\cos\psi}{\sqrt{3}(3+\sin\psi)} \tag{2.47}$$

Note that $\sigma_m = \frac{1}{3}J_1$ and $\sqrt{J_{2D}} = \frac{\bar{\sigma}}{\sqrt{3}}$, substituting these material constants and let $\theta = \pm 30^0$, Drucker-Prager yield function and plastic potential function can be derived as Mohr-Coulomb form:

$$F = \sigma_m \sin\phi + \frac{\bar{\sigma}}{2}(1 \pm \frac{\sin\phi}{3}) - c\cos\phi \tag{2.48}$$

$$Q = \sigma_m \sin\psi + \frac{\bar{\sigma}}{2}(1 \pm \frac{\sin\psi}{3}) - c\cos\psi \tag{2.49}$$

where the positive sign is taken if $\theta \Rightarrow -30^0$ and negative sign is adopted if $\theta \Rightarrow 30^0$.

Figure 2.10 shows the relationship between Mohr-Coulomb yield surface and Drucker-Prager yield surfaces.

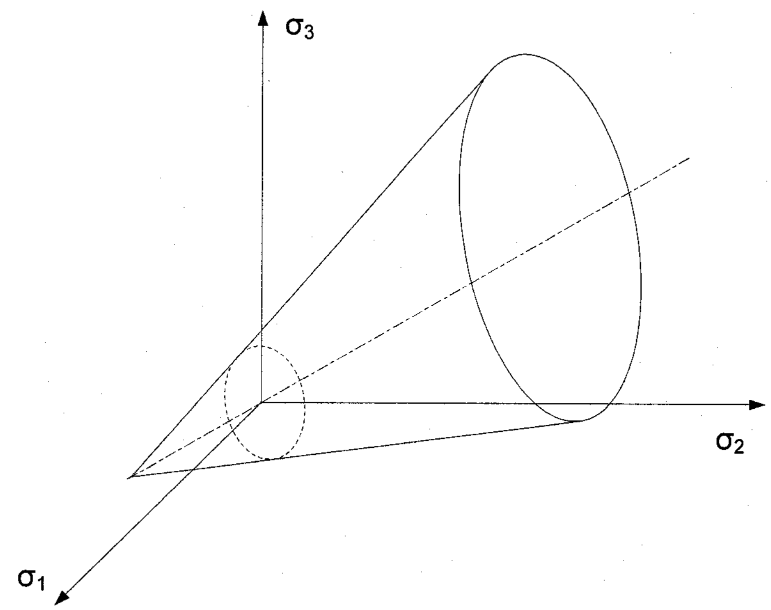

Figure 2. 9 Drucker-Prager yield surface in the principal stress space

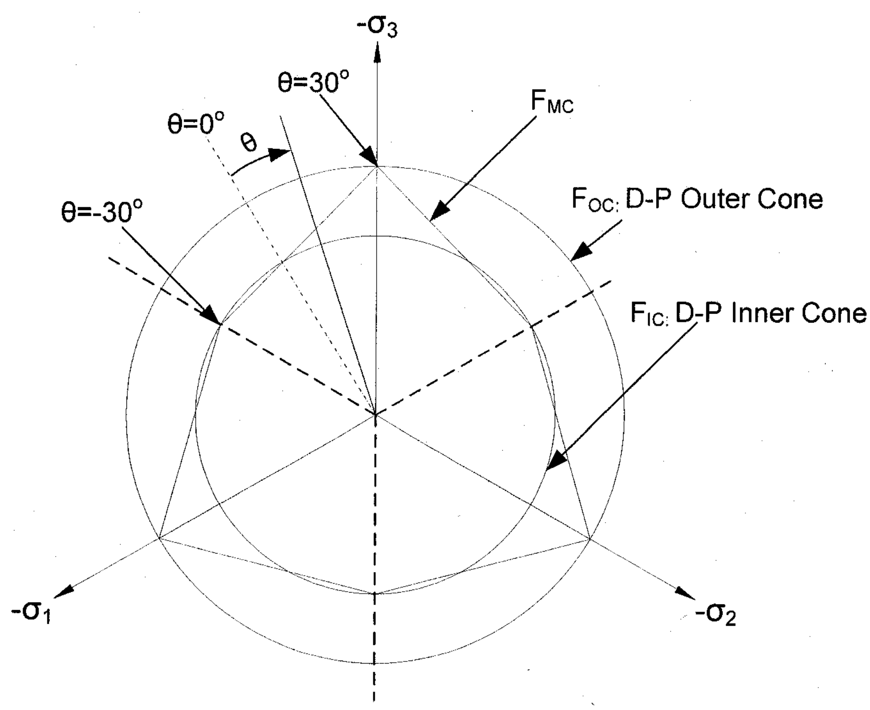

Figure 2. 10 Mohr-Coulomb yield surface with rounded corners by Drucker-Prager cones

2.4 Empirical model—Hoek-Brown failure criterion

2.4.1 Hoek-Brown failure criterion

Hoek-Brown empirical failure criterion has been developed and improved several versions. The criterion linked the equation to geological observations, originally in the form of Bieniawski's Rock Mass Rating (RMR) (Bieniawski, 1973) and recently to the Geological Strength Index (GSI). Its usage has been expanded from confined hard rock to a wide range of confined soils, weak rocks, and hard rocks

The original Hoek-Brown empirical failure criterion (Hoek & Brown, 1980a, 1980b) is written as:

$$\sigma_1 = \sigma_3 + (m\sigma_3\sigma_c + s\sigma_c^2)^{1/2} \tag{2.50}$$

where m and s are the rock mass constants, which are related to the angle of internal friction of rock mass and the rock mass cohesion, respectively; σ_c is the uniaxial compressive strength of intact rock material.

For disturbed rock masses (Hoek & Brown, 1988):

$$m_b = m_i \exp(\frac{RMR-100}{14}) \tag{2.51}$$

$$s = \exp(\frac{RMR-100}{6}) \tag{2.52}$$

For undisturbed or interlocking rock masses (Hoek & Brown, 1988)

$$m_b = m_i \exp(\frac{RMR-100}{28}) \tag{2.53}$$

$$s = \exp(\frac{RMR-100}{9}) \tag{2.54}$$

$$E = 10\exp(\frac{RMR-10}{40}) \tag{2.55}$$

where m_b and m_i are for broken rock and intact rock, respectively.

For intact rock, m = 0, s = 1 (Hoek, Wood, & Shah, 1992).

For brittle rock, m = 0, s = 0.11 (Martin, Kaiser, & Creath, 1999).

The generalized Hoek-Brown failure criterion (Hoek, 1994; Hoek & Brown, 1997; Hoek, Carranza-Torres, & Corkum, 2002) is expressed as:

$$\sigma_1 = \sigma_3 + \sigma_c \{m_b \frac{\sigma_3}{\sigma_c} + s\}^a \tag{2.56}$$

where m_b, s and a are rock material constants that can be related to Geological Strength Index (GSI) (Hoek, Marinos, & Benissi, 1998) and the degree of rock damage.

$$m_b = m_i \exp(\frac{GSI-100}{28-14D}) \tag{2.57}$$

$$s = \exp(\frac{GSI-100}{9-3D}) \tag{2.58}$$

$$a = \frac{1}{2} + \frac{1}{6}(e^{-GSI/15} - e^{-20/3}) \tag{2.59}$$

where m_i is the intact rock material constant, and D is a factor which depends on the degree of disturbance to which the rock mass has been subjected by blast damage and stress relaxation. D varies from 0 for undisturbed in situ rock masses to 1 for very disturbed rock masses.

The uniaxial compressive strength of rock mass, σ_{bc}, can be obtained by setting $\sigma_3 = 0$:

$$\sigma_{bc} = \sigma_c s^a \tag{2.60}$$

and the tensile strength can be obtained by setting $\sigma_1 = \sigma_3 = \sigma_t$:

$$\sigma_t = -\frac{s\sigma_c}{m_b} \tag{2.61}$$

Hoek (1983) showed that for brittle materials the uniaxial tensile strength is equal to the biaxial tensile strength.

2.4.2 A proposed flow rule for Hoek-Brown model

Cundall (2005) proposed that many rock materials under unconfined compression exhibit large rate of volumetric expansion at yielding, and the associated flow rule may be used because it provides the largest volumetric strain rate.

$$d\varepsilon_i = \lambda \frac{\partial F}{\partial \sigma_i} \tag{2.62}$$

where

$$\lambda = \frac{1}{1 + a\sigma_c ({}^{m_b \sigma_3}\!/_{\sigma_c} + s)^{a-1} ({}^{m_b}\!/_{\sigma_c})} \tag{2.63}$$

2.4.3 Pros and cons of Hoek-Brown model

Hoek-Brown failure criterion has following advantages:

- Simple and easy to use,
- Reasonably estimates rock mass strength under high confinement.

Hoek-Brown model is the relationship between the major and minor principal stresses. It ignores the intermediate principal stress. For elastoplastic analysis, it has following disadvantages:

- Invalid for checking failure at the boundary of underground openings,
- Missing solid flow rule and hardening/softening rule,
- Unsuitable for simulating nonlinear behaviour of rock materials (Lorig & Varona, 2004).

Chapter 3 Finite Element Analysis

The Finite Element Method (FEM) (Clough, 1960; Turner, Clough, Martin, & Topp, 1956) is one of the most popular and powerful numerical methods of analysis. It is used to formulate mathematical algorithms for the solution of engineering problems. FEM is a computer-aided mathematical tool used to obtain approximate solutions for engineering problems that can be represented by the physical system subject to external influences.

The essence of the Finite Element Method is to divide the problem domain into a number of elements of various shapes, e.g. triangles, quadrilaterals, tetrahedrons, and bricks. For each element, based on the element stiffness properties and the applied loads, we can form the static equilibrium equations, called element equations. By assembling element equations, the global equations are formed. By solving global equations at the nodes, we can obtain the solutions for linear problems. By solving sets of piecewise linear functions using incremental methods, the solutions for nonlinear problems is obtained.

Various element shapes can adapt to almost any model domain geometry. FEM can model not only complex geometry, but also other important characteristics of materials, such as nonlinear and/or heterogeneous material behaviour, and time dependent phenomena. This ability makes FEM very powerful and versatile.

Engineering applications of finite element method in rock mechanics can be utilized in three major fields: civil engineering, petroleum engineering and mining engineering (Mitri, 2005). For example, in open pit mining, FEM is widely used in slope stability analysis; in underground mining, FEM is used for calculation of stresses around pillars (Blake, 1971), hanging walls & footwall walls (Pariseau, 1980), tunnels (Feder, 1979), support of underground openings (Ranken & Ghaboussi, 1975), etc. It should be noted that the early applications of FEM to underground mining were restricted to material elasticity or elastoviscosity.

Even though the results are rarely exact due to the limitations of computer hardware and the difficulties of estimating rock mass properties, they are nevertheless useful for guiding engineering design practices. Prediction can be improved by considering more realistic material properties and by processing finer mesh with more equations thanks to modern computer technology.

3.1 Finite element equations

3.1.1 Mapping: physical element, isoparametric element and parent element

In finite element analysis, isoparametric element is an element for which element shape and field quantities (e.g. stresses, strains, displacements, etc.) are defined by the same interpolation functions, or shape functions. The physical elements of various sizes and shapes are all mapped into the so called parent elements, which have the same size and shape in local coordinates (Rao, 1989).

Figure 3.1 shows a typical parent quadrilateral element mapping to the physical elements with straight edges and/or curved edges. As an example, this figure also illustrates the mapping results of the coordinates of the four nodes between local system and global system.

For a two dimensional element, the general form of transformation relationship is as follows.

For coordinates:

$$x = \sum_{i=1}^{n} N_i X_i \qquad y = \sum_{i=1}^{n} N_i Y_i \tag{3.1}$$

For displacements:

$$u = \sum_{i=1}^{n} N_i u_i \qquad v = \sum_{i=1}^{n} N_i v_i \tag{3.2}$$

where

x, y are global coordinates;

X_i, Y_i are global coordinates at node *i*;

u, v are displacements in x, y directions, respectively;

u_i, v_i are displacements at node *i* in x, y directions, respectively;

N_i is element shape function with respect to local coordinates, and will be discussed in detail in the next section;

n is the number of nodes for each element.

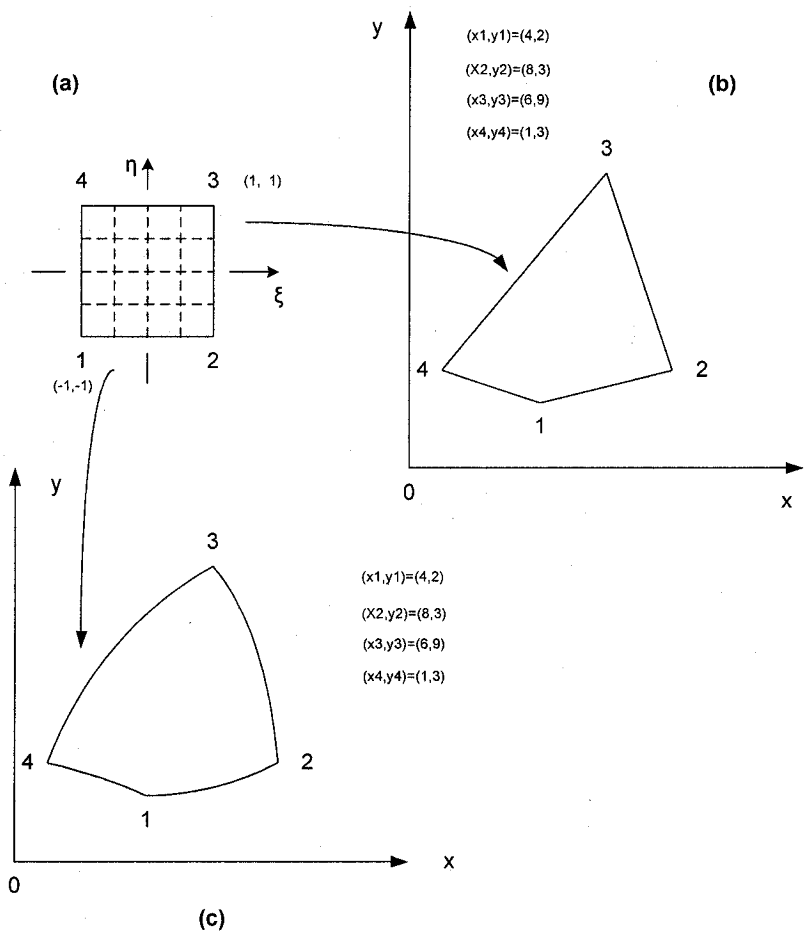

Figure 3. 1 Mapping of quadrilateral isoparametric element
(a) parent element in local coordinates (local system); (b) straight edge physical quadrilateral element in Cartesian coordinates(global system); (c) curved edge physical quadrilateral element in Cartesian coordinates(global system)

3.1.2 Shape functions and their derivatives

As discussed previously, for an isoparametric element, element shape and field quantities all share the same shape functions. This is the biggest characteristic and advantage of isoparametric elements; it simplifies the calculations of all field quantities.

3.1.2.1 One dimensional element shape functions

For a two-node element:

$$\begin{aligned} N_1 &= \frac{1}{2}(1-\xi) \\ N_2 &= \frac{1}{2}(1+\xi) \end{aligned} \tag{3.3}$$

For a three-node element:

$$\begin{aligned} N_1 &= -\frac{1}{2}\xi(1-\xi) \\ N_2 &= \frac{1}{2}\xi(1+\xi) \\ N_3 &= (1+\xi)(1-\xi) \end{aligned} \tag{3.4}$$

3.1.2.2 Two dimensional element shape functions

From one dimensional element shape functions, we can derive two dimensional element shape functions.

For a three-node triangle element:

$$\begin{aligned} N_1 &= \xi \\ N_2 &= \eta \\ N_3 &= 1-\xi-\eta \end{aligned} \tag{3.5}$$

For a six-node triangle element:

$$\begin{aligned} N_1 &= (2\xi-1)\xi \\ N_2 &= (2\eta-1)\eta \\ N_3 &= [2(1-\xi-\eta)-1](1-\xi-\eta) \\ N_4 &= 4\xi\eta \\ N_5 &= 4(1-\xi-\eta)\eta \\ N_6 &= 4(1-\xi-\eta)\xi \end{aligned} \tag{3.6}$$

For a four-node quadrilateral element:

$$
\begin{aligned}
N_1 &= \frac{1}{4}(1-\xi)(1-\eta) \\
N_2 &= \frac{1}{4}(1+\xi)(1-\eta) \\
N_3 &= \frac{1}{4}(1+\xi)(1+\eta) \\
N_4 &= \frac{1}{4}(1-\xi)(1+\eta)
\end{aligned}
\tag{3.7}
$$

For an eight-node quadrilateral element:

$$
\begin{aligned}
N_1 &= \frac{1}{4}(1-\xi)(1-\eta)(-\xi-\eta-1) \\
N_2 &= \frac{1}{4}(1+\xi)(1-\eta)(\xi-\eta-1) \\
N_3 &= \frac{1}{4}(1+\xi)(1+\eta)(\xi+\eta-1) \\
N_4 &= \frac{1}{4}(1-\xi)(1+\eta)(-\xi+\eta-1) \\
N_5 &= \frac{1}{2}(1-\xi)(1-\eta)(1+\xi) \\
N_6 &= \frac{1}{2}(1+\xi)(1+\eta)(1-\eta) \\
N_7 &= \frac{1}{2}(1+\xi)(1+\eta)(1-\xi) \\
N_8 &= \frac{1}{2}(1-\xi)(1-\eta)(1+\eta)
\end{aligned}
\tag{3.8}
$$

The node number sequences are defined as Figure3.1, 3.2 and 3.3.

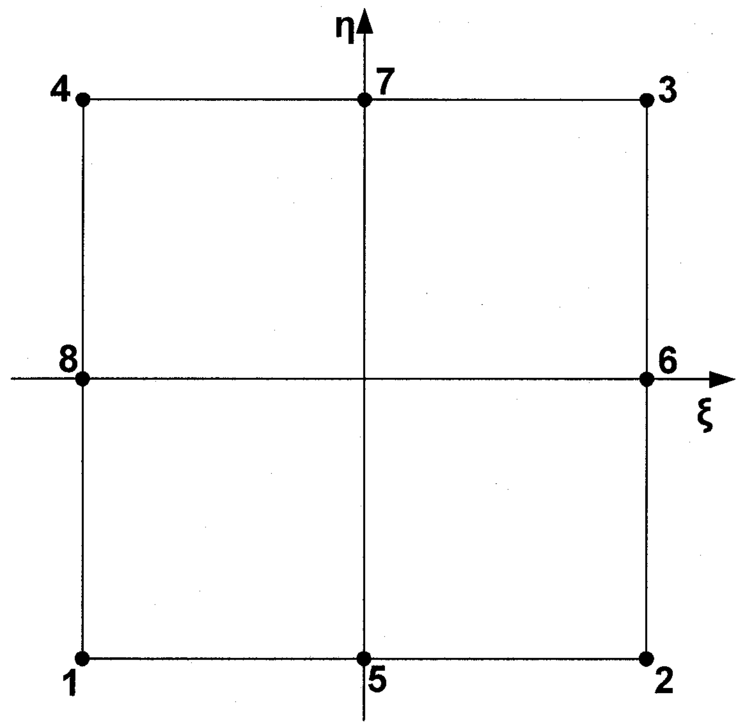

Figure 3. 2 Numbering sequence of four and eight-node quadrilateral element

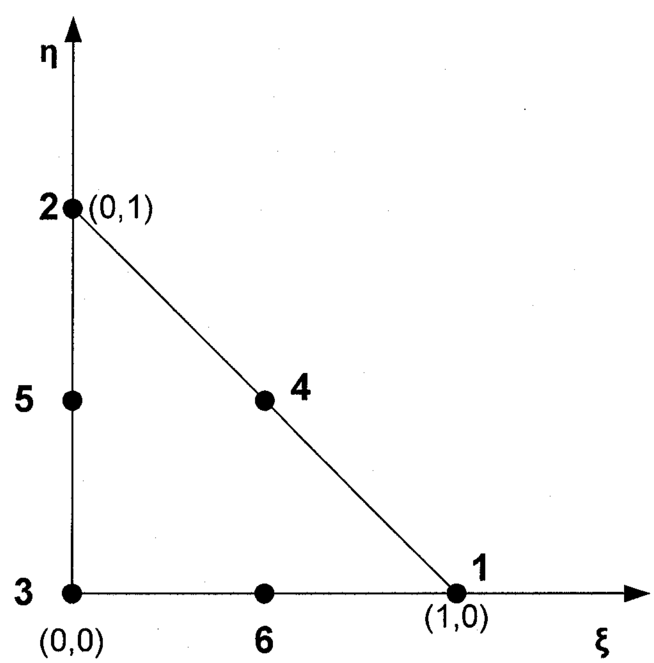

Figure 3. 3 Numbering sequence of three and six-node triangle element

3.1.2.3 Derivatives of shape functions

The derivatives of shape functions with respect to local system are as follows:

For a three-node triangle element:

$$\begin{bmatrix} \dfrac{\partial N_i}{\partial \xi} \\ \dfrac{\partial N_i}{\partial \eta} \end{bmatrix} = \begin{bmatrix} 1 & 0 & -1 \\ 0 & 1 & -1 \end{bmatrix} \tag{3.9}$$

For a six-node triangle element:

$$\begin{bmatrix} \dfrac{\partial N_i}{\partial \xi} \\ \dfrac{\partial N_i}{\partial \eta} \end{bmatrix} = \begin{bmatrix} 4\xi-1 & 0 & 2(\xi+\eta-1) & 4\eta & -4\eta & 4(1-\eta-2\xi) \\ 0 & 4\eta-1 & 2(\xi+\eta-1) & 4\xi & 4(1-\xi-2\eta) & -4\xi \end{bmatrix} \tag{3.10}$$

For a four-node quadrilateral element:

$$\begin{bmatrix} \dfrac{\partial N_i}{\partial \xi} \\ \dfrac{\partial N_i}{\partial \eta} \end{bmatrix} = \frac{1}{4}\begin{bmatrix} -(1-\eta) & (1-\eta) & (1+\eta) & -(1+\eta) \\ -(1-\xi) & -(1+\xi) & (1+\xi) & (1-\xi) \end{bmatrix} \tag{3.11}$$

For an eight-node quadrilateral element:

$$
\begin{aligned}
&\frac{\partial N_1}{\partial \xi}=\frac{1}{4}(1-\eta)(2\xi+\eta) && \frac{\partial N_1}{\partial \eta}=\frac{1}{4}(1-\xi)(2\eta+\xi)\\
&\frac{\partial N_2}{\partial \xi}=\frac{1}{4}(1-\eta)(2\xi-\eta) && \frac{\partial N_2}{\partial \eta}=\frac{1}{4}(1+\xi)(2\eta-\xi)\\
&\frac{\partial N_3}{\partial \xi}=\frac{1}{4}(1+\eta)(2\xi+\eta) && \frac{\partial N_3}{\partial \eta}=\frac{1}{4}(1+\xi)(2\eta+\xi)\\
&\frac{\partial N_4}{\partial \xi}=\frac{1}{4}(1+\eta)(2\xi-\eta) && \frac{\partial N_4}{\partial \eta}=\frac{1}{4}(1-\xi)(2\eta-\xi)\\
&\frac{\partial N_5}{\partial \xi}=-\xi(1-\eta) && \frac{\partial N_5}{\partial \eta}=-\frac{1}{2}(1-\xi^2)\\
&\frac{\partial N_6}{\partial \xi}=\frac{1}{2}(1-\eta^2) && \frac{\partial N_6}{\partial \eta}=-\eta(1+\xi)\\
&\frac{\partial N_7}{\partial \xi}=-\xi(1+\eta) && \frac{\partial N_7}{\partial \eta}=\frac{1}{2}(1-\xi^2)\\
&\frac{\partial N_8}{\partial \xi}=-\frac{1}{2}(1-\eta^2) && \frac{\partial N_8}{\partial \eta}=-\eta(1-\xi)
\end{aligned}
\tag{3.12}
$$

3.1.3 Strain-displacement relationship

From the small deformation theory, for a two dimensional problem, the strain-displacement relationship can be expressed as:

$$
\begin{aligned}
\varepsilon_x &= \frac{\partial u}{\partial x}\\
\varepsilon_y &= \frac{\partial v}{\partial y}\\
\gamma_{xy} &= \frac{\partial u}{\partial y}+\frac{\partial v}{\partial x}
\end{aligned}
\tag{3.13}
$$

or

$$
\begin{bmatrix}\varepsilon_x\\ \varepsilon_y\\ \gamma_{xy}\end{bmatrix}=\begin{bmatrix}\frac{\partial}{\partial x} & 0\\ 0 & \frac{\partial}{\partial y}\\ \frac{\partial}{\partial y} & \frac{\partial}{\partial x}\end{bmatrix}\begin{Bmatrix}u\\ v\end{Bmatrix}
\tag{3.14}
$$

Substitutes equation (3.2) into equation (3.14) and apply the chain rule, it can be get

$$
\{\varepsilon\}=[B]\{d\}
\tag{3.15}
$$

where

$$\{\varepsilon\} = \left[\varepsilon_x, \varepsilon_y, \gamma_{xy}\right]^T \text{ is the strain vector} \tag{3.16}$$

$$\{d\} = \begin{bmatrix} u_1 & v_1 & \dots & \dots & u_n & v_n \end{bmatrix}^T \text{ is the generalized displacement vector} \tag{3.17}$$

[B] is the strain-displacement matrix, depending on the element type and the number of nodes.

For a three-node triangle element:

$$[B] = \frac{1}{2A}\begin{bmatrix} (y_2 - y_3) & 0 & (y_3 - y_1) & 0 & (y_1 - y_2) & 0 \\ 0 & -(x_2 - x_3) & 0 & -(x_3 - x_1) & 0 & -(x_1 - x_2) \\ -(x_2 - x_3) & (y_2 - y_3) & -(x_3 - x_1) & (y_3 - y_1) & -(x_1 - x_2) & (y_1 - y_2) \end{bmatrix} \tag{3.18}$$

where A is the area of the triangle. Apparently, [B] is a constant, so the element is called constant strain triangle, or CST.

For a four-node quadrilateral element:

$$[B] = \begin{bmatrix} \frac{\partial N_1}{\partial x} & 0 & \frac{\partial N_2}{\partial x} & 0 & \frac{\partial N_3}{\partial x} & 0 & \frac{\partial N_4}{\partial x} & 0 \\ 0 & \frac{\partial N_1}{\partial y} & 0 & \frac{\partial N_2}{\partial y} & 0 & \frac{\partial N_3}{\partial y} & 0 & \frac{\partial N_4}{\partial y} \\ \frac{\partial N_1}{\partial y} & \frac{\partial N_1}{\partial x} & \frac{\partial N_2}{\partial y} & \frac{\partial N_2}{\partial x} & \frac{\partial N_3}{\partial y} & \frac{\partial N_3}{\partial x} & \frac{\partial N_4}{\partial y} & \frac{\partial N_4}{\partial x} \end{bmatrix} \tag{3.19}$$

For an eight-node quadrilateral element:

$$[B] = \begin{bmatrix} \frac{\partial N_1}{\partial x} & 0 & \frac{\partial N_2}{\partial x} & 0 & \frac{\partial N_3}{\partial x} & 0 & \frac{\partial N_4}{\partial x} & 0 & & \frac{\partial N_8}{\partial x} & 0 \\ 0 & \frac{\partial N_1}{\partial y} & 0 & \frac{\partial N_2}{\partial y} & 0 & \frac{\partial N_3}{\partial y} & 0 & \frac{\partial N_4}{\partial y} & \dots\dots & 0 & \frac{\partial N_8}{\partial y} \\ \frac{\partial N_1}{\partial y} & \frac{\partial N_1}{\partial x} & \frac{\partial N_2}{\partial y} & \frac{\partial N_2}{\partial x} & \frac{\partial N_3}{\partial y} & \frac{\partial N_3}{\partial x} & \frac{\partial N_4}{\partial y} & \frac{\partial N_4}{\partial x} & & \frac{\partial N_8}{\partial y} & \frac{\partial N_8}{\partial x} \end{bmatrix} \tag{3.20}$$

In strain-displacement matrix, the coefficients can be transformed from one system to another system, e.g. global system to local system, or vice versa. The transformation relationship can be expressed as:

$$\begin{bmatrix} \dfrac{\partial N_i}{\partial x} \\ \dfrac{\partial N_i}{\partial y} \end{bmatrix} = [J]^{-1} \begin{bmatrix} \dfrac{\partial N_i}{\partial \xi} \\ \dfrac{\partial N_i}{\partial \eta} \end{bmatrix} \tag{3.21}$$

where [J] is the Jacobian matrix.

$$[J] = \begin{bmatrix} \dfrac{\partial x}{\partial \xi} & \dfrac{\partial y}{\partial \xi} \\ \dfrac{\partial x}{\partial \eta} & \dfrac{\partial y}{\partial \eta} \end{bmatrix} \tag{3.22}$$

and

$$[J]^{-1} = \begin{bmatrix} \dfrac{\partial \xi}{\partial x} & \dfrac{\partial \eta}{\partial x} \\ \dfrac{\partial \xi}{\partial y} & \dfrac{\partial \eta}{\partial y} \end{bmatrix} \tag{3.23}$$

3.1.4 Constitutive relations for elastoplasticity

As discussed in chapter 2, equations (2.14), (2.7) and (2.15) are actually the general forms of material constitutive laws. For plane strain elastoplasticity and/or axisymmetric problems, $\sigma_z \neq 0$, so we can simply append its correspondent component(s) to the end of equation (2.12) for easy programming.

$$[D] = \frac{E}{(1+\nu)(1-2\nu)} \begin{bmatrix} 1-\nu & \nu & & \nu \\ \nu & 1-\nu & & \nu \\ & & \dfrac{1-2\nu}{2} & \\ \nu & \nu & & 1-\nu \end{bmatrix} \tag{3.24}$$

For plane strain condition:

$$\{\sigma\} = \left[\sigma_x, \sigma_y, \tau_{xy}, \sigma_z\right]^T \tag{3.25}$$

$$\{\varepsilon\} = \left[\varepsilon_x, \varepsilon_y, \gamma_{xy}, \varepsilon_z\right]^T \tag{3.26}$$

For axisymmetric problems:

$$\{\sigma\} = \left[\sigma_r, \sigma_z, \tau_{rz}, \sigma_t\right]^T \tag{3.27}$$

$$\{\varepsilon\} = \left[\varepsilon_r, \varepsilon_z, \gamma_{rz}, \varepsilon_t\right]^T \tag{3.28}$$

3.1.5 Element equilibrium and stiffness matrix

Element equilibrium relations can be derived from the virtual work principle or from the potential energy theory (to distinguish the discussion in element or global domain, use superscript e to represent element domain) as:

$$\left[k^e\right]\cdot\left\{d^e\right\}=\left\{P^e\right\} \tag{3.29}$$

where $\left\{d^e\right\}$ is the element nodal displacement vector;

$\left\{P^e\right\}$ is the element total load vector, detailed discussion in the next section;

$[k^e]$ is the element stiffness matrix.

$$\left[k^e\right]=\int_V [B]^T [D][B]dV \tag{3.30}$$

where V stands for integration over element volume.

$$dV = tdxdy \tag{3.31}$$

where t is the thickness of the element, in plane strain problem, assuming t = 1.

To simplify the implementation in computer program, the stiffness matrix is usually expressed in local coordinates. Due to

$$dxdy = \left|J(\xi,\eta)\right| d\xi d\eta \tag{3.32}$$

So the element stiffness matrix can be expressed as:

$$\left[k^e\right]=t\int_{-1}^{1}\int_{-1}^{1}[B]^T [D][B]\left|J\right| d\xi d\eta \tag{3.33}$$

where $|J|$ is the determinant of Jacobian matrix, representing the distortion ratio of matrix transformation from global system to local system.

3.1.6 Load vector

The complete element (external) load vector is composed of the following components:

$$\left\{P^e\right\}=\left\{F^c\right\}+\left\{F^b\right\}+\left\{F^t\right\}+\left\{F^{\sigma^0}\right\}+\left\{F^{\varepsilon^0}\right\} \tag{3.34}$$

where

$\left\{F^c\right\}$ is the load vector due to concentrated nodal loads, e.g. mechanical rockbolts;

$\{F^b\}$ is the consistent load vector due to body forces, e.g. gravity induced force, in mining referred to as $\{P^g\}$;

$\{F^t\}$ is the consistent load vector due to boundary tractions, e.g. distributed loads;

$\{F^{\sigma^0}\}$ is the load vector due to initial stresses, e.g. *in situ* stresses (tectonic stresses) in mining problems;

$\{F^{\varepsilon^0}\}$ is the load vector due to initial strains or pre-stress forces, e.g. thermal stresses

Note that:

(a) For mining problems, the complete load vector is frequently taken into account in four parts—gravity; in situ stress; load from construction materials, such as backfill materials, shotcrete; load from pre-stress forces, such as pre-tensioned bolts.

(b) In finite element method, loads must be converted into nodal loads, called "equivalent loads".

For consistent load vector due to body force:

$$\{F^b\} = t\int_{-1}^{1}\int_{-1}^{1}[N]^T\{f\}|J|d\xi d\eta \tag{3.35}$$

where

$$\{f\} = [f_x, f_y]^T \tag{3.36}$$

For gravity induced force:

$$\{P_y^g\} = -\gamma\int_{V^e}[N]^T dV \tag{3.37}$$

or in local system:

$$\{P_y^g\} = -\gamma t\int_{-1}^{1}\int_{-1}^{1}[N]^T|J|d\xi d\eta \tag{3.38}$$

For initial stress induced loads:

$$\left\{F^{\sigma^0}\right\} = t\int_{-1}^{1}\int_{-1}^{1}[B]^T\left\{\sigma^0\right\}|J|d\xi d\eta \tag{3.39}$$

For in situ stress induced load vector in mining problems:

$$\left\{F^{\sigma^0}\right\} = -\int_{V^e}[B]^T\left\{\sigma^0\right\}dV = -t\int_{-1}^{1}\int_{-1}^{1}[B]^T\left\{\sigma^0\right\}|J|d\xi d\eta \tag{3.40}$$

where

$$\left\{\sigma^0\right\} = \begin{Bmatrix}\sigma_x^0 \\ \sigma_y^0 \\ \tau_{xy}^0\end{Bmatrix} = \begin{Bmatrix}\sum_{i=1}^{n} N_i\sigma_{x,i}^0 \\ \sum_{i=1}^{n} N_i\sigma_{y,i}^0 \\ \sum_{i=1}^{n} N_i\tau_{xy,i}^0\end{Bmatrix} \tag{3.41}$$

For traction induced load vector over area S_e:

$$\left\{F^t\right\} = \int_{S_e}[N]^T\{T\}\,dS \tag{3.42}$$

For initial strain induced load vector within volume V_e:

$$\left\{F^{\varepsilon^0}\right\} = \int_{V_e}[B]^T[D]\{\varepsilon_0\}\,dV \tag{3.43}$$

Within element, the internal force vector represents the loads at nodes caused by the material strains, which can be calculated by

$$\left\{r^{\text{int}}\right\} = \int_V [B]^T\{\sigma\}\,dV \tag{3.44}$$

For linearly elastic material behaviour, equation (3.44) can be simplified as:

$$\left\{r^{\text{int}}\right\} = \left[k^e\right]\{d\} \tag{3.45}$$

3.1.7 Numerical integration

Numerical integration is used to obtain numerical estimate of complex integrals. It is based on passing a polynomial in each dimension through a certain number of points, called sampling points, and multiplying a weighting factor at each point, then summing up the quantities to evaluate the integral. Gauss quadrature is the most popular numerical integration scheme.

For a one dimensional Gauss quadrate, if $I = \int_{x_1}^{x_2} f(x)dx$ becomes $I = \int_{-1}^{1} \phi(\xi)d\xi$, then we have general quadrature formula:

$$I = \int_{-1}^{1} \phi(\xi)d\xi \approx W_1\phi_1 + W_2\phi_2 + \cdots + W_n\phi_n = \sum_{i=1}^{n} W_i\phi_i \tag{3.46}$$

Figure 3.4 illustrates the sampling locations and weighting factors of one dimension Gauss quadrature with three sampling points.

Similarly, for a two dimensional problem, if $I = \int_{y_1}^{y_2}\int_{x_1}^{x_2} f(x,y)dxdy$, then we have

$$I = \int_{-1}^{1}\int_{-1}^{1} \phi(\xi,\eta)d\xi d\eta \approx \sum_{i=1}\sum_{j=1} W_i W_j \phi(\xi_i,\eta_j) \tag{3.47}$$

For example, for a four-node isoparametric quadrilateral element in 2D problems, at four Gauss sampling points (see Figure 3.5), all the weighting factors equal to 1, and

$$I = \phi_1 + \phi_2 + \phi_3 + \phi_4 \tag{3.48}$$

Newton-Cotes quadrature is another frequently used integration scheme. Comparing with Gauss quadrature, Newton-Cotes quadrature uses sampling points at the element boundary.

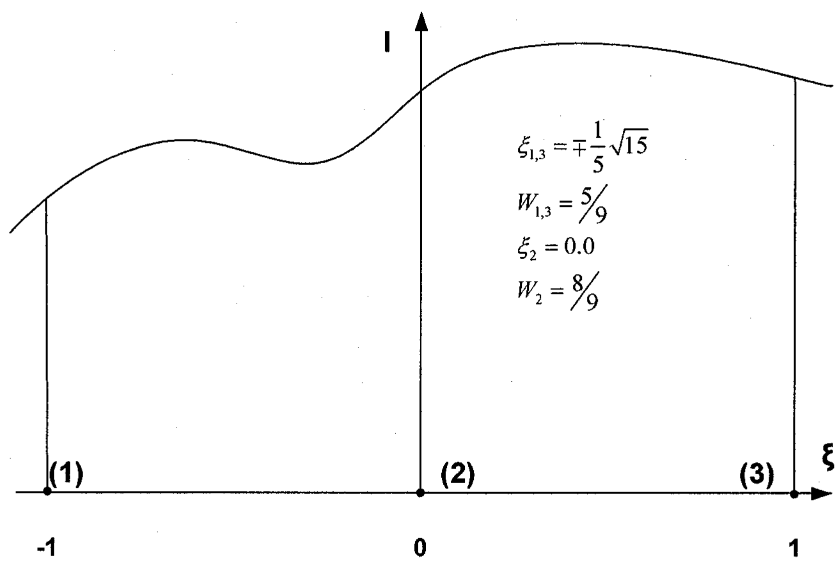

Figure 3. 4 Three sampling points and weighting factors for line element

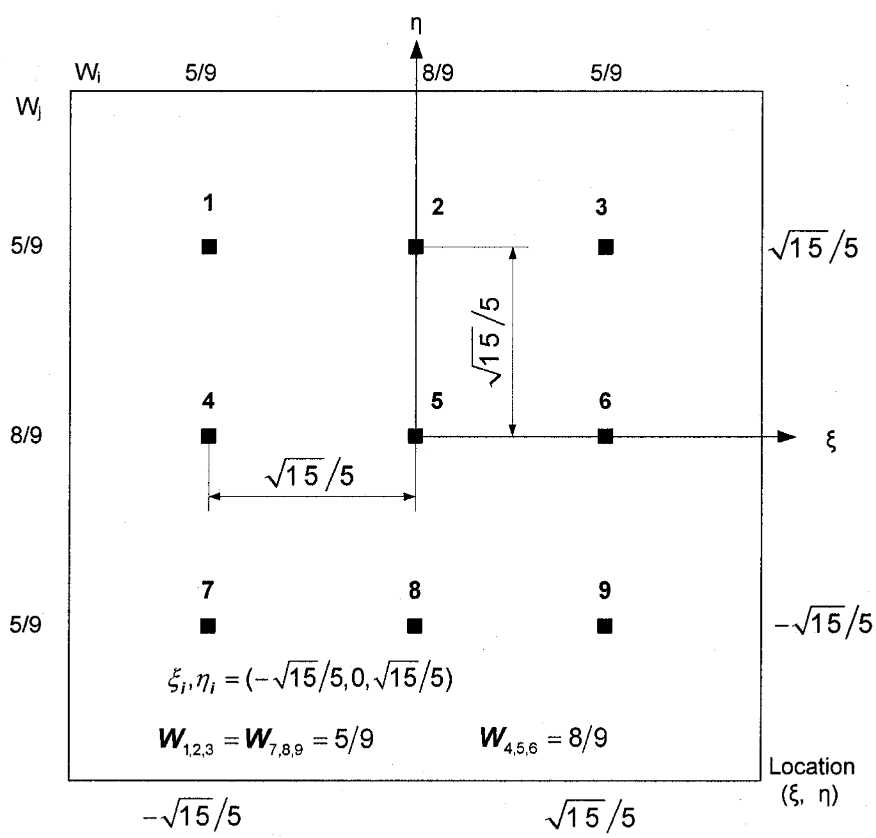

Figure 3. 5 Nine sampling points of quadrilateral element

3.1.8 Summary of finite element equations for solids

Stiffness matrix

$$\left[k^e\right] = \iint [B]^T [D][B] dxdy \tag{3.49}$$

Mass matrix

$$[m^e] = \rho \iint [N]^T [N] dxdy \tag{3.50}$$

Static Equilibrium

$$\left[k^e\right]\left\{d^e\right\} = \left\{f^e\right\} \tag{3.51}$$

Incremental form

$$\left[k^e\right]\left\{\Delta d^e\right\} = \left\{\Delta f^e\right\} \tag{3.52}$$

and

$$\left\{d\right\}_1 = \left\{d\right\}_0 + \left\{\Delta d\right\} \tag{3.53}$$

In 2D problems, for quadrilateral elements, we can use numerical integration approach, as following (Smith & Griffiths, 2004):

$$\int_{-1}^{1}\int_{-1}^{1} f(\xi,\eta)|J| d\xi d\eta \approx \sum_{i=1}^{n}\sum_{j=1}^{n} w_i w_j f(\xi_i,\eta_j) \tag{3.54}$$

When n = 2, numerical integration can get exact solution for cubic functions in Gauss sampling points. When n = 3, numerical integration gives exact solution for quintic functions in Gauss sampling points. So for two-point Gaussian quadrature in each direction leads in most cases to accurate estimates of the stiffness matrix of a four-node quadrilateral element. A compromise approach is to evaluate the contribution to the stiffness matrix coming from each of the four "Gauss-Points" algebraically and add them together. Thus:

$$\left[k^e\right] \approx \sum_{i=1}^{nip} W_i |J|_i \left([B]^T [D][B]\right)_i \tag{3.55}$$

3.2 Algorithms for solving nonlinear finite element equations

3.2.1 Introduction

For a nonlinear analysis, the difficulty is the path-dependent stiffness in equations (3.51), (3.52) and (3.53). In order to arrive at a solution a linearized increment approach, or a trial and error process, or a combined incremental iterative scheme, is needed.

In practical finite element analysis, there are two main categories of solution procedures. One is called secant approach, another is called tangent approach. The latter further divides into two methods: Newton-Raphson method, or variable stiffness method; and Modified Newton-Raphson method, or initial stiffness method.

3.2.2 Secant approach

In this method, as illustrated in Figure 3.6, the initial global stiffness is first calculated. Based on the applied force, the displacements are calculated and used to update the global stiffness and a new set of displacements. That is,

$$\{u\}^{i+1} = [K_s(u^i)]^{-1}\{F\}^{i+1} \tag{3.56}$$

where i and (i+1) stand for i^{th} and $(i+1)^{th}$ iterations.

3.2.3 Tangent approach

3.2.3.1 Newton-Raphson method

For Newton-Raphson method or tangent stiffness method, as illustrated in Figure 3.7, the tangent stiffness matrix, $[K_t]$, and the load imbalance $\{\Delta R\}$ are updated after each iteration. The solution process seeks to reduce the load imbalance, $\{\Delta R\}$, and displacement increment, $\{\Delta d\}$, to zero or a certain tolerance. In multiple d.o.f case, Newton-Raphson method involves repeated solutions of the equations

$$[K_t]^i\{\Delta d\}^{i+1} = \{\Delta R\}^{i+1} \tag{3.57}$$

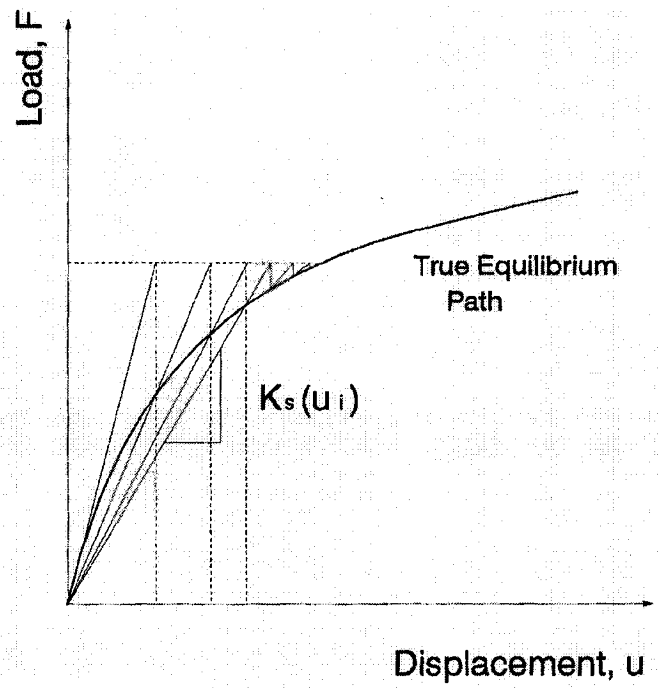

Figure 3. 6 The secant iterative method (Chan & Chui, 2000)

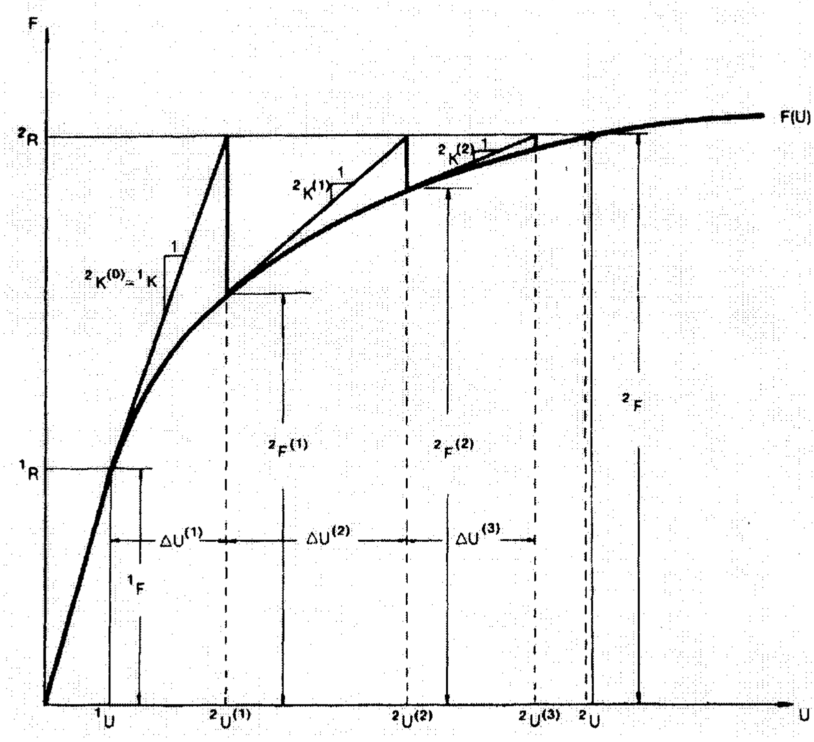

Figure 3. 7 Newton-Raphson method (Chen & Han, 1988)

3.2.3.2 Modified Newton-Raphson method

The Modified Newton-Raphson method, as illustrated in Figure 3.8, involves "constant stiffness" iterations. The global stiffness matrix is formed only once. For each iteration, only the global "load" vector is modified. So it is also called initial stiffness method.

It can be seen from Figure 3.8 that the Modified Newton-Raphson method may require more iterations as failure approaches because the initial stiffness overestimates or underestimates the actual material stiffness. But it has the advantage of stability when approached to failure. Thus it can be used in the problems of perfect plasticity, hardening, softening and creep problems.

On the other hand, Newton-Raphson method needs less iteration in that it takes into account the reduction of material stiffness as failure is approached, but the extra cost of reforming the global stiffness matrix is offset by the reduced number of iterations. Especially as failure is approached, the very small stiffness could lead the system unstable (Mitri, 2005).

3.2.3.3 Combined Newton-Raphson Method

As discussed previously, Newton-Raphson method and Modified Newton-Raphson method both have pros and cons. In practice, especially in simulating sequenced mining problems or staged underground openings, one can combine these two methods to retain their advantages and discard their disadvantages. That is periodically updating the global stiffness matrix to reduce total iterations and speedup convergence, and incrementally varying "right-hand side", or "loads" in each stage to stabilize the stiffness and conform to different nonlinear problems. Figure 3.9 symbolically shows this scheme.

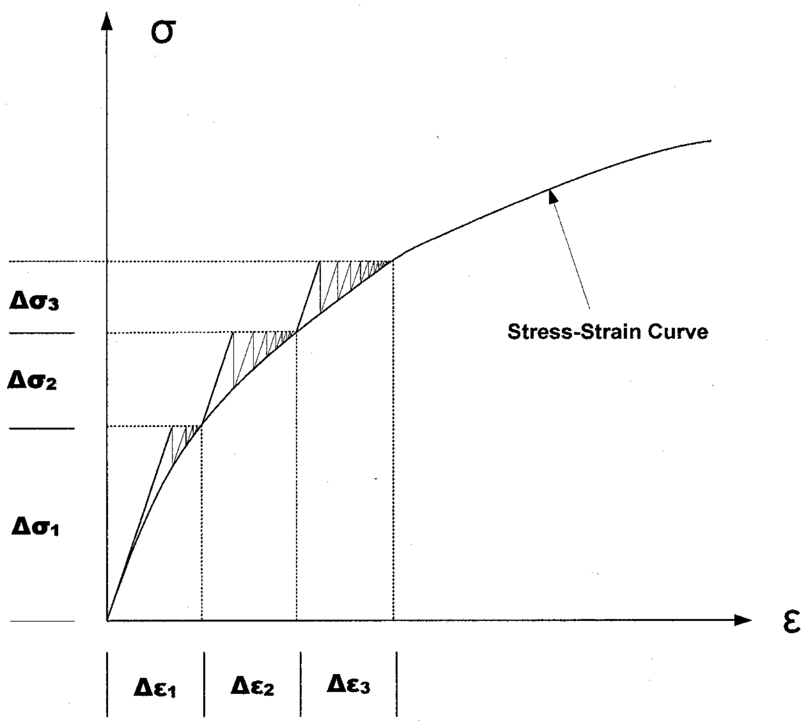

Figure 3. 8 Modified Newton-Raphson method

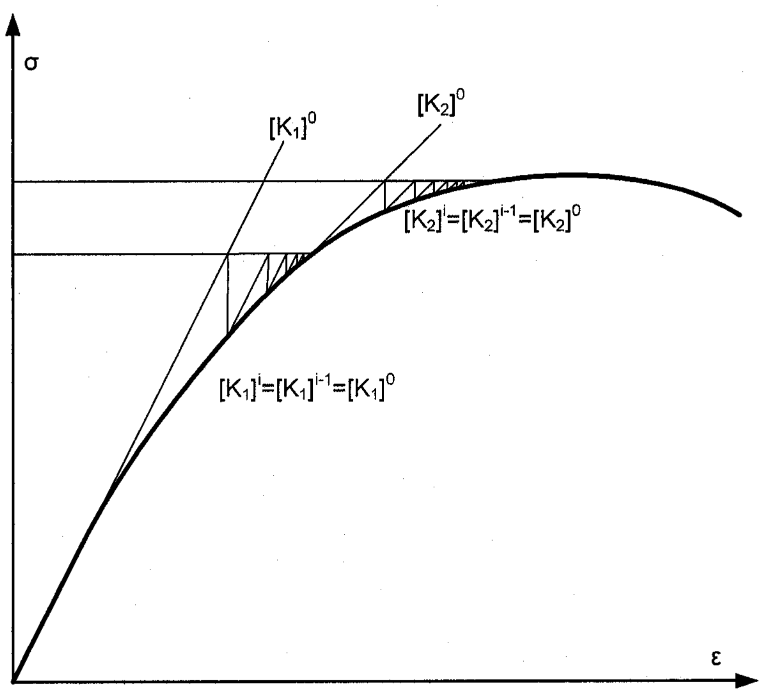

Figure 3. 9 Combined Newton-Raphson Method

3.2.4 Implementation of initial stiffness method

3.2.4.1 Generation of excavation loads

As discussed in preceding sections, initial stiffness method essentially uses repeated elastic solutions to achieve the final solutions by iteratively varying the right hand loads in the system. In underground mining problems, the right hand loads are excavation loads.

It is known that in natural state, the rock mass is in a state of equilibrium and subjected to initial stresses. After the mining activities started, rock materials are removed and underground openings are created. The initial stress state is disturbed and needs to redistribute around the underground excavations. Suppose that unit E with volume V_E will be excavated, and material unit weight is γ and [N] is the element shape function. To achieve a new equilibrium state, the excavation loads, $\{F_{BE}\}$, should act on excavation boundary. According to the third Newton's law, $\{F_{BE}\}$ equals to $\{F_{EB}\}$ which comes from initial stresses and body loads (gravity loads in this case) of the excavated units E, but the directions are opposite. So we have

$$\{F_{BE}\} = -\int_{V_E}[B]^T\{\sigma_E^0\}dV_E + \gamma\int_{V_E}[N]^T dV_E = (\{F^{\sigma^0}\} + \{P^g\}) \tag{3.58}$$

From equation (3.37) or (3.38) and (3.39) or (3.40), we can calculate $\{P^g\}$ and $\{F^{\sigma^0}\}$. From equation (3.58) we can see that the first part of right hand side does not change and only the second part of the right hand side, body load vector, or gravity load vector varies from one iteration to the next.

There are two commonly used methods to generate the body loads: initial strain method and initial stress method.

3.2.4.2 Initial stress method

Initial stress method (Zienkiewicz, Valliappan, & King, 1968) is more commonly used conventional method when dealing with nonlinear problems. Griffiths (1988) further developed this approach that the global stiffness matrix is formed only once, with the non-linearity introduced by iteratively modifying the applied forces on the structure until convergence is achieved.

Assuming that at material yielding, the strains will contain both elastic and plastic components, that is:

$$\{\varepsilon\} = \{\varepsilon^e\} + \{\varepsilon^p\} \tag{3.59}$$

or incremental form

$$\{d\varepsilon\} = \{d\varepsilon^e\} + \{d\varepsilon^p\} \tag{3.60}$$

In modified Newton-Raphson method, it is only the elastic strain increment $\{\Delta\varepsilon^e\}$ that generates stresses through the elastic stress-strain relation, thus

$$\begin{aligned} \{d\sigma\} &= \left[D^e\right]\{d\varepsilon^e\} \\ &= \left[D^e\right](\{d\varepsilon\} - \{d\varepsilon^p\}) \end{aligned} \tag{3.61}$$

But in initial stress method, this involves an explicit relationship between increments of stress and increments of strain. Thus, the linear elasticity was still described by above equation, whereas elastoplasticity is described by

$$\{d\sigma\} = \left[D^{ep}\right]\{d\varepsilon^e\} \tag{3.62}$$

where

$$[D^{ep}] = [D^e] - [D^p] \tag{3.63}$$

Now we can derive $[D^p]$ as follows:

Classical plasticity theory describes that plastic strain increments are normal to the yield surface, F, thus

$$\left\{d\varepsilon^p\right\} = \lambda\left\{\frac{\partial F}{\partial \sigma}\right\} \tag{3.64}$$

where λ is a plastic scalar multiplier.

For frictional materials, e.g. rocks, concretes and drained soils, plastic strain increments are normal to the plastic potential surface, Q, thus

$$\left\{d\varepsilon^{p}\right\}=\lambda\left\{\frac{\partial Q}{\partial \sigma}\right\} \tag{3.65}$$

so

$$\{d\sigma\}=\left[D^{e}\right](\{d\varepsilon\}-\lambda\left\{\frac{\partial Q}{\partial \sigma}\right\}) \tag{3.66}$$

For a perfect plastic material, on the yield surface

$$\left\{\frac{\partial F}{\partial \sigma}\right\}^{T}\{d\sigma\}=0 \tag{3.67}$$

Substitute (3.66) into (3.67), then

$$\lambda=\frac{\left\{\frac{\partial F}{\partial \sigma}\right\}^{T}\left[D^{e}\right]\{d\varepsilon\}}{\left\{\frac{\partial F}{\partial \sigma}\right\}^{T}\left[D^{e}\right]\left\{\frac{\partial Q}{\partial \sigma}\right\}} \tag{3.68}$$

Substitute (3.68) into (3.66), thus

$$\{d\sigma\}=(\left[D^{e}\right]-\frac{\left[D^{e}\right]\left\{\frac{\partial Q}{\partial \sigma}\right\}\left\{\frac{\partial F}{\partial \sigma}\right\}^{T}\left[D^{e}\right]}{\left\{\frac{\partial F}{\partial \sigma}\right\}^{T}\left[D^{e}\right]\left\{\frac{\partial Q}{\partial \sigma}\right\}})\{d\varepsilon\} \tag{3.69}$$

Compare (3.69) with (3.62) and (3.63), so

$$\left[D^{ep}\right]=\left[D^{e}\right]-\frac{\left[D^{e}\right]\left\{\frac{\partial Q}{\partial \sigma}\right\}\left\{\frac{\partial F}{\partial \sigma}\right\}^{T}\left[D^{e}\right]}{\left\{\frac{\partial F}{\partial \sigma}\right\}^{T}\left[D^{e}\right]\left\{\frac{\partial Q}{\partial \sigma}\right\}} \tag{3.70}$$

and

$$\left[D^{p}\right]=\frac{\left[D^{e}\right]\left\{\frac{\partial Q}{\partial \sigma}\right\}\left\{\frac{\partial F}{\partial \sigma}\right\}^{T}\left[D^{e}\right]}{\left\{\frac{\partial F}{\partial \sigma}\right\}^{T}\left[D^{e}\right]\left\{\frac{\partial Q}{\partial \sigma}\right\}} \tag{3.71}$$

According to Griffiths (Griffiths & Willson, 1986), for Mohr-Coulomb materials with plane strain plastic problems

$$\left\{\frac{\partial F}{\partial \sigma}\right\} = \begin{Bmatrix} \sin\phi + k_1 \sin\alpha \\ \sin\phi - k_1 \sin\alpha \\ 2k_2 \cos\alpha \\ 0 \end{Bmatrix} \tag{3.72}$$

$$\left\{\frac{\partial Q}{\partial \sigma}\right\} = \begin{Bmatrix} \sin\psi + k_1 \sin\alpha \\ \sin\psi - k_1 \sin\alpha \\ 2k_2 \cos\alpha \\ 0 \end{Bmatrix} \tag{3.73}$$

where

$$k_1 = \begin{cases} 1 & if \quad |\sigma_y| \geq |\sigma_x| \\ -1 & if \quad |\sigma_y| < |\sigma_x| \end{cases}$$

$$k_2 = \begin{cases} 1 & if \quad \tau_{xy} \geq 0 \\ -1 & if \quad \tau_{xy} < 0 \end{cases}$$

$$\alpha = \arctan\left|\frac{\sigma_x - \sigma_y}{2\tau_{xy}}\right|$$

The body loads in the stress redistribution process are reformed at each iteration for all elements that possess yielding Gauss points, thus

$$\{F_b\}^i = \sum_{n=1}^{all\_element} \iint [B]^T [D^p] \{d\varepsilon\}^i \, dxdy \tag{3.74}$$

3.2.4.3 Initial strain method

This method is based on viscoplasticity theory. According to Zienkiewicz (Zienkiewicz & Cormeau, 1974), materials are allowed to sustain stress state outside the failure criterion (i.e. F > 0) for finite time periods; then the stress state will redistribute.

The viscoplastic strain rates can be expressed as

$$\{\dot{\varepsilon}^{vp}\} = F\left\{\frac{\partial Q}{\partial \sigma}\right\} \tag{3.75}$$

where F is the yield function and Q is the plastic potential function.

The increment of viscoplastic strain within a pseudo-time step is calculated by

$$d\varepsilon^{vp} = \Delta t\{\dot{\varepsilon}^{vp}\} \tag{3.76}$$

The iteration form from previous accumulated viscoplastic strain, $\{\Delta\varepsilon^{vp}\}^{i-1}$, to the next time step, i.

$$\{\Delta\varepsilon^{vp}\}^{i} = \{\Delta\varepsilon^{vp}\}^{i-1} + \{d\varepsilon^{vp}\}^{i} \tag{3.77}$$

The upper bound limit of the time step Δt for unconfined numerical stability has been derived by Cormeau (1975), which is dependent on the applied failure criterion. For Mohr-Coulomb materials:

$$\Delta t = \frac{4(1+\nu)(1-2\nu)}{E(1-2\nu+\sin^2\phi)} \tag{3.78}$$

The derivatives of the plastic potential function Q with respect to stresses are expressed through the Chain Rule as:

$$\left\{\frac{\partial Q}{\partial \sigma}\right\} = \frac{\partial Q}{\partial \sigma_m}\left\{\frac{\partial \sigma_m}{\partial \sigma}\right\} + \frac{\partial Q}{\partial J_{2D}}\left\{\frac{\partial J_{2D}}{\partial \sigma}\right\} + \frac{\partial Q}{\partial J_{3D}}\left\{\frac{\partial J_{3D}}{\partial \sigma}\right\} \tag{3.79}$$

And the viscoplastic strain rate in equation (3.75) can be evaluated numerically by following form of expression:

$$\{\dot{\varepsilon}^{vp}\} = F\left(\frac{\partial Q}{\partial \sigma_m}\left[M^1\right] + \frac{\partial Q}{\partial J_{2D}}\left[M^2\right] + \frac{\partial Q}{\partial J_{3D}}\left[M^3\right]\right)\{\sigma\} \tag{3.80}$$

This is essentially the notation used by Zienkiewicz and Cormeau (Zienkiewicz & Cormeau, 1975), and Zienkiewicz and Taylor (Zienkiewicz & Taylor, 1989).

For Mohr-Coulomb materials in 2D problems:

If $|\sin\theta| \le 0.49$, regular expressions are adopted.

$$\frac{\partial Q}{\partial \sigma_m} = \sin\psi$$

$$\frac{\partial Q}{\partial J_{2D}} = \frac{\cos\theta}{\sqrt{2}t}\left(1+\tan\theta\tan 3\theta + \frac{\sin\psi}{\sqrt{3}}(\tan 3\theta - \tan\theta)\right)$$

$$= \frac{\sqrt{3}\cos\theta}{2\bar{\sigma}}\left(1+\tan\theta\tan 3\theta + \frac{\sin\psi}{\sqrt{3}}(\tan 3\theta - \tan\theta)\right) \qquad (3.81)$$

$$\frac{\partial Q}{\partial J_{3D}} = \frac{\sqrt{3}\sin\theta + \sin\psi\cos\theta}{t^2\cos 3\theta}$$

$$= \frac{3}{2\bar{\sigma}^2}\frac{\sqrt{3}\sin\theta + \sin\psi\cos\theta}{\cos 3\theta}$$

If $|\sin\theta| > 0.49$, following expressions are adopted.

$$\frac{\partial Q}{\partial \sigma_m} = \sin\psi$$

$$\frac{\partial Q}{\partial J_{2D}} = \frac{1}{2\sqrt{2}t}\left(\sqrt{3} \pm \frac{\sin\psi}{\sqrt{3}}\right) \qquad (3.82)$$

$$= \frac{1}{4\bar{\sigma}}(3 \pm \sin\psi)$$

$$\frac{\partial Q}{\partial J_{3D}} = 0$$

where

$$[M^1] = \frac{1}{9\sigma_m}\begin{bmatrix} 1 & 1 & 0 & 1 \\ 1 & 1 & 0 & 1 \\ 0 & 0 & 0 & 0 \\ 1 & 1 & 0 & 1 \end{bmatrix}$$

$$[M^2] = \frac{1}{3}\begin{bmatrix} 2 & -1 & 0 & -1 \\ -1 & 2 & 0 & -1 \\ 0 & 0 & 6 & 0 \\ -1 & -1 & 0 & 2 \end{bmatrix} \qquad (3.83)$$

$$[M^3] = \frac{1}{3}\begin{bmatrix} s_x & s_z & \tau_{xy} & s_y \\ s_z & s_y & \tau_{xy} & s_x \\ \tau_{xy} & \tau_{xy} & -3s_z & -2\tau_{xy} \\ s_y & s_x & -2\tau_{xy} & s_z \end{bmatrix}$$

Similarly, the body loads are also accumulated at each time step within each load step based on previous iteration for all elements containing yield Gauss points.

$$\{F_b\}^i = \{F_b\}^{i-1} + \sum_{elements}^{all} \iint [B]^T [D^e] \{\Delta\varepsilon^{vp}\}^i \, dxdy \tag{3.84}$$

Initial strain method not only has the identical results with initial stress method, but also has the advantage of unified approach to problems of elastoplasticity, viscosity and creep.

3.2.5 Convergence criteria

A properly defined convergence criterion to terminate the equilibrium iterations is an essential part of solving elastoplastic problems. In the end of each iteration, the solutions obtained must be checked against a prescribed tolerance. Three methods are frequently used.

3.2.5.1 Displacement criterion

Displacement criterion is based on the nodal displacement changes on a particular iteration, *i*, compared with total accumulated displacements in a given step, *m*. It can be expressed as (Owen and Hinton, 1980):

$$\frac{\left|\{\Delta d\}_m^i\right|}{\left|\{d\}_m^i - \{d\}_{m-1}\right|} \times 100\% \le Tolerance \tag{3.85}$$

3.2.5.2 Load criterion

Load criterion is based on the nodal residual force changes on a particular iteration, *i*, compared with total residual forces in a given step, *m*. It can be expressed as (Owen and Hinton, 1980):

$$\frac{\left|\{\Delta R\}_m^i\right|}{\left|\{R\}_m^i - \{R\}_{m-1}\right|} \times 100\% \le Tolerance \tag{3.86}$$

Tolerance should be carefully chosen. "A too loose tolerance will lead to an inaccurate result, while a too tight tolerance may lead to wasteful computation to obtain a needless accuracy" (Chen & Han, 1988). In rock engineering, *tolerance = 0.1-1.0* is suitable. For most of rock engineering simulations, *tolerance = 1.0* is good enough.

3.2.5.3 Energy criterion

Energy criterion combines previous two criteria. It is based on the work done by the out-of-balance forces (residual forces) in the i^{th} iteration through the incremental displacements compared with the initial internal energy increment in the first iteration (Mitri & Hassani, 1988). That is

$$\frac{\{\Delta R_m^i\}^T\left\{\Delta d_m^i\right\}}{\{\Delta R_m^1\}^T\left\{\Delta d_m^1\right\}}\times 100\% \leq Tolerance \tag{3.87}$$

Typically, $Tolerance = 0.1$ is suitable for the majority of rock engineering problems.

3.2.6 Factor of safety

3.2.6.1 ez-tools approach

Using rock failure criteria to check the stress level is a widely used approach by rock mechanics specialists, particularly in hard rock applications. In linear elastic mode, ez-tools uses the ratio of the rock mass strength ($S_{\max}$) to the applied stress (S) around underground openings to calculate the safety level, called factor of safety or safety level (Mitri & Tang, 2003). That is:

$$FS = \frac{S_{\max}}{S} \tag{3.88}$$

The rock mass strength ($S_{\max}$) and the applied stress (S) are failure criterion/model dependent. ez-tools implemented five failure criteria, and the calculation formula are summarized in Table 3-1.

If $FS > 1$, it is safe; if $FS = 1$, it is in critical state; if $FS < 1$, it is unsafe.

Table 3- 1 Factor of safety calculation formula in ez-tools (Mitri & Tang, 2003)

Criterion	S_{max}	S	Note	Significance
Mohr-Coulomb	$c+\sigma_n \tan\phi$	$\frac{\sigma_1-\sigma_3}{2}\cos\phi$		Comparison of shear strength of the material (or equivalent) to the maximum applied shear stress
Drucker-Prager	$k-\alpha J_1$	$\sqrt{J_{2D}}$	k and α are compression cone constants	
Hoek-Brown	$\sqrt{m\sigma_c\sigma_3+s\sigma_c^2}$	$\sigma_1-\sigma_3$		
Bieniawski (Bieniawski, 1973)	$a+b\left(\frac{\sigma_3}{\sigma_c}\right)^\alpha-\frac{\sigma_3}{\sigma_c}$	$\frac{\sigma_1-\sigma_3}{\sigma_c}$	a, b, and α are Bieniawski material constants	
Tensile strength	σ_t	σ_3	Used when a stress state contains one or more principal stresses in tension for above criteria	

3.2.6.2 Phase² approach

As shown in Figure 3.10, factor of strength, FS, can be calculated as (Phase 2 v6.0 documentation):

$$FS=\frac{T_{max}}{T} \tag{3.89}$$

where

$$T_{max}=-\frac{\sigma_m\sin\phi-c\cos\phi}{\cos\theta-\frac{\sin\theta\sin\phi}{\sqrt{3}}} \tag{3.90}$$

$$T=\sqrt{J_{2D}}=\frac{t}{\sqrt{2}} \tag{3.91}$$

If FS > 1, the stress state is in elastic region of the material; if FS = 1, the material is yield.

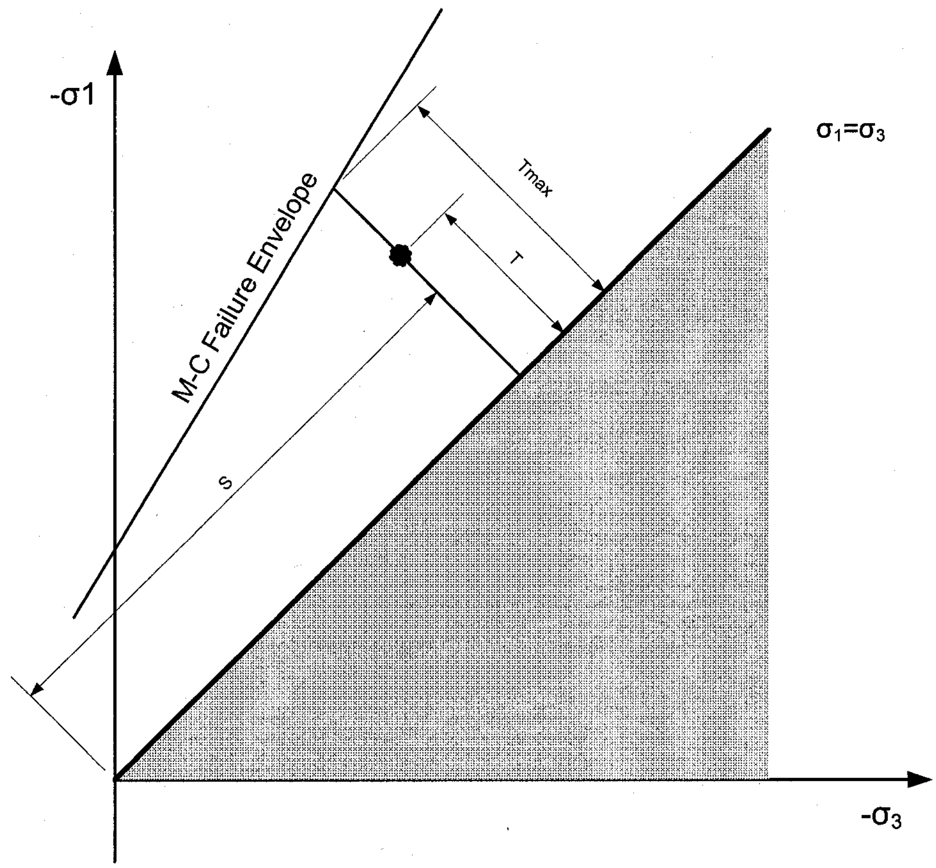

Figure 3. 10 Illustration of Factor of Strength for 2D problems in Phase 2

Chapter 4 Characteristic Model for Mine Haulage Drift

4.1 Introduction to sublevel stoping method

Sublevel stoping method, or blasthole stoping method, is a general term applied to vertical mining methods in which a large open stope is created in the ore body. Due to the reason of patent, sublevel stoping method has many variations. In this method, a stope is often large, with largest dimensions in vertical direction. This non-entry open stope serves as the free space for subsequent ore blasting. Mining activities such as drilling and blasting are conducted in the sublevels within the ore block. Based on the drill patterns and blasting directions, there are three main different sublevel stoping variations in Canadian underground mines.

The first method is the traditional one which is called blasthole stoping. With this method, the drilling from the sublevel can be fan shape (Figure 4.1) or ring shape (Figure 4.2). After creating a vertical slot by blasting, larger amounts of ore are blasted in vertical slices. Blasted slices of ore fall into an open void within the open stope.

The second method called longhole stoping method is shown in Figure 4.3. With this method, the drill pattern is parallel holes and the width of the sublevels is the same as the width of the stope. Mining sequence is similar to the blasthole stoping.

The third method is known as VCR (vertical crater retreat) or VRM (vertical retreat method), originally developed by Canadian mining company Inco, as shown in Figure 4.4. This method uses similar drill pattern with longhole stoping method, but the ore is blasted in horizontal slices.

After the ore is recovered from the sublevel open stope, the void is backfilled with cemented backfill for primary stope or non-cemented backfill for secondary stope, called delayed backfill.

To maintain better ground conditions, the stoping sequence in longitudinal direction is to maintain a doom shape mining front. Figure 4.5 shows the typical open stope mining sequence in longitudinal direction in Bousquet 2 mine.

Sublevel stoping method is used in the following conditions:

- Ore and wall rocks are relatively strong;
- The orebody is steeply dipping;
- The orebody has regular boundaries;
- The largest dimension is normally the vertical.

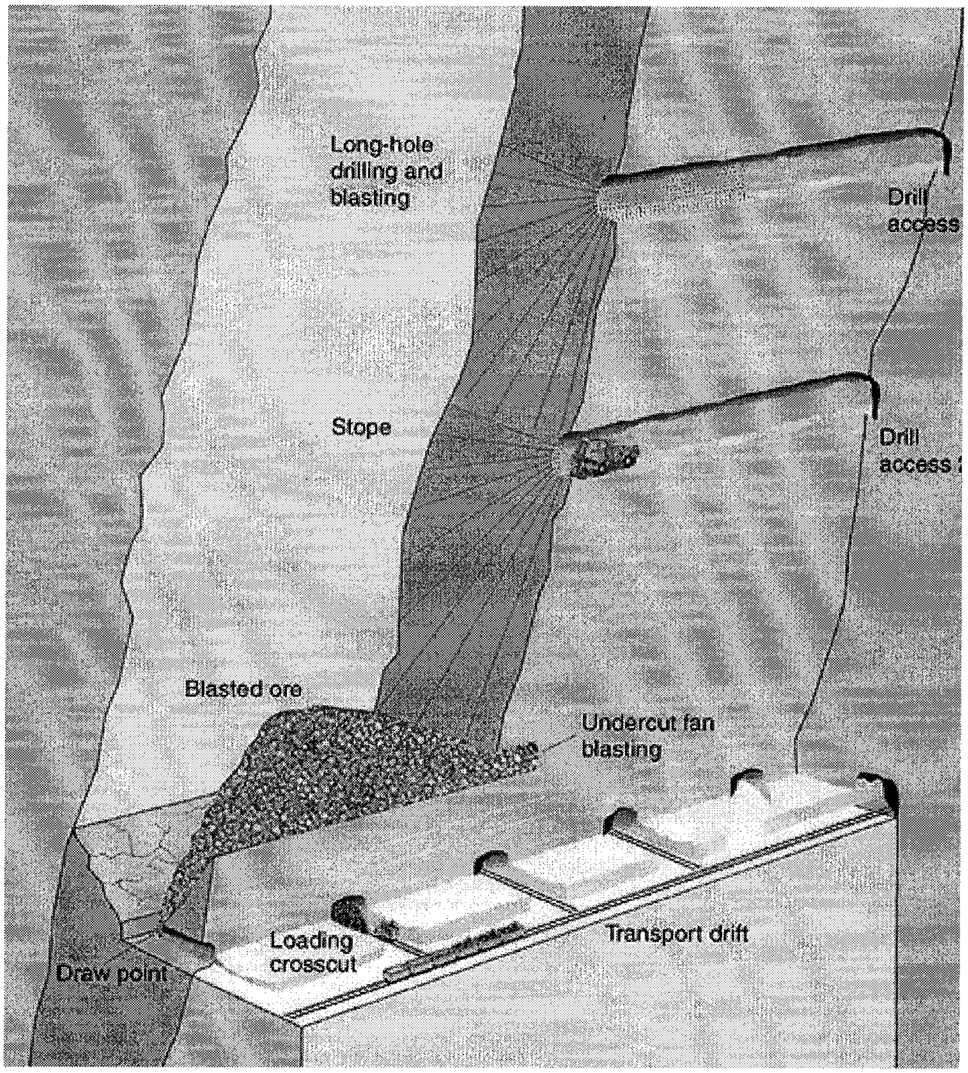

Figure 4. 1 Fan pattern blasthole stoping method-I (AtlasCopco, 2005)

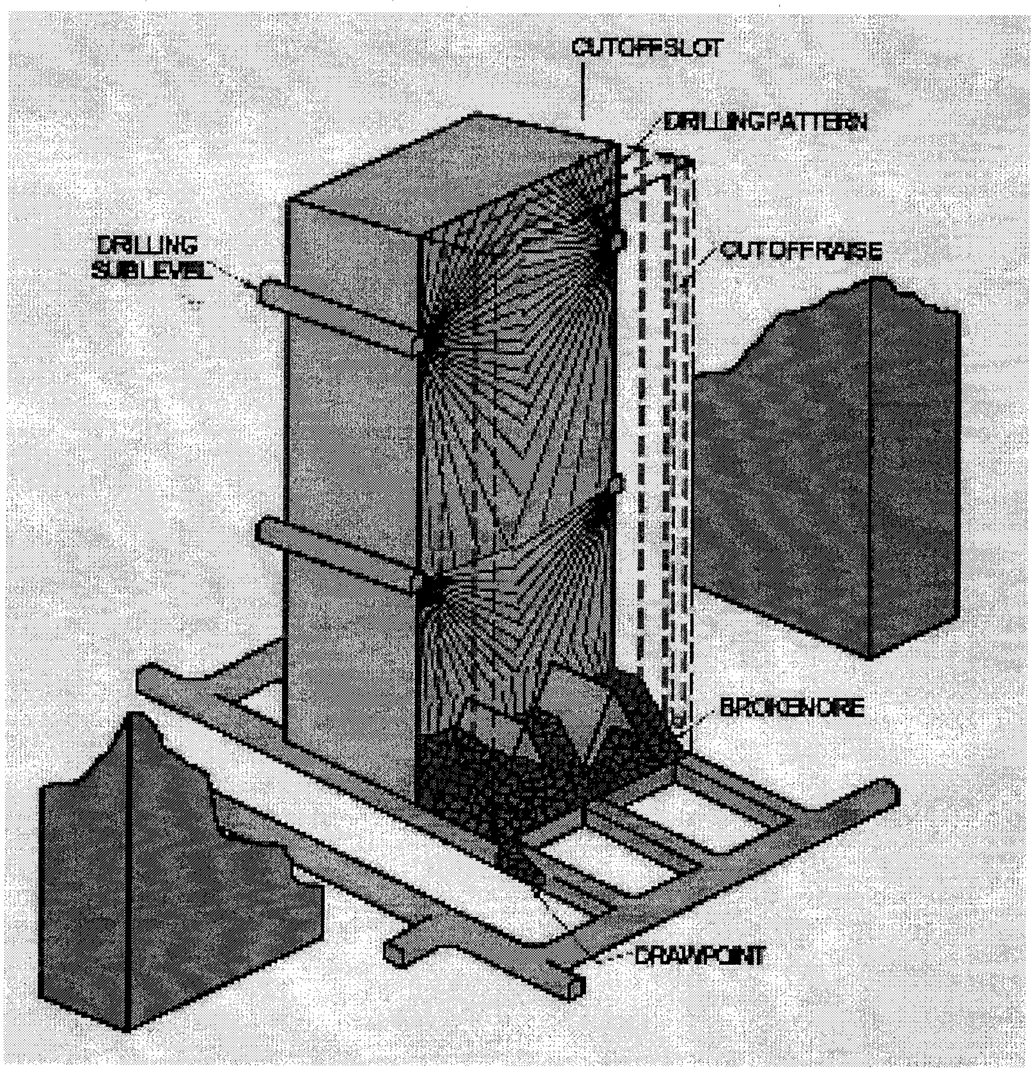

Figure 4. 2 Fan pattern blasthole stoping method-II
(Grant and DeKruijff, 2000)

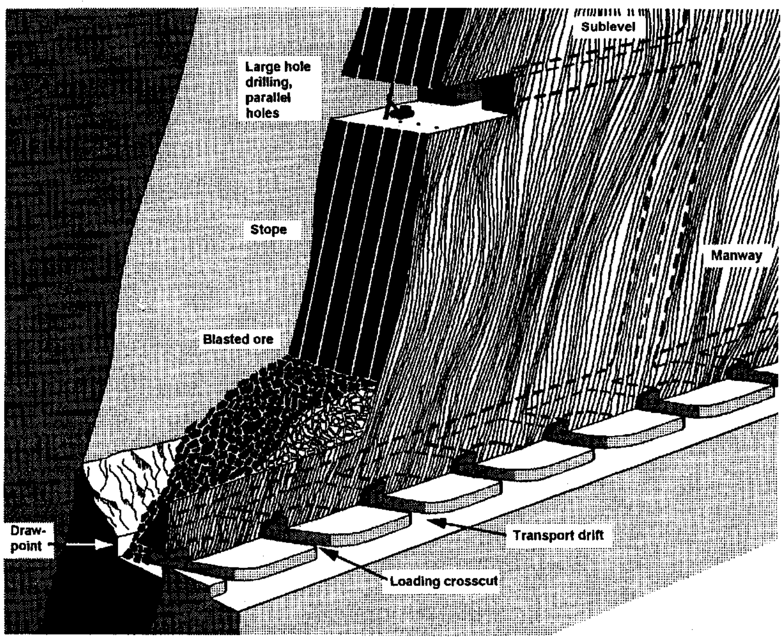

Figure 4. 3 Longhole stoping method (Hamrin, 2001)

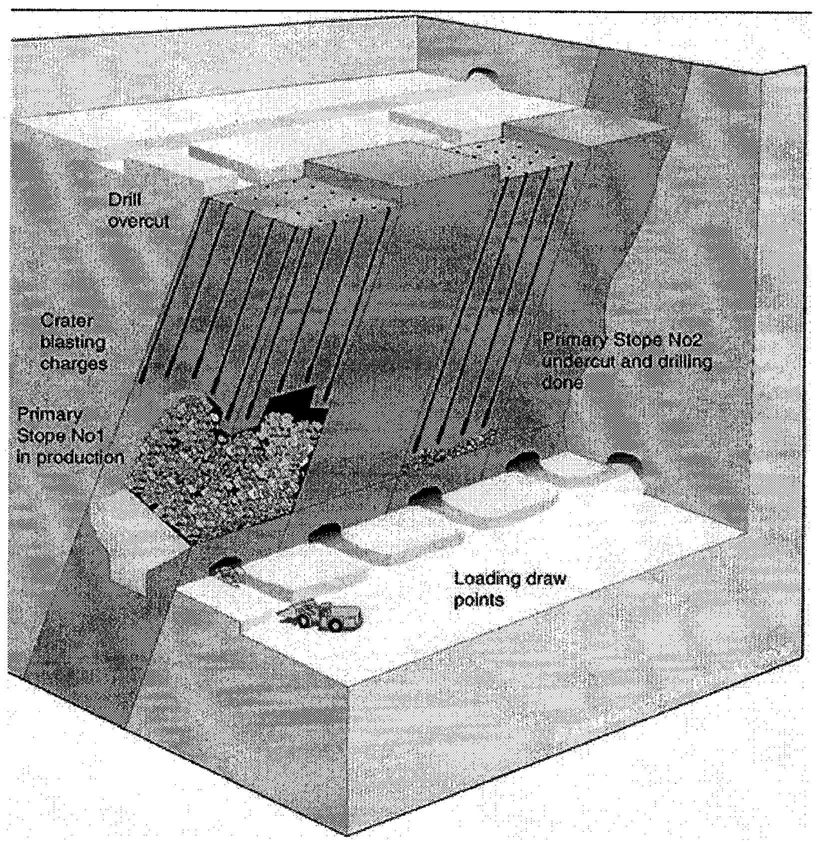

Figure 4. 4 VCR method (primary stope) (AtlasCopco, 2005)

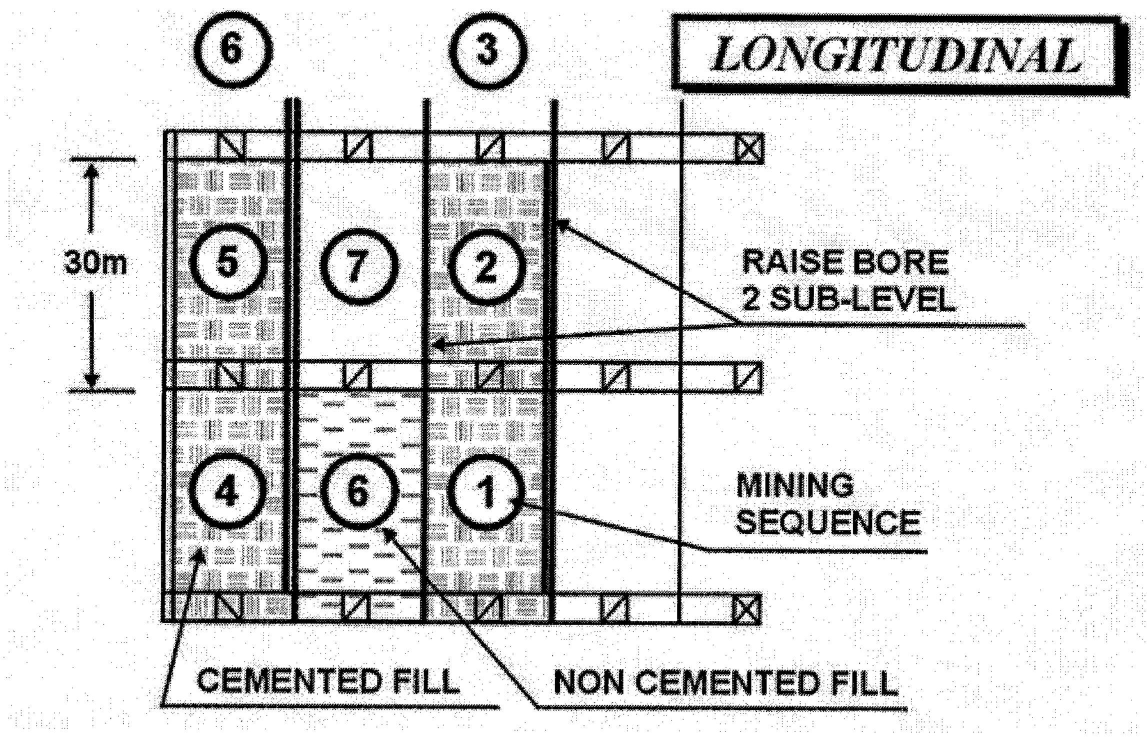

Figure 4. 5 Bousquet 2 Mine's open stope mining pattern in longitudinal direction (Henning, 1998)

As can be seen, haulage drifts play an import role in mine production in that they transport the valuable minerals (blasted ore) to the ore passes and hence out of the mining zone. Therefore, it is crucial in a mining operation that a haulage drift remains functional at all times.

4.2 Selection of parameters of stope and haulage drift

To build a characteristic model for the simulation of stability of haulage drift, parameters of the stope and haulage drift will be based on Canadian underground mines which are using sublevel stoping methods.

4.2.1 Stope geometry

Some reported sublevel stope geometries from Canadian mines are listed in Table 4-1, and terminology used in Table 4-1 for describing stope geometry is shown in Figure 4.6.

Table 4- 1 Examples of sublevel stope geometry in Canadian underground mines*

Mine, Company	Sublevel Stope Geometry				Shaft Depth (m)
	Height (m)	Length along strike (m)	Width (m)	Dip (°)	
Laronde, Agnico-Eagle	30	15	4-10	85	No.1: 1207 No.3: 2240
Doyon, Cambior	13-30	10	8	65	1000
Kidd, Falconbridge	40	25	15	75-90	1554
Lindsley, Falconbridge	20	20	4-10	55-85	1638
Trout Lake, Hudson Bay	30	25	8	55-60	1100
Copper Cliff South, Inco	60.96 (200')	18.29 (60')	15.24 (50')	75	1293
	15.24 (50')	30.48 (100')	6.1 (20')		
Creighton, Inco **	60.96 (200')	15.24 (50')	12.22 (40')	70-90	2560 (Sylvestre, 1999)
Holloway, Newmont	15-30	25-75	4-12		865

* **2005 Mining Sourcebook,** Canadian Mining Journal

** **2000 Mining Sourcebook,** Canadian Mining Journal

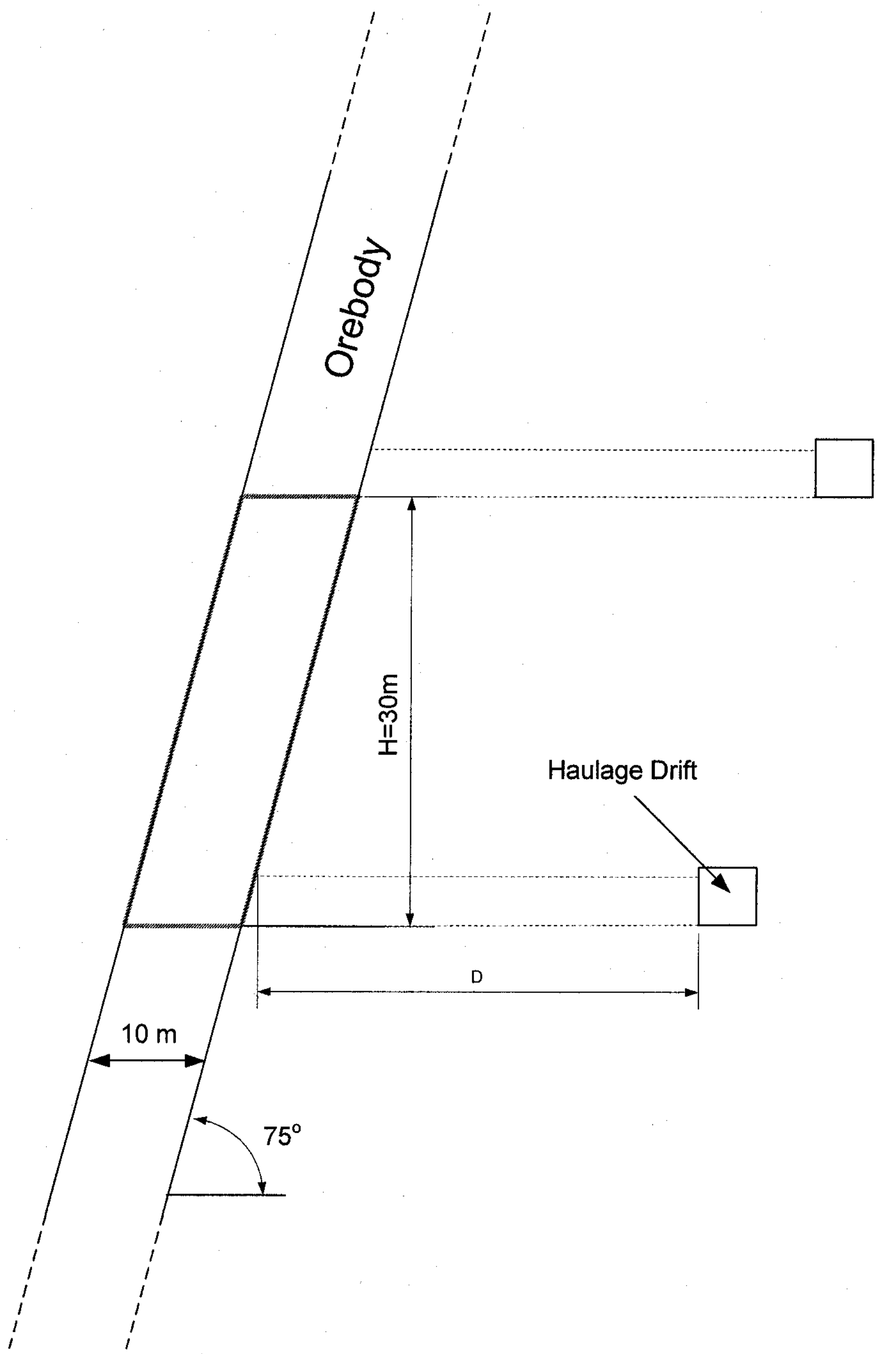

Figure 4. 6 Modelled sublevel stope geometry and terminology

Based on the information collected in Table 4-1, the base sublevel stope model parameters are chosen as follows:

Vertical stope height:	30 m
Horizontal width of orebody:	10 m
Dip angle of orebody:	75°

4.2.2 Geometry of haulage drift

Table 4-2 shows examples of haulage drift geometries reported in Canadian underground mine.

Table 4- 2 Examples of haulage drift geometries in Canadian underground mines*

Mine, Company	Haulage drift sizes (m × m)
Laronde, Agnico-Eagle	4.5 x 4.5
Doyon, Cambior	4.0 x 4.2
Kidd, Falconbridge	4.5 x 4.5
Lindsley, Falconbridge	4.6 x 4.6
Trout Lake, Hudson Bay	5.2 x 4.2
Copper Cliff South, Inco	4.9 x 4.9 (16' x 16')
Creighton, Inco	variable
Holloway, Newmont	4.0 x 3.7 & 5.0 x 3.7
* **2005 Mining Sourcebook,** Canadian Mining Journal	

Based on the information collected in Table 4-2, the modelled haulage drift geometry is chosen as: 4.50m × 4.50m rectangular shape.

As part of the parametric study, a rectangular drift with 3-centered arc roof will also be studied. In order to permit fair comparison the areas of cross sections (20.25 m^2) will be kept same.

The 3-centered arc roof drift (4.50m × 4.73m) is shown in Figure 4.7.

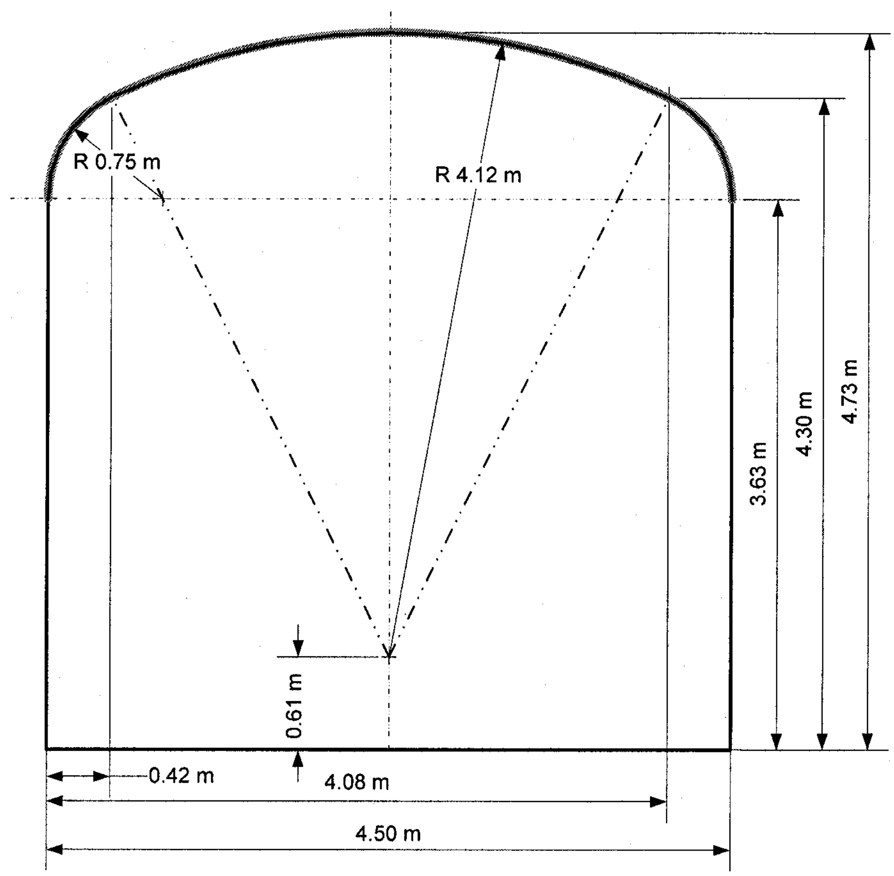

Figure 4. 7 Geometry of modelled haulage drift with 3-cantred arc roof

4.2.3 Distance between haulage drift and footwall of ore body

The distance, *D*, between haulage drift and the stope is defined in Figure 4.8. It depends on several factors, such as rock mass quality, in situ stress, mining depth below surface, loading equipment, ore body geometry, stope access geometry, and angle of repose of blasted ore. Given that Canadian underground mines in Canadian shields have moderate to strong rock mass quality, the length of mobile loading equipment between 3 m and 11 m (mucking machine 3-5 m, and Scooptram 6-12 m). Referring to Bousquet 2 Mine (Henning, 1998), the distance *D* for the base model is chosen as $D = 50\ m$.

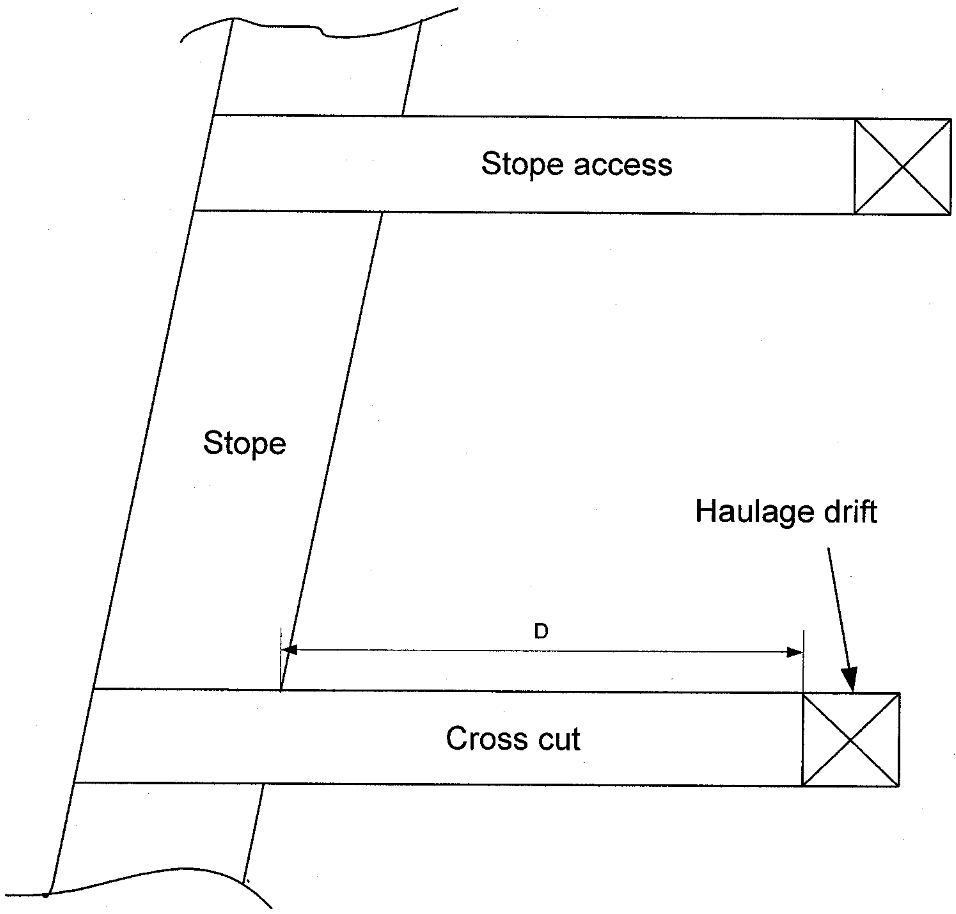

Figure 4. 8 Definition of distance, *D*, between the stope and haulage drift

4.2.4 Stope and haulage drift layout and mining sequence

Figure 4.9 shows the mining layout that will be adopted for the characteristic numerical model. As can be seen, there are three stopes between levels, hence two sublevels are required. The mining method is open stoping with delayed backfill. The numbers between brackets indicate the excavation and backfilling sequence in the numerical model, which will be referred to as "staging" in subsequent discussion of the numerical model.

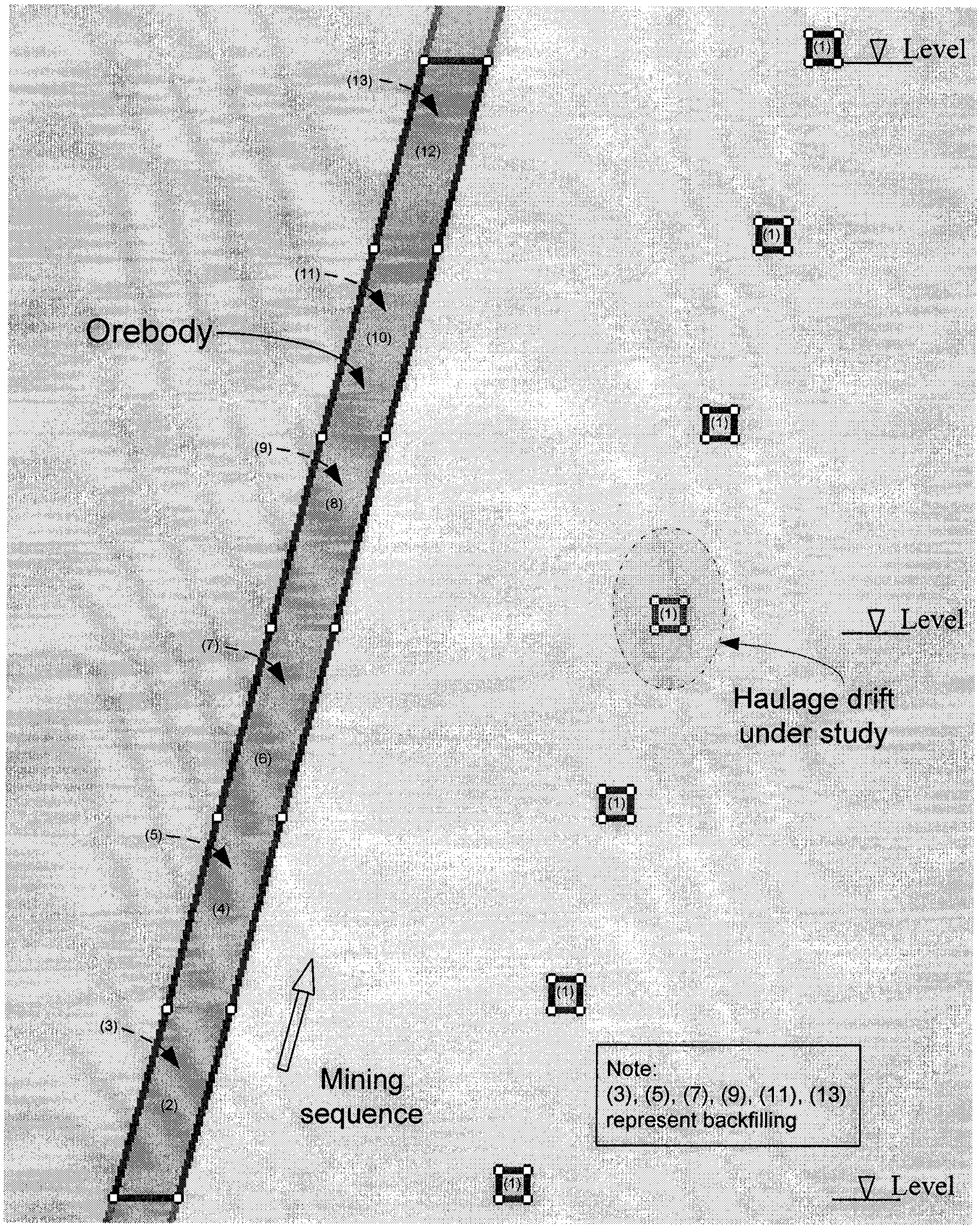

Figure 4. 9 Stope and haulage drift layout and mining-backfill sequences simulated

4.3 Selection of rock mass properties and initial stress conditions

4.3.1 In situ stress

In situ stresses are pre-mining natural stresses found in the rock mass, sometimes referred to as far field stresses. In situ stresses result from the weight of overlying rock materials (gravitational stress) and tectonic forces.

In situ stresses are usually reported as vertical stress (σ_v) and two horizontal stresses ($\sigma_{H\max}$) and ($\sigma_{H\min}$). They are also frequently described as three principal stresses ($\sigma_1, \sigma_2, \sigma_3$). According to Arjang (1991), there is a common feature in the Canadian Shield for near vertical ore bodies is that the maximum horizontal stress acts perpendicular to the strike of the ore body while the minimum horizontal stress is aligned on-strike. Brunswick Mine is one of the typical examples (Andrieux & Simser, 2001). The in situ stresses have following relationship in terms of different descriptions.

$$\begin{aligned} \sigma_1 &= \sigma_{H\max} \\ \sigma_2 &= \sigma_{H\min} \\ \sigma_3 &= \sigma_v \end{aligned} \tag{4.1}$$

The ratio of average horizontal stress σ_h to the vertical stress is normally expressed as:

$$k = \frac{\sigma_h}{\sigma_v} \tag{4.2}$$

In the Canadian Shield, the ratio k varies nonlinearly with the depth (Brown & Hoek, 1978; Herget, 1987). At shallow depth, k tends to be higher than at deep depth, as shown in Figure 4.10. The vertical component of in situ stresses varies linearly with depth H. That is:

$$\sigma_v = \gamma H \tag{4.3}$$

where the stress unit is MPa; the depth unit is m (meter); and γ is the unit weight of overlying rock mass (MN/m^3). In the Canadian Shield, the average rock mass density is in the range of 0.0255 MN/m^3 to 0.0275 MN/m^3 (2600 kg/m^3 to 2800 kg/m^3).

and (Herget, 1987)

$$k_{\max} = \frac{\sigma_{H\max}}{\sigma_v} = \frac{357}{H} + 1.46$$
$$k_{ave} = \frac{\sigma_{Have}}{\sigma_v} = \frac{267}{H} + 1.25 \tag{4.4}$$
$$k_{\min} = \frac{\sigma_{H\max}}{\sigma_v} = \frac{167}{H} + 1.10$$

Based on above information and documented stress data (Figure 4.11), Diederichs recommended that the horizontal components of in situ stresses can be calculated by (Diederichs, 1999):

$$\sigma_{H\max} = k_{\max}\sigma_v$$
$$\sigma_{H\min} = k_{\min}\sigma_v \tag{4.5}$$

and

$$k_{\max} = 1 + \frac{25}{\sqrt{H}}$$
$$k_{\min} = 1 + \frac{8}{\sqrt{H}} \tag{4.6}$$

The units in equations (4.5) and (4.6) are the same as equations (4.3) and (4.4).

In this study, three mining depths will be considered: 1500 m, 2000 m, and 2500 m. By using equations (4.3), (4.5) and (4.6), the calculated in situ stress components for the characteristic models are shown in Table 4-3.

4.3.2 Rock mass mechanical properties

In Canadian Shields, mineral deposits are typically associated with crystalline rock forming, e.g. basalt, andesite, rhyolite, granite. Such rock masses may have variable qualities from fair to very good. Bousquet 2 Mine is one of the typical examples. For the model parametric study, the rock mass parameters will be based on Bousquet 2 Mine's test results (Henning, 1998), as shown in Table 4-4.

Table 4- 3 Input data of in situ stress components for different modelling depths

Depth Category	Depth, H (m)	γ (MN/m^3)	k_{max}	k_{min}	σ_v (MPa)	$\sigma_{H\max}$ (MPa)	$\sigma_{H\min}$ (MPa)
H-1	1500	0.0255	1.65	1.21	38.25	63.11	46.28
H-2	2000	0.0255	1.56	1.18	51.00	79.56	60.18
H-3	2500	0.0255	1.50	1.16	63.75	95.63	73.95

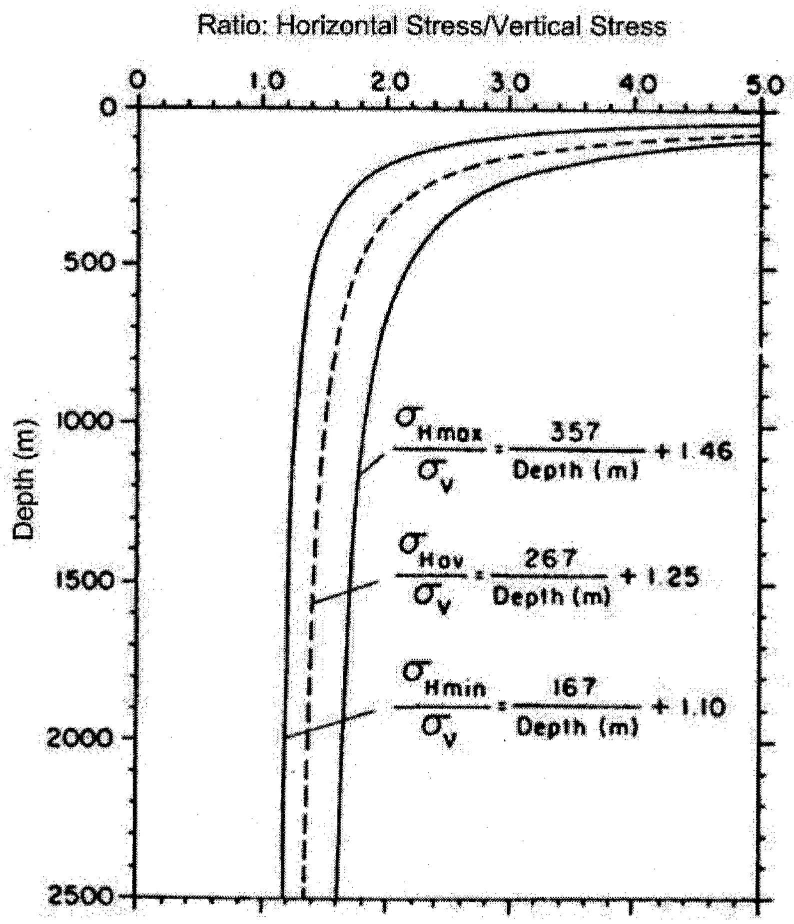

Figure 4. 10 Variations of k values with depths (Herget, 1987)

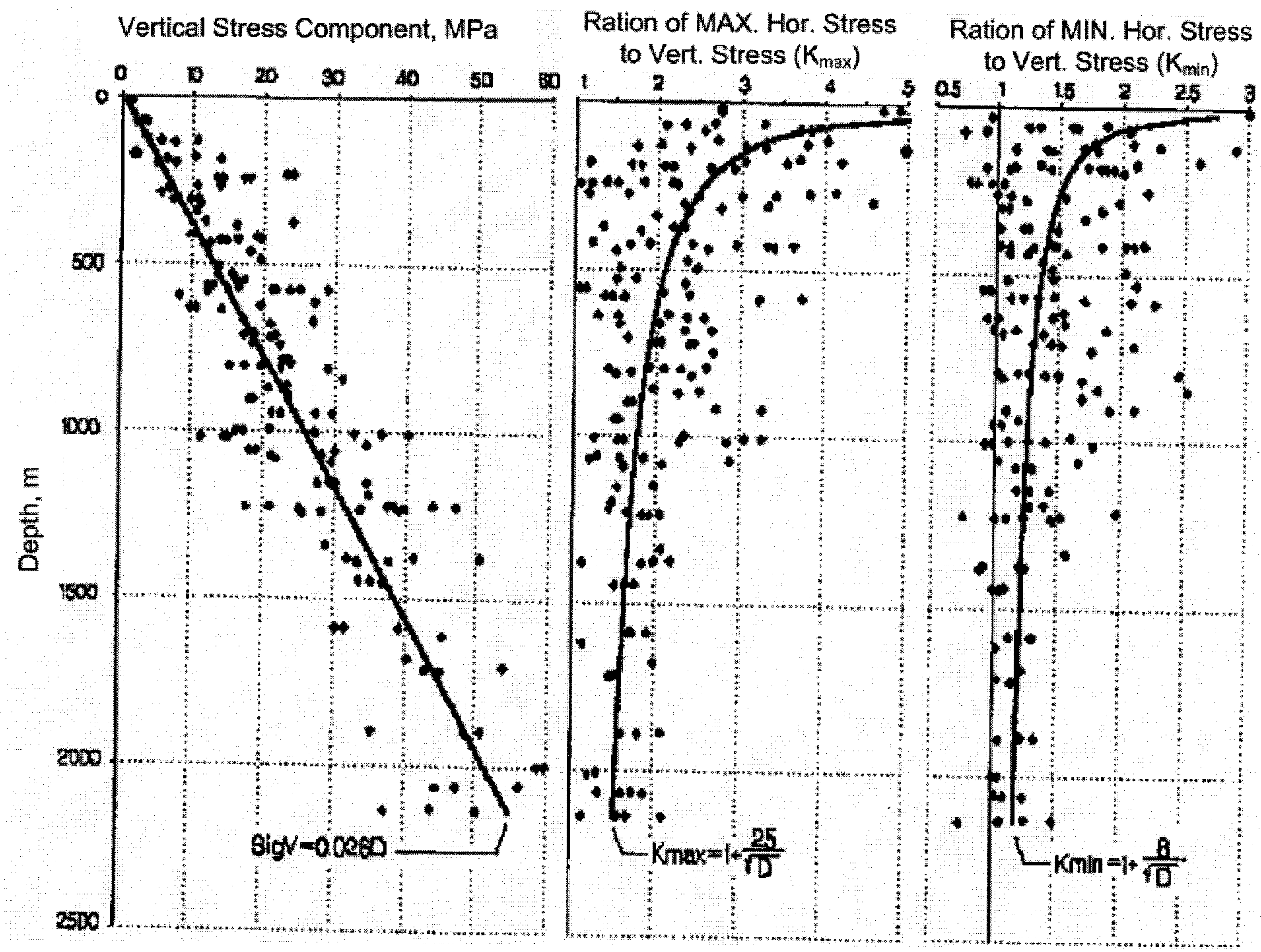

Figure 4. 11 In situ stress components reinterpreted by nonlinear functions (Diederichs, 1999)

Table 4- 4 Rock mass mechanical properties for the characteristic model

Rock Mass Parameter	Domain		
	Hanging-wall	Ore body	Footwall
Modulus of elasticity, E (GPa)	31	115	49
Cohesion, **c** (MPa)	2.6	11.5	4.3
Friction angle, ϕ, (^{o})	38	48	39
UCS, (MPa)	11	59	18
Poison's ratio, υ	0.21	0.10	0.15
Unit weight, γ (kN/m^3)*	25.51	25.51	25.51
Tensile strength (MPa)**	1.1	5.9	1.8
Dilation angle, ψ (^{o})	12-20*** $\frac{1}{4}\phi$****	12-20*** $\frac{1}{4}\phi$****	12-20*** $\frac{1}{4}\phi$****

* Canadian Shield average value

** Assuming 10% of UCS, based on Tesarik, Seymour, and Yanske (2003)

*** Vermeer (1998)

****Hoek and Brown (1997)

4.3.3 Backfill mechanical properties

It is common practice in Canadian underground mines that the primary stopes are backfilled using cemented backfill materials, e.g. tailings, sands, waste rock etc; the secondary stopes are usually backfilled without cement materials. For this study, it will be focused on primary stopes. After mining, the voids are backfilled with cemented rockfill. Table 4-5 shows the cemented backfill material properties (Archibald & Hassani, 1998).

Table 4-5 Model parameters for cemented rockfill (Archibald & Hassani, 1998)

Backfill Parameter	Material Value
Modulus of elasticity, E (GPa)	2.5
Cohesion, **c** (MPa)	0.1
Friction angle, ϕ, (°)	35
UCS, (MPa)	3.0
Poison's ratio, υ	0.35
Unit weight, γ (kN/m^3)	23.00
Dilation angle, ψ (°)*	0
* Traina (1983), and Hoek and Brown (1997)	

4.4 Selection of mesh quality

In finite element analysis, finite element mesh is generally desirable to avoid high aspect ratio of element. The presence of such elements can have adverse effects on the analysis results, lead to misleading and inaccurate results, even lead to non-convergence of the finite element solution in extreme cases. To guarantee appropriate accuracy of the results and not too finer mesh which will lead more computing time, for this parametric study the mesh quality will be defined.

A poor quality element is that with one or more of following conditions:

- Aspect ratio = (maximum side length) / (minimum side length) > 10;
- Minimum interior angle < 45°;
- Maximum interior angle > 135°.

The total poor quality elements will be controlled within 5%.

Chapter 5 Stability Analysis of Mine Haulage Drift

5.1 Introduction

Stability assessment is one of the most important issues in ground control. As analytical methods cannot provide adequate solutions, empirical methods have become widely used in Canadian underground mines. Empirical methods are based on past experiences and rock mass classification systems. They employ certain geomechanical characteristics of the rock mass to provide guidelines on stability performance and to determine the rock support requirements.

The most commonly used rock mass classification systems in Canadian mines are Rock Quality Designation (RQD) system proposed by Deere et al. (1967), Rock Mass Rating (RMR) system and its variations originally proposed by Bieniawski (1973), Tunnelling Index Quality (Q) System, proposed by Barton et al.(Barton, Lien, & Lunde, 1974) and Geological Strength Index (GSI) system, proposed by Hoek et al. (Hoek, Wood, & Shah, 1992; Hoek, 1994; Hoek, Kaiser, & Bawden, 1995; Hoek & Brown, 1997; Hoek, Carranza-Torres, & Corkum, 2002). The Stability Graph Method proposed by Potvin (1988) is based on the Q-system; it is widely used in Canadian mines for the assessment of stope stability.

Numerical modeling methods have become widely accepted in Canadian underground mines in recent years as a tool for the assessment of stability of underground mine openings and risk of ground failure. These methods combined with empirical methods provide an excellent approach for engineering design of mine openings.

5.2 Criteria for the evaluation of drift stability

5.2.1 Extent of yield zones

This criterion is widely used in numerical modeling when elastoplastic models are employed. The yield condition at a point is reached when the state of stress reaches the yield surface. Thus yielding may be considered as an important factor contributing to instability.

5.2.2 Displacement/Convergence criteria

Displacement convergence criteria are generally site specific; they depend not only on the rock mass characteristics but also on the intended usage of the underground opening as well as the design and code requirements. In the following, three displacement-based criteria are presented.

The first criterion is the wall convergence ratio (WCR), which is defined by the ratio of the total magnitude of the wall closure to the span of the drift (W^0) (see Figure 5.1). Thus,

$$WCR = \frac{W^0 - W^1}{W^0} \times 100\% \tag{5.1}$$

where W_1 is the span of drift after it has been deformed.

The roof sag ratio (RSR) is defined by the roof/back sag (ΔS) to the span of the drift (see Figure 5.2). Hence,

$$RSR = \frac{\Delta S}{W^0} \times 100\% \tag{5.2}$$

The third criterion is the floor heave ratio (FHR), which is defined by the ratio of floor heave (Δh) to the span of the drift (see Figure 5.2):

$$FHR = \frac{\Delta h}{W^0} \times 100\% \tag{5.3}$$

In the above equations, the superscripts, *0 and 1*, denote initial and deformed values, respectively.

5.2.3 Stress concentration criterion

This criterion uses the stress concentration factor (SCF), which is the ratio of the mining-induced major principal stress to the average undisturbed stress or pre-mining stress (σ^0) (Obert, Duvall, & Merril, 1960).

$$SCF = \sigma_1 / \sigma^0 \tag{5.4}$$

where σ_1 is the mining-induced major principal stress. The value of SCF is usually used to determine the location and extent of high stress zone created by an excavation. If the SCF is more or less uniform around the mine opening, such opening is considered more stable (Obert, Duvall, & Merril, 1960). When a nonlinear modelling capability is not available, SCF criterion is used in linear elastic analyses as an indicator of potential instability.

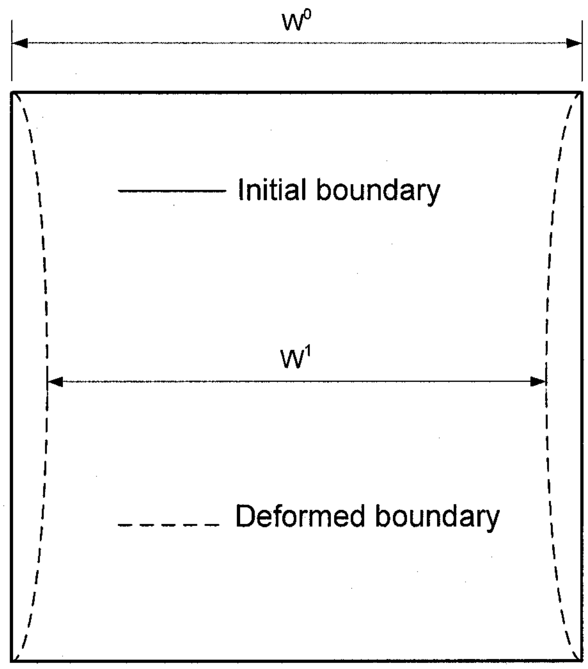

Figure 5. 1 Definition of wall convergence

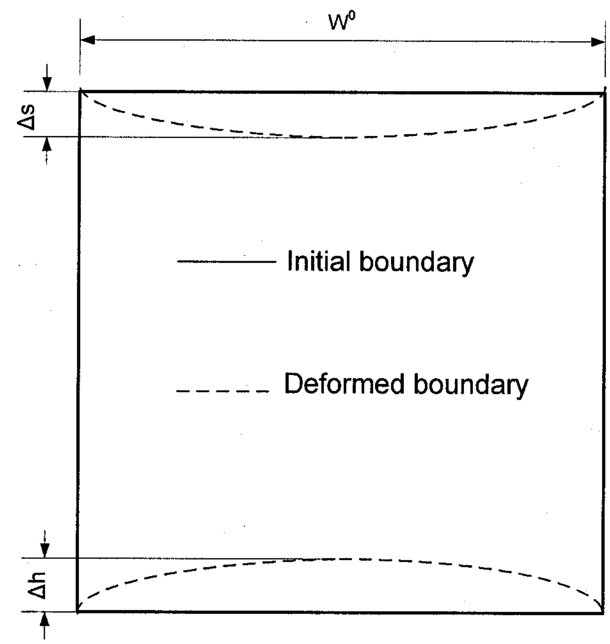

Figure 5. 2 Definition of roof sag and floor heave

5.3 Model parametric study

A series of 39 numerical simulations has been carried out to investigate the stability of the mine haulage drift. Table 5-1 summarizes the cases simulated for the model parametric study. The base model is selected with the following characteristics:

Three-centered arc roof with the dimensions shown in Figure 4.7;

Mining depth, H = 2000 m;

Distance between the stope and the haulage drift, D = 50 m;

Rock Mass Properties as given in Table 4-4 in Section 4.3;

In situ stresses as described in Table 4-3 in section 4.3 (k_{max} = 1.56 and k_{min} = 1.18).

The base model (model number 1 in Table 5.1) will be used as a basis for comparison of the drift model responses to varying different parameters.

Table 5- 1 Data for model parametric study

Model Number	Shape (W×H)	D (m)	H (m)	Ψ (°)	Model Type
1	3-centered Arc (4.50×4.73 m)	50	2000	12	Elastoplastic Model
2				20	
3				Φ/4	
4			1500	12	
5				20	
6				Φ/4	
7			2500	12	
8				20	
9				Φ/4	
10		40	2000	12	
11				20	
12				Φ/4	
13			1500	12	
14				20	
15				Φ/4	
16			2500	12	
17				20	
18				Φ/4	
19		60	2000	12	
20				20	
21				Φ/4	
22			1500	12	
23				20	
24				Φ/4	
25			2500	12	
26				20	
27				Φ/4	
28		50	2000	N/A	Elastic Model
29		40			
30		60			
31	Rectangular (4.50×4.50 m)	50	2000	12	Elastoplastic Model
32				20	
33				Φ/4	
34			1500	12	
35				20	
36				Φ/4	
37			2500	12	
38				20	
39				Φ/4	

5.4 Effect of mining sequences

In the following text, discussions are presented to demonstrate the effect of mining sequences on the drift stability. In the numerical modelling process, modelling "stages" is used to simulate the mining and filling sequences. Table 5-2 presents the definition of the 13 model stages that were used to simulate the mining and filling sequences of six stopes with three below and three above the drift under study, as illustrated in Figure 5.3.

5.4.1 Extent of yielding

Model 1 representing a 3-centred arc drift (Table 5.1) is used to examine the effect of mining extraction on the development of yield zone around the haulage drift at a mining depth of 2000 m and a distance of 50 m. The results are shown in Figure 5.4 in terms of the extent of yield zones as mining activity progresses upwards. As can be seen from Figure 5.4, the effect of mining and filling the lower stopes is insignificant (stages 2 to 6) with the yield zone extending only to a distance of 2.6 m (stage 6) in the drift sidewall on the far side of the orebody. As mining of the same-level stope proceeds, the yield zone extends significantly in the opposite drift sidewall to a distance of 3.5 m on the near side of the orebody (stage 8). The analysis further shows that the yield zone pattern is not symmetric. The yield zone continues to grow in the back and floor, however, to a lesser extent, with the extraction of the upper stopes (stages 10 and 12). In the end, the yield zone spreads around the drift in the following manner:

- Sidewalls: from 2.0 m (stage 1) to 3.5 m (stage 12) on the orebody side and from 1.7 m (stage 1) to 2.6 m (stage 12) on the far side;
- Floor: from 2.2 m (stage 1) to 4.1 m (stage 12);
- Back: from 1.8 m (stage 1) to 2.7 m (stage 12).

Furthermore, the analysis shows that backfilling has practically no significant effect on the reduction of yield zones. This is evident from the comparison of yield zone patterns of two consecutive stages representing mining and filling such as 8 and 9 shown in Figure 5.4.

Analyses of Model 2 to Model 27 (all models are 3-centred arc drifts, detailed parameters see Table 5.1) show the similar yield patterns to model 1 as the mining activity progresses upwards.

5.4.2 Stress concentration and redistribution

Model 1 as described in preceding section is used to investigate the stress concentration and redistribution patterns around the haulage drift at different mining steps. The results (stages 1, 2, 4, 6, 8, 9, 10, and 12) are shown in Figure 5.5 in terms of major principal stress, and Figure 5.6 in terms of stress concentration factor (SCF) contour, also called isotropic major principal stress flow line.

It can be seen from Figure 5.5 and Figure 5.6 that at a certain distance in the back and under the floor, there exist high stress-concentration spots (SCF > 1), but the magnitude is getting smaller (σ_{1max} = 143 MPa at stage 1, σ_{1max} = 110 MPa at stage 8, and σ_{1max} = 66 MPa at stage 12) with mining activity progression. The results also show that the stress-concentration spots are relatively clockwise rotating with the up dip mining activity.

The further analysis also shows that the long-axis of isotropic major principal stress flow lines of redistributed stresses is also clockwise rotating, and the magnitude of clockwise rotation angle is from 0° (horizontal) at stage 1 to approximate 50° at stage 8, and up to 135° at stages 12. When this result is compared with that of model 10 having D = 40 m, it is found that the principal stress rotation is even more pronounced than in Model 1. Likewise, Model 19 having D = 60 m shows smaller angles of principal stress rotation. Table 5-3 summaries those observations. Similar observations can be made by comparing Model 4, 13, and 22 having a mining depth of 1500 m; and Model 7, 16, and 25 at mining depth of 2500 m with smaller distance (Model 10 to 18, see table 5.1) rotating a larger angle and longer distance rotating (Model 19 to 27, see table 5.1) a smaller angle.

Furthermore, it can be also noticed that the stress concentration is more uniform in the back than in the floor, especially the two corners of the floor. This implies that rounded boundaries can reduce stress concentration.

Table 5- 2 Definition of numerical modelling stages

Model Stage	Definition
1	Opening of the haulage drifts
2	Ore extraction in the first (lowest level) stope
3	Backfill in the first stope
4	Ore extraction in the second stope
5	Backfill in the second stope
6	Ore extraction in the third stope
7	Backfill in the third stope
8	Ore extraction in the fourth (at the same level with the haulage drift) stope
9	Backfill in the fourth stope
10	Ore extraction in the fifth stope
11	Backfill in the fifth stope
12	Ore extraction in the sixth (the most upper level) stope
13	Backfill in the sixth stope

Table 5- 3 Effect of distance, D, on principal stress rotation from horizontal

Model	D (m)	Rotation Angle (°)		
		Stage 1	Stage 8	Stage 12
10	40	0	55	150
1	50	0	50	135
19	60	0	45	120

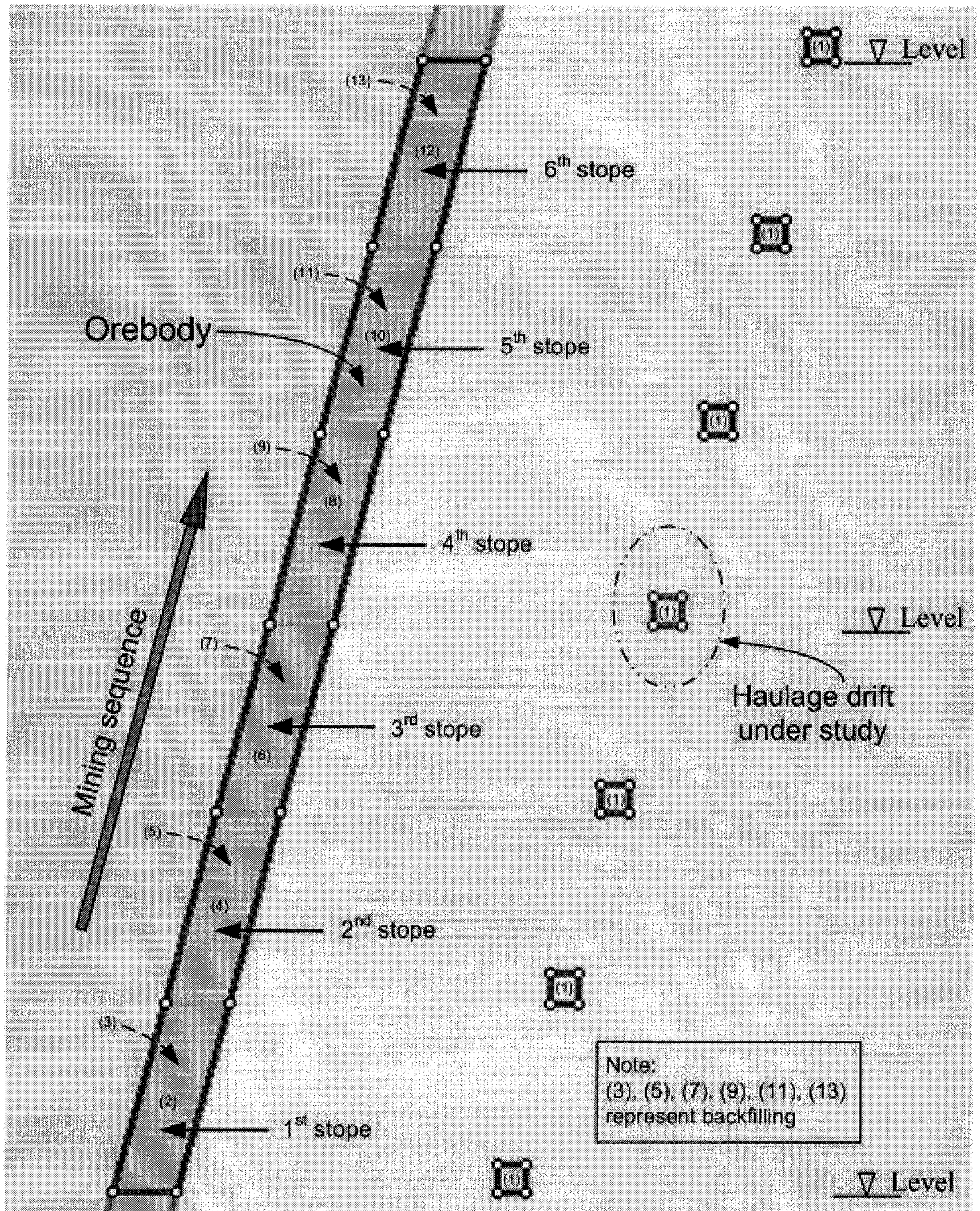

Figure 5. 3 Sequence of modelled stopes and drifts

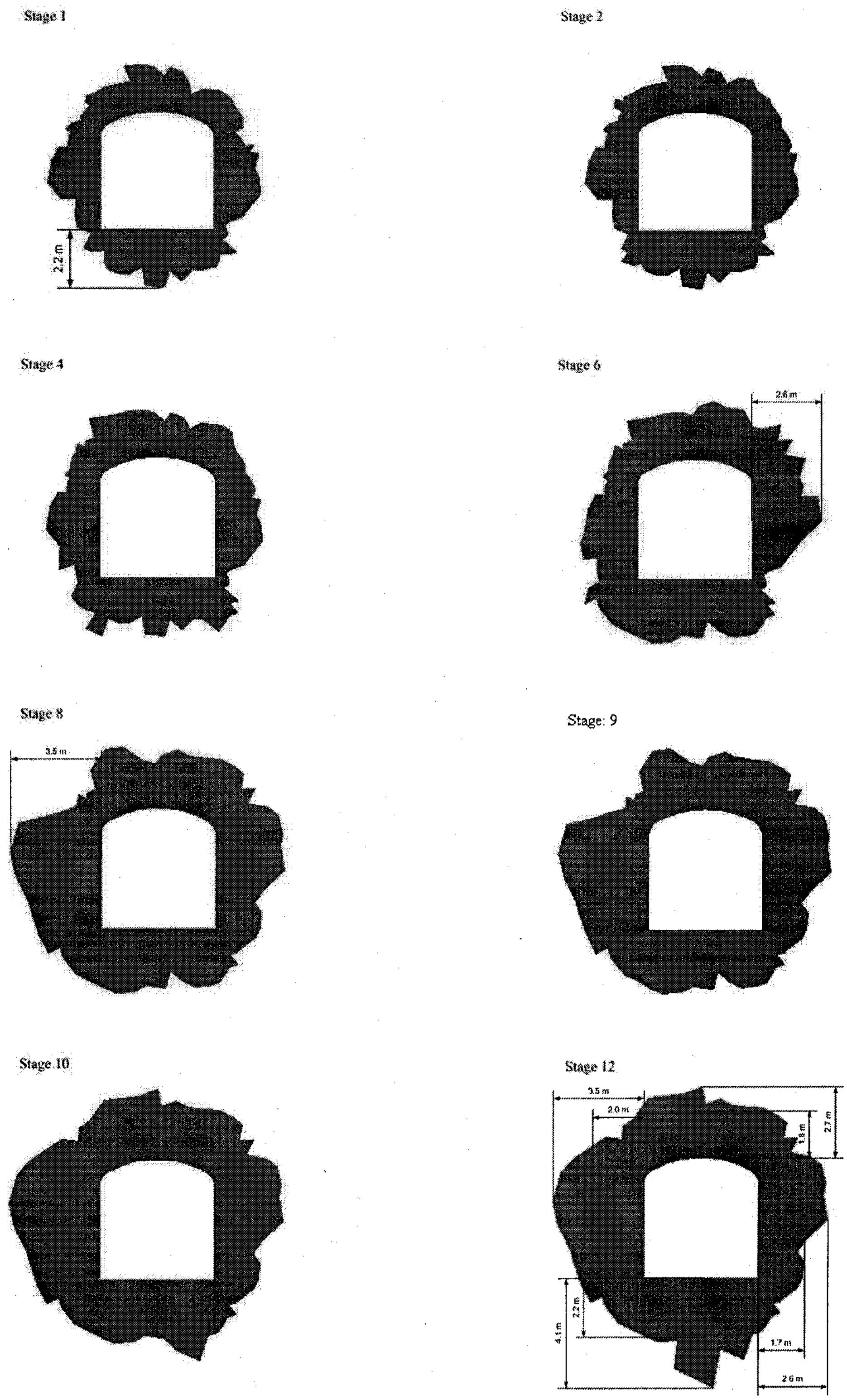

Figure 5. 4 Progression of yield zones with modelling stages—Model 1

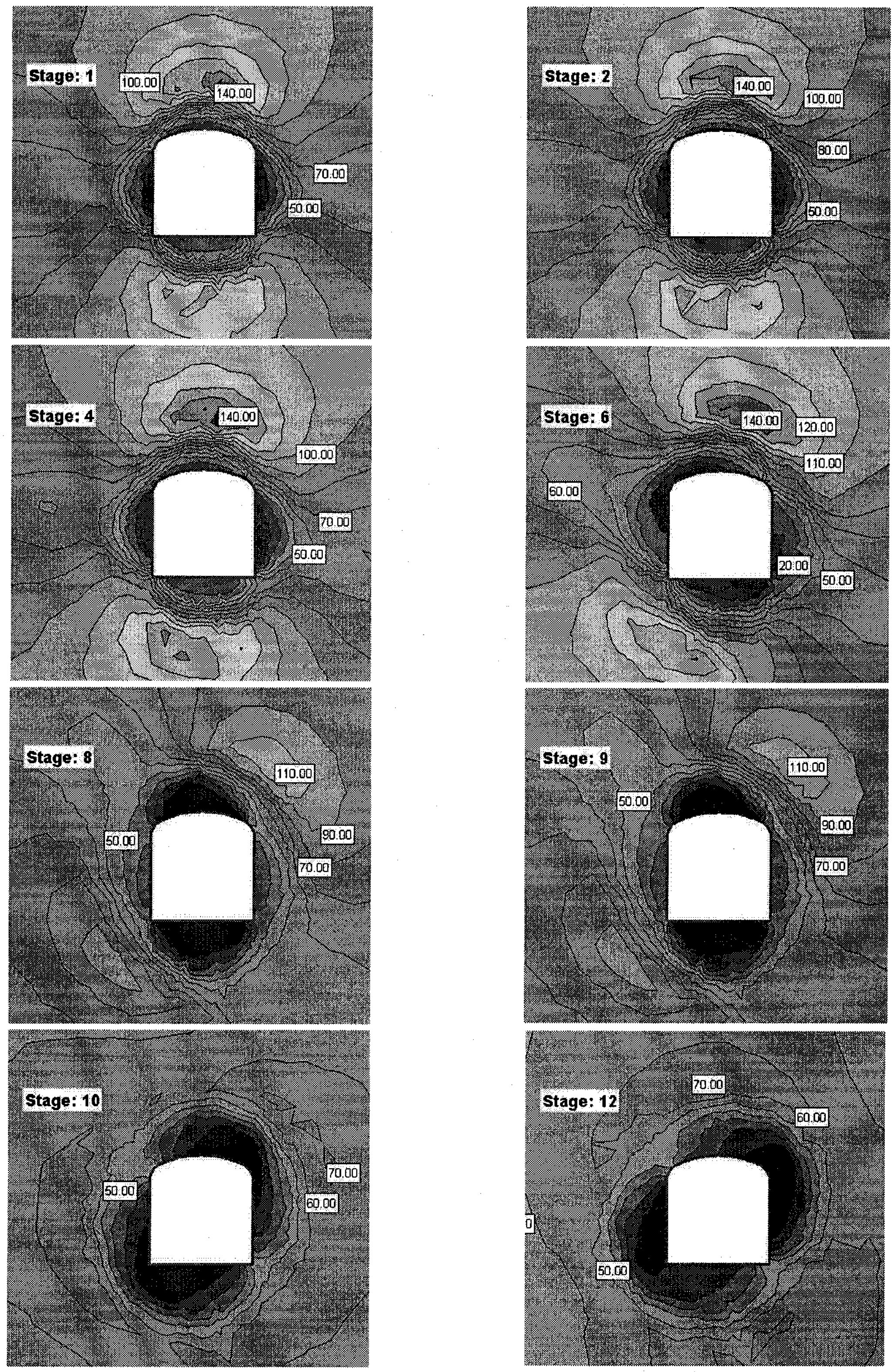

Figure 5. 5 Major principal stress distribution at different stages—Model 1

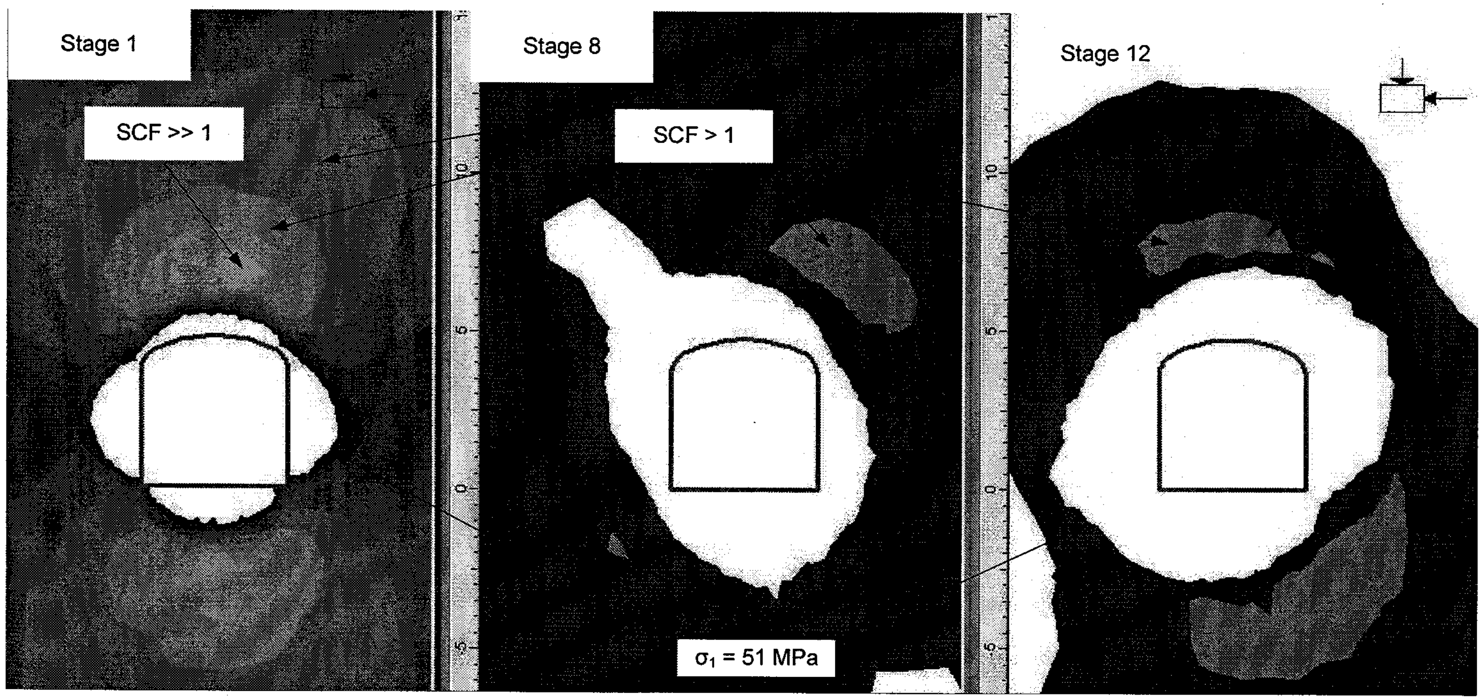

Figure 5. 6 SCF contours at different stages—Model 1

5.4.3 Wall convergence

Model 1 is used to examine wall convergence of the haulage drift in terms of sidewall relative displacements and wall convergence ratio. As expected, the wall convergence is not evenly distributed along the sidewalls with maximum convergence occurring near the middle of the sidewall at each stage. The wall convergence slightly decreases from 25 mm (stage 1) to 20 mm (stage 8), and then increases to 30 mm at stage 12. The maximum convergence occurs at the last stope extraction (stage 12) with WCR = 0.67%. It should be noted that the maximum deformations of the sidewall boundaries are near the mid-height of the sidewalls. Stope extraction results shifting of the haulage drift laterally towards the stope side. For the case of Model 1, the haulage drift shifts about 6 cm at the same level of stope extraction (stage 8) and 11 cm at the last stope extraction (stage 12).

Further analyses show that the sidewall horizontal displacement patterns are similar to Model 1 for other 3-centred arc drift models, but with the distance decrease, the values of displacement increase. Figure 5.7 shows the results of D = 50 m (Model 1), D = 40 m (Model 10), and D = 60 m (Model 19) at stage 12 with H = 2000 m. In the figures for each model, the upper displacement values are measured at the height of 3 m, and the lower displacement values are measured at the height of 2 m of the sidewall boundaries. It can be seen, the drift shifts about 12.5 cm when D = 40 m, and 10 cm when D = 60 m compared with 11 cm when D = 50 m.

5.4.4 Roof sag

Model 1 is used to examine the roof sag in terms of roof vertical displacement and roof sag ratio. Figure 5.8 demonstrates the roof sag profile at stages 1, 6, and 12, in which negative displacement denotes sag. It is shown that the roof sags are not evenly distributed with maximum value occurring on the right side of the roof centerline at each stage. It can be seen that at stage 6 the roof sag reaches to the maximum value, about 18 mm (RSR = 0.4%); then decreases to some 2 mm at stage 12, showing skewed distribution with larger sag near the far side of the orebody.

Further studies have shown that stage 6 (mining at the one level lower of the haulage drift) is a significant stage in terms of producing maximum sag.

The effect of mining depth on maximum roof sag can be examined by comparing the result of Model 1 with those of Models 4 and 7 having mining depths of 1500 m and 2500 m respectively. The effect of distance *D* is examined through the comparison of model results having D = 40 m and 60 m. These are Models 10 and 19. Likewise, Models 4, 13, and 22, as well as Models 7, 16, and 25 are compared; see Table 5-4.

Table 5- 4 Effect of D and H on roof sag

Model	D (m)	H (m)	Max roof sag (mm)	RSR (%)
1	50	2000	18	0.400
4		1500	11	0.244
7		2500	25	0.556
10	40	2000	17	0.378
13		1500	10	0.222
16		2500	25	0.556
19	60	2000	17	0.378
22		1500	11	0.244
25		2500	24	0.533
1	50	2000	18	0.400
10	40		17	0.378
19	60		17	0.378
4	50	1500	11	0.244
13	40		10	0.222
22	60		11	0.244
7	50	2500	25	0.556
16	40		25	0.556
25	60		24	0.533

5.4.5 Floor heave

Model 1 is used to investigate the floor heave in terms of floor vertical displacement and floor heave ratio FHR as defined in equation 5.3. Figure 5.9 exhibits the floor heave profile at stages 1, 8 and 12. It can be observed that the floor heave presents monotonically increase showing skewed distributions, with bigger heave near the stope side. The maximum value at stage 8 is about 30 mm (FHR = 0.67%), and at stage 12 it reaches to about 45 mm (FHR = 1%).

Further studies (Model 2 to 27, see Table 5-1) have shown that floor heave patterns are similar to Model 1.

5.4.6 Summary of effect of mining sequence

- Mining in the same level of the haulage drift (stage 8) has the most significant influence to the development of yield zone around the haulage drift; stages 10 and 12 have secondly significant influence to the yield zone extending.
- Stope extraction (stages 2, 4, 6, 8, 10, and 12) affects the stress redistribution. There exist stress concentration zones in the back and under the floor.
- Extraction stages influence the wall convergence and shift the haulage drift towards the stopes with the mining activity progresses upwards.
- Roof sag has developing-receding phenomenon before and after stage 8.
- Floor heave constantly increase with skewed phenomenon.
- Mining at the same level of the haulage drift (stage 8) is a critical stage to the stability of haulage drift.

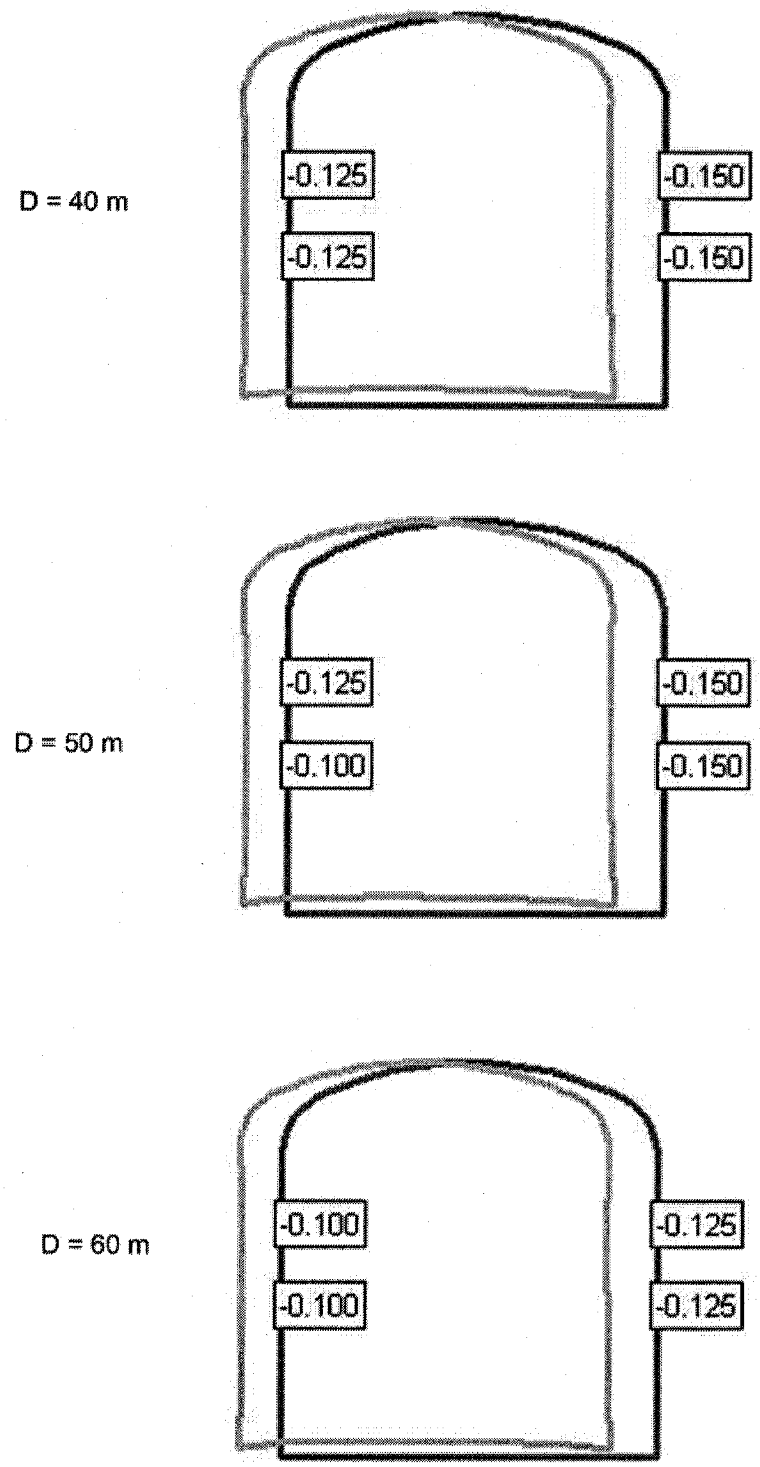

Figure 5. 7 Effect of distance D to horizontal displacement of the drift
Model 10, Model 1, and Model 19 from top to bottom

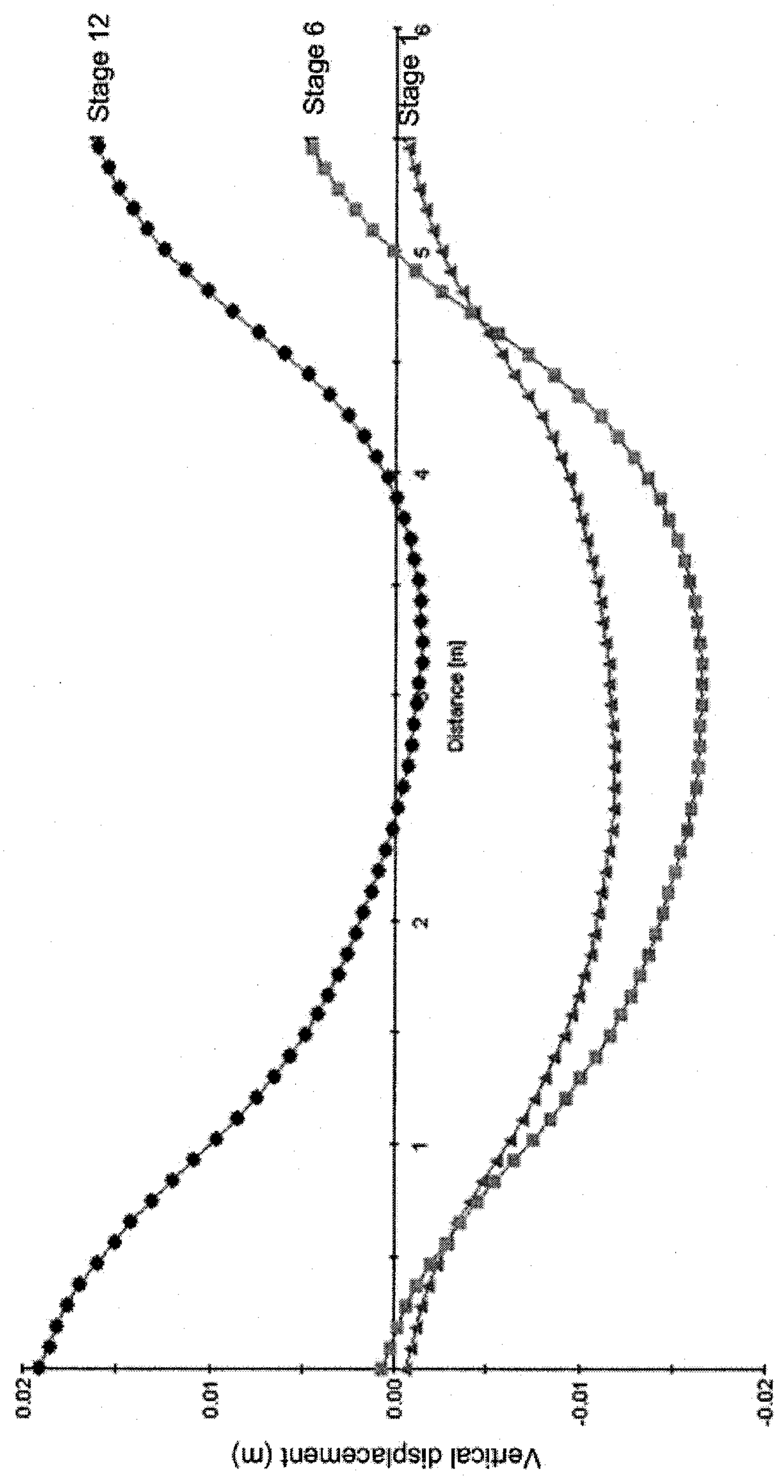

Figure 5. 8 Roof sag profile at different stages

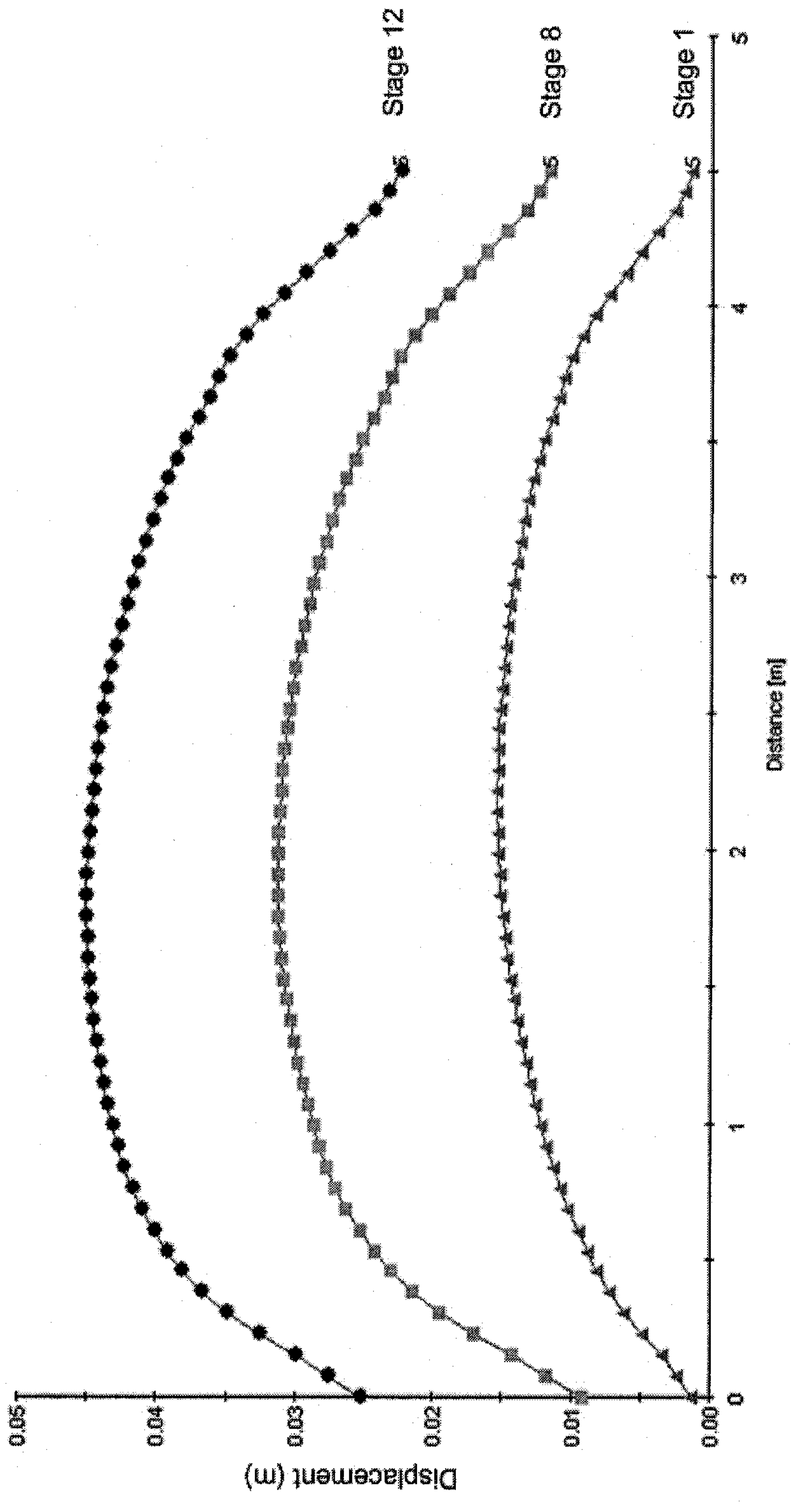

Figure 5. 9 Floor heave profile at different stages

5.5 Effect of distance

Models 1, 10 and 19 (see Table 5.1) representing D=50 m, 40 m and 60 m, respectively, are used to examine the influence of distance between haulage drift and stope on the stability of the haulage drift at a mining depth of 2000 m. All three drift models are 3-centred arc with dimensions of 4.5 m × 4.73 m. As mining at the same level of the haulage drift (stage 8), the results are shown in Figure 5.10 and Figure 5.11 in terms of stress distribution or concentration and the extent of yield zones, respectively.

It can be seen from Figure 5.10, the isotropic major principal stress flow lines (for example when SCF = 1, σ_1 = 51 MPa) extend outwards and the surrounded areas increase as the distance decreases. The analysis further shows that as the distance decreases, the isotropic major principal stress flow line pattern is not evenly distributed, with towards the stope direction extending faster than other directions, which somewhat implies that the major principle stress relieve more on the stope side than other side.

Figure 5.11 illustrates the results of yield zone comparisons vs. distance *D* for the same model group as in Figure 5.10 (stage 8). As can be seen from Figure 5.11, the effect of distance *D* is significant with the yield zone extending to a distance of 4.1 m from 3.5 m when the distance decreases to 40 m from 50 m; and the yield zone curtailing to a distance of 2.4 m from 3.5 m when the distance increases to 60 m from 50 m.

5.6 Effect of mining depth

Model 1, 4, and 7 representing 3-centred arc drifts (Table 5.1) are used to investigate the effect of mining depth on the development of yield zone and stress redistribution or concentration around the haulage drift at distance of D = 50 m and mining depths of H = 2000 m, 1500 m, and 2500 m. In this discussion the effect of mining depth reflects the effect of in situ stresses, representing three main factors: the depth of overburden, the average specific gravity, and the ratio (k) of horizontal stress to vertical stress.

Figure 5.12 shows the comparison results of the stress distribution/concentration vs. mining depth *H* at stage 8 for Model 4 (H = 1500 m), Model 1 (H = 2000 m), and Model 7 (H = 2500 m) (from left to right). Where SCF = 1 represent the isotropic major principal stress flow lines for Model 4 (σ_1 = 38.25 MPa), Model 1 (σ_1 = 51 MPa), and Model 7 (σ_1 = 63.75 MPa). It can be noticed that the isotropic SCF surrounded zones have enlarged with the increase of mining depth which implies that the major principle stress relieves bigger levels, but the stress distribution patterns has no significant change.

Figure 5.13 perceives comparison of yield zone vs. mining depth for the same model group as in Figure 5.12. It is found that, on the one hand, the yield zone enlarges as the mining depth increases from 1500 m to 2000 m, with the yield depths extending from 2.5 m to 3.5 m correspondingly; on the other hand, the yield depth has no considerable change as the mining depth increases from 2000 m to 2500 m. For all three models the maximum yield depths are located near the stope side sidewalls about 3 m high from the floor of the haulage drift.

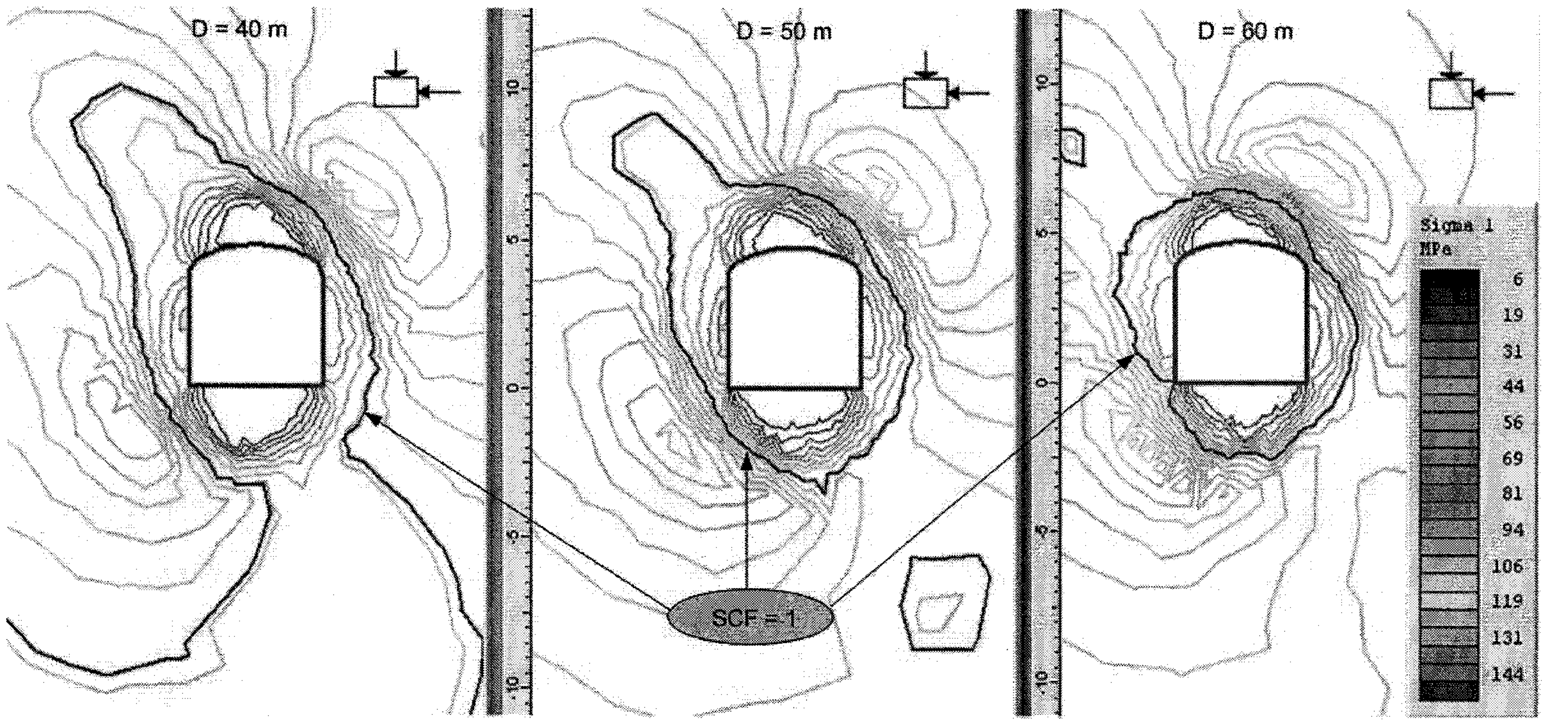

Model 10 Model 1 Model 19

Figure 5. 10 SCF contours at stage 8 for different D values

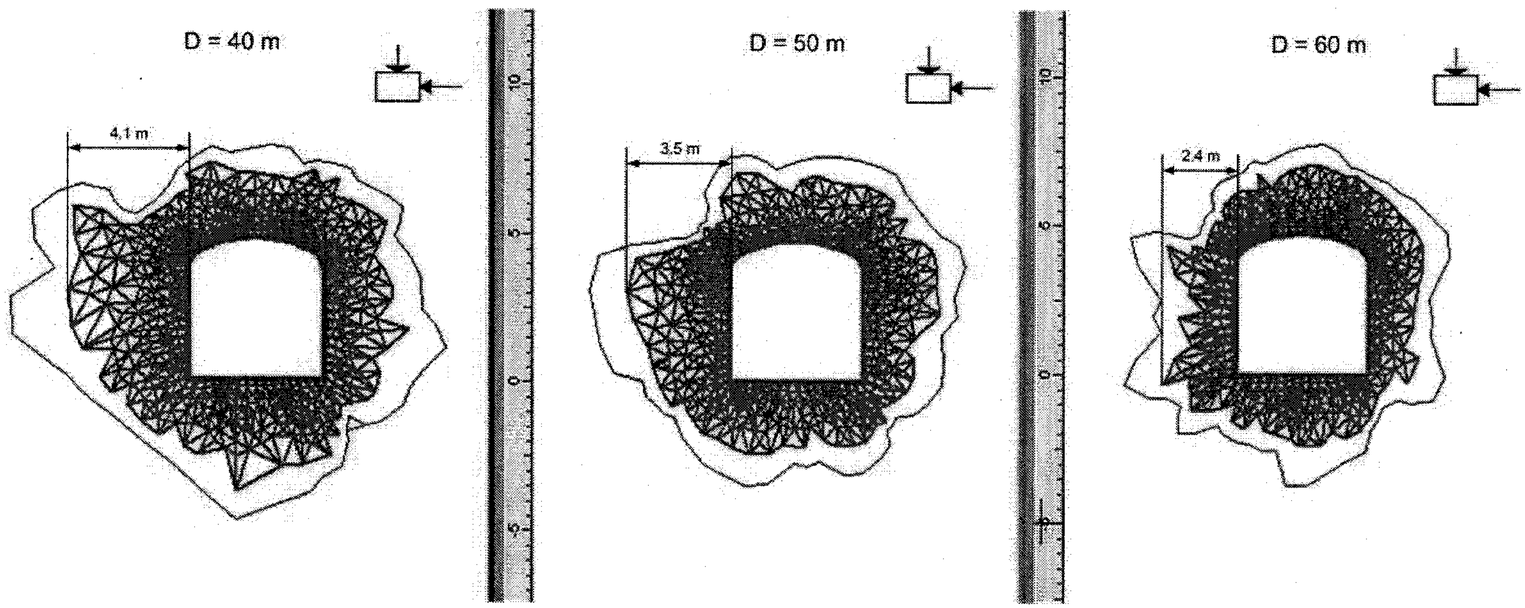

Model 10 Model 1 Model 19

Figure 5. 11 Extent of yield zones at stage 8 for different D values

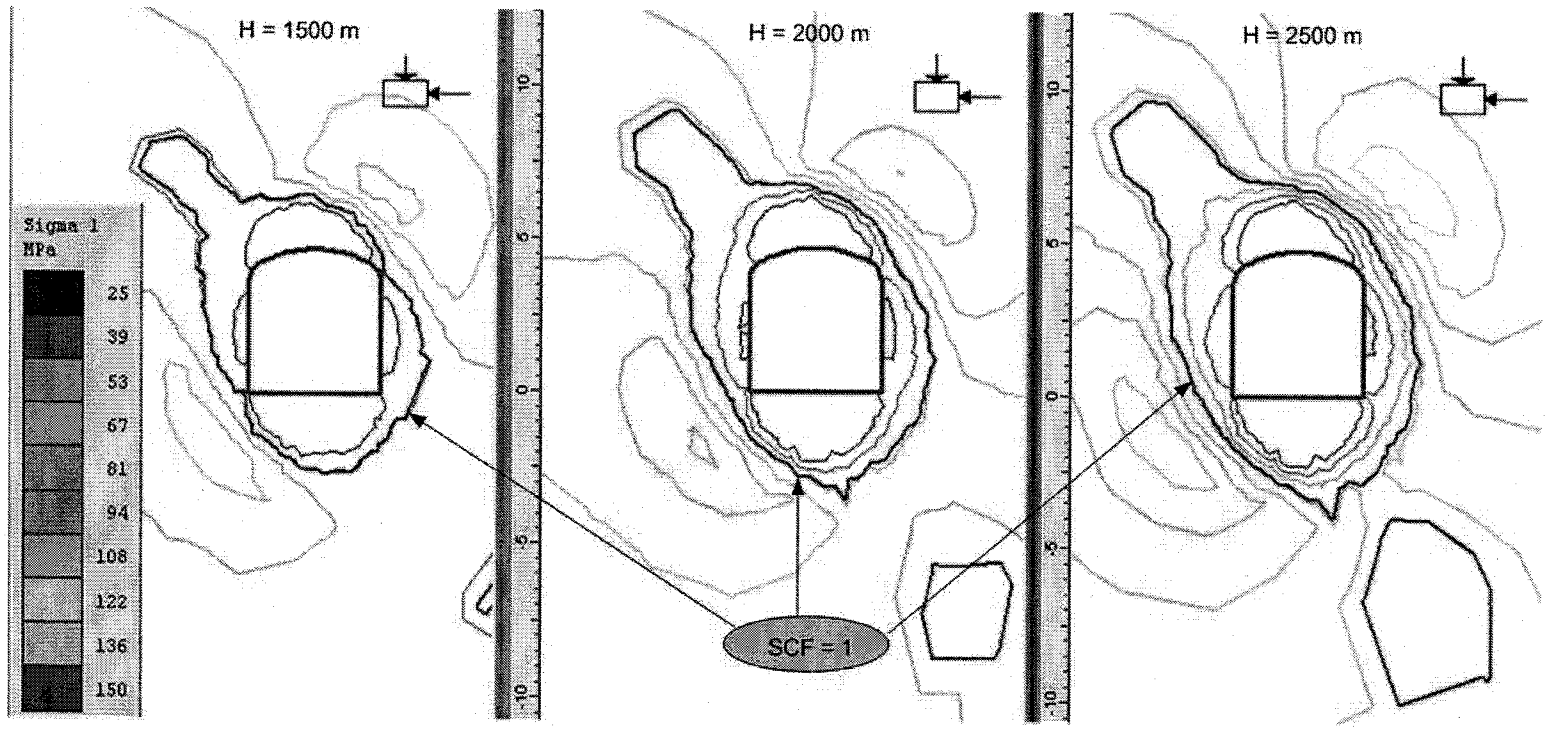

Model 4 Model 1 Model 7

Figure 5. 12 SCF contours at stage 8 for different H values

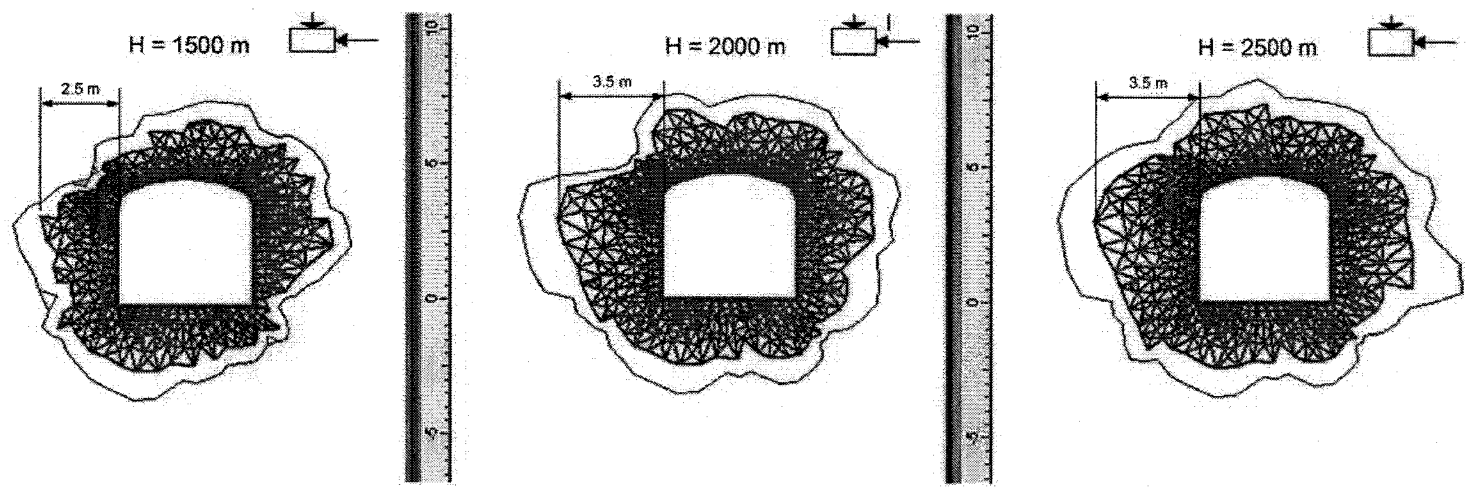

Model 4 Model 1 Model 7

Figure 5. 13 Extent of yield zones at stage 8 for different H values

5.7 Sensitivity of model results to the dilation angle

Dilation angle is one of the parameters that are not easily obtained for elastoplastic simulation of rock materials. To verify the influence of dilation angle to the response of stability of underground openings, this section will give detailed discussion of the sensitivity of dilation angle to the stability of haulage drift in terms of extent of yield zone, stress distribution pattern, and horizontal displacement inside the rock mass.

Models 1 to 3, 10 to 12, and 19 to 21 representing 3-centred arc drifts with H = 2000 m (Table 5.1) are used to examine the sensitivity of dilation angle on the development of yield zone at the final extraction stage (stage 12). Model 1, 2, and 3 are also used to investigate the sensitivity of dilation angle on major principal stress distribution, and horizontal displacement in the sidewall (stope side) starting from 3 m high sidewall boundary to 10 m deep when D = 50 m and H = 2000 m, as shown in Figure 5.14. Figures 5.15, 5.16 and 5.17 demonstrate the results of dilation angles of 0.25Φ (Model 3) (hanging-wall Φ = 38°, footwall Φ = 39°, orebody Φ = 48°), 12° (Model 1), and 20° (Model 2) in terms of yield zones, major principal stress distributions and horizontal displacement distributions.

It can be observed from Figure 5.15 that the final yield zone decreases with the increase of the dilation angle. It is obvious that the yield zones of Model 2, Model 11, and Model 20 (ψ = 20°) are smaller than that of. Model 1, Model 10, and Model 19 (ψ = 12°). On the other hand, the yield zones of Model 3, Model 12, and Model 21 ($\psi = 1/4\Phi \leq 12°$ and close to 12°) are slightly larger than that of Model 1, Model 10, and Model 19.

It can be seen from Figures 5.16 and Figure 5.17 that the dilation angle has insignificant effect on the SCF contour lines and the displacement distribution at all stages.

Further observations on different model groups representing 3-centred arc drifts, such as Models 4, 5, 6, 7, 8, and 9 have shown the similar results. Therefore, it can be concluded that the dilation angle affects only the final yield zones, with dilation angle increasing the final yield zones decrease. It also can be derived that using associated flow rule for hard rock mass would be underestimate the final yield zone in that dilation angle reaches to its maximum value with $\psi = \Phi$.

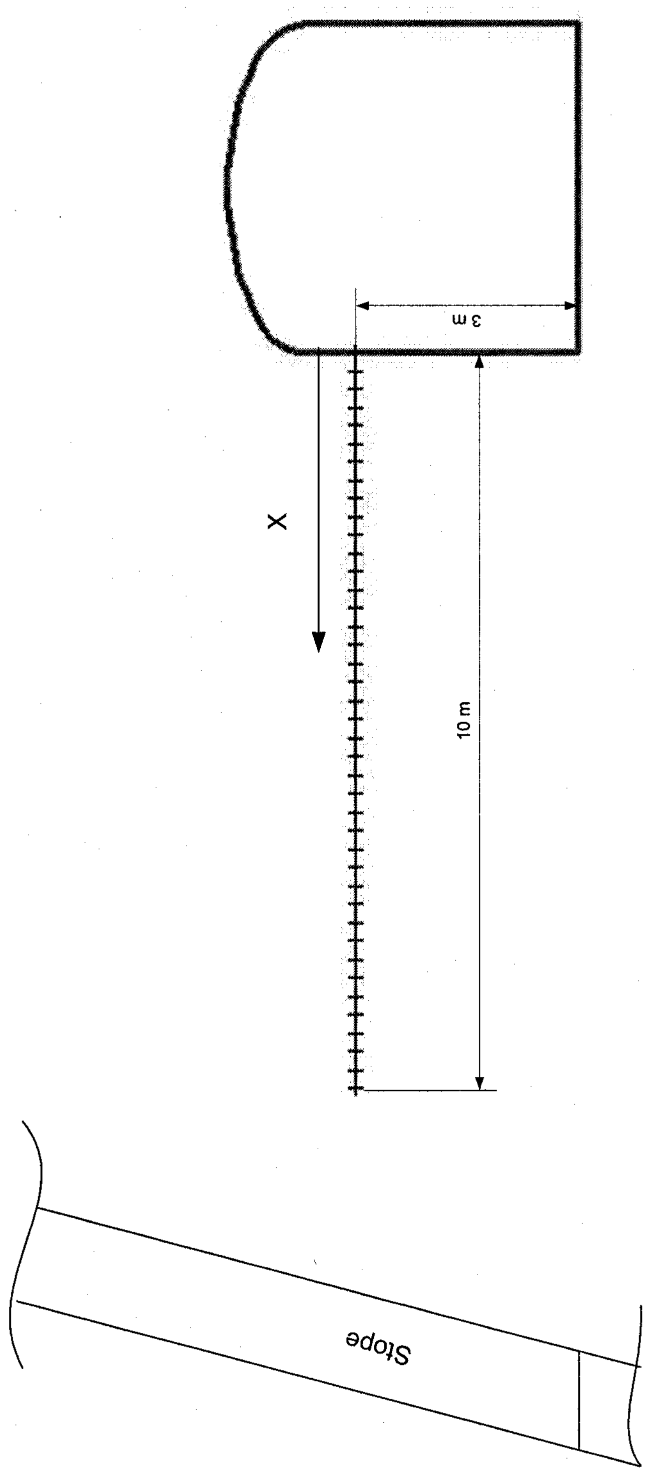

Figure 5. 14 Layout for checking sensitivity of dilation angle to model results

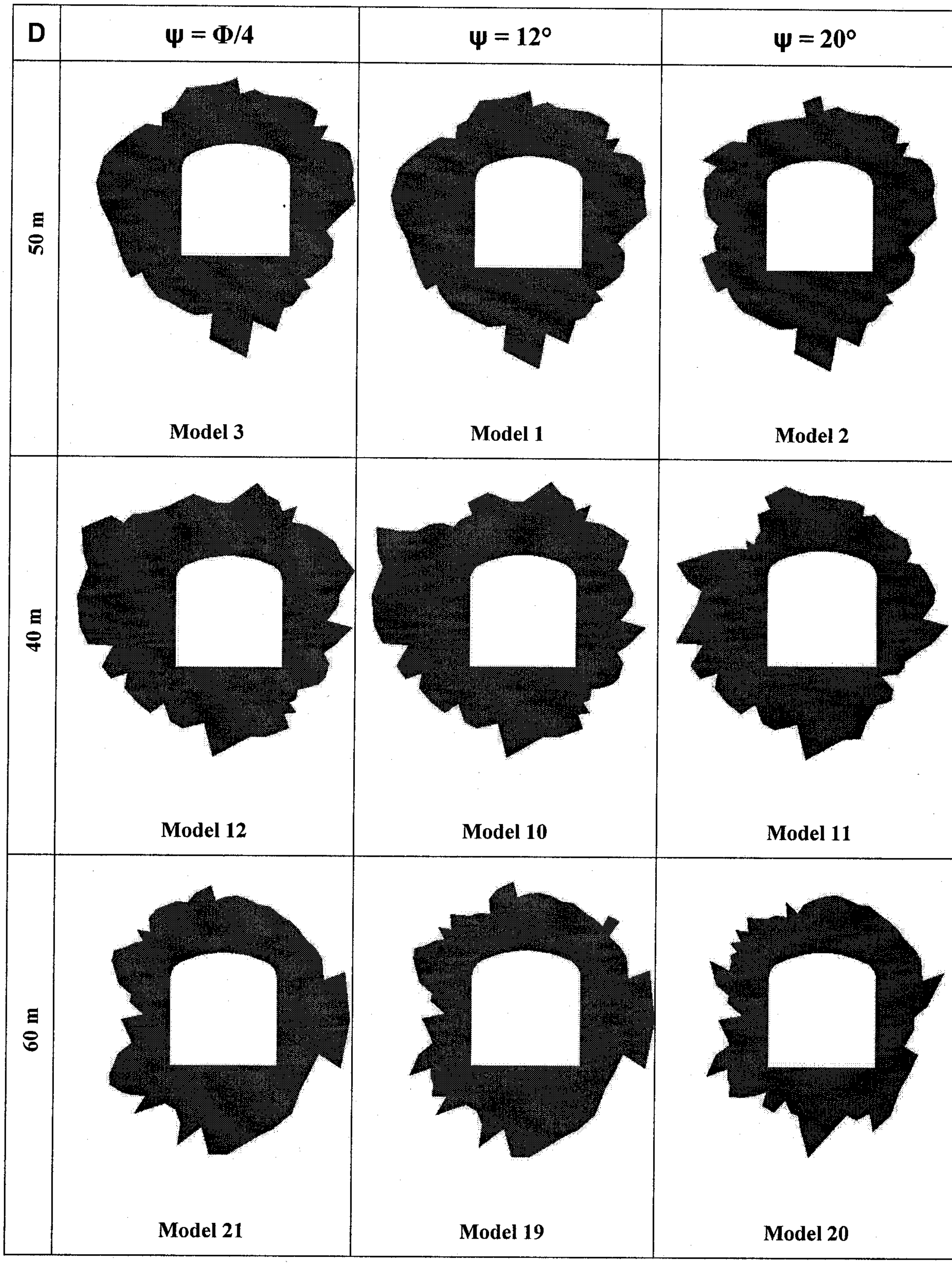

Figure 5. 15 Effect of dilation angle on yield ones

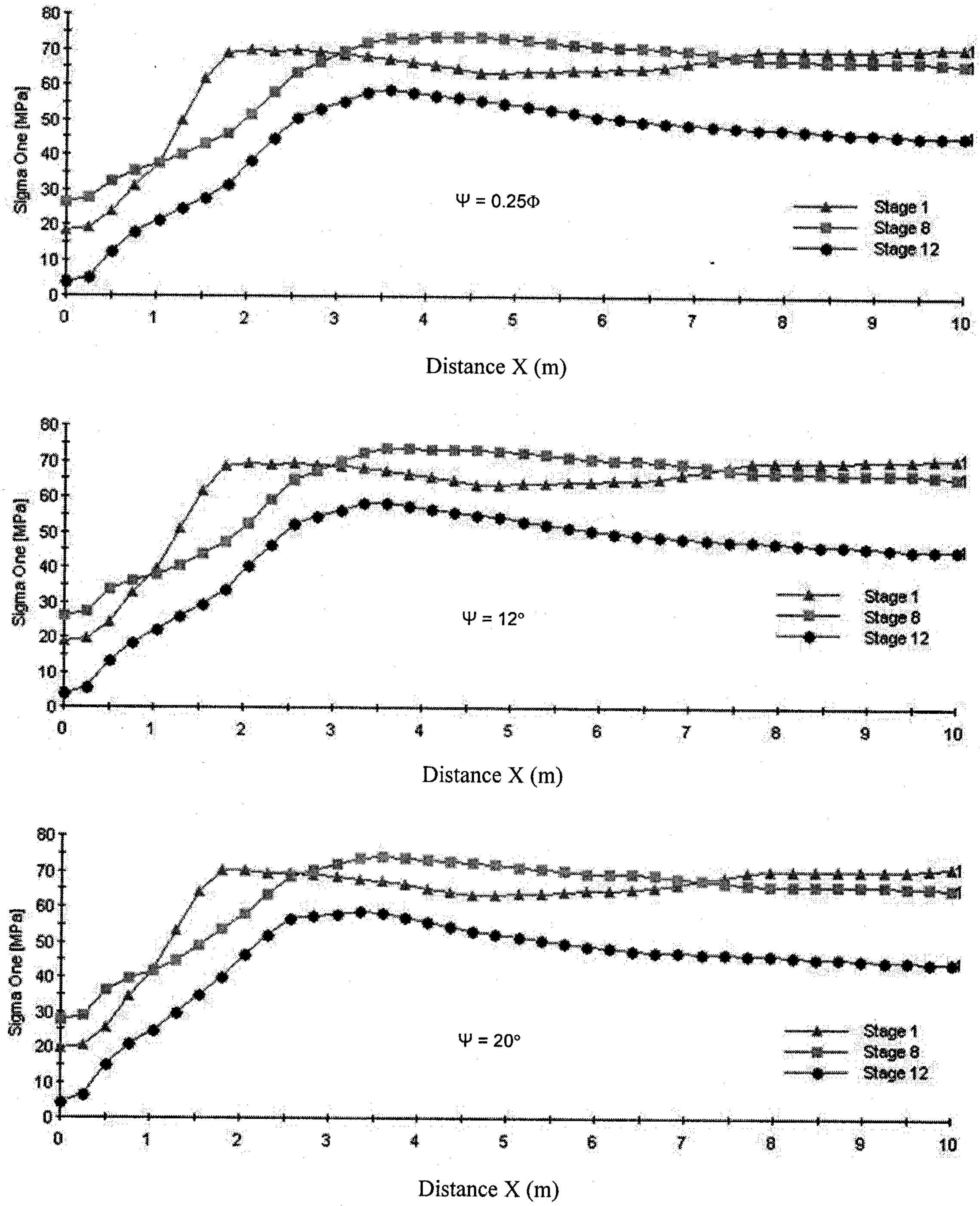

Figure 5. 16 Effect of dilation angle on major principal stress distribution --Model 3, 1, and 2 (top to bottom)

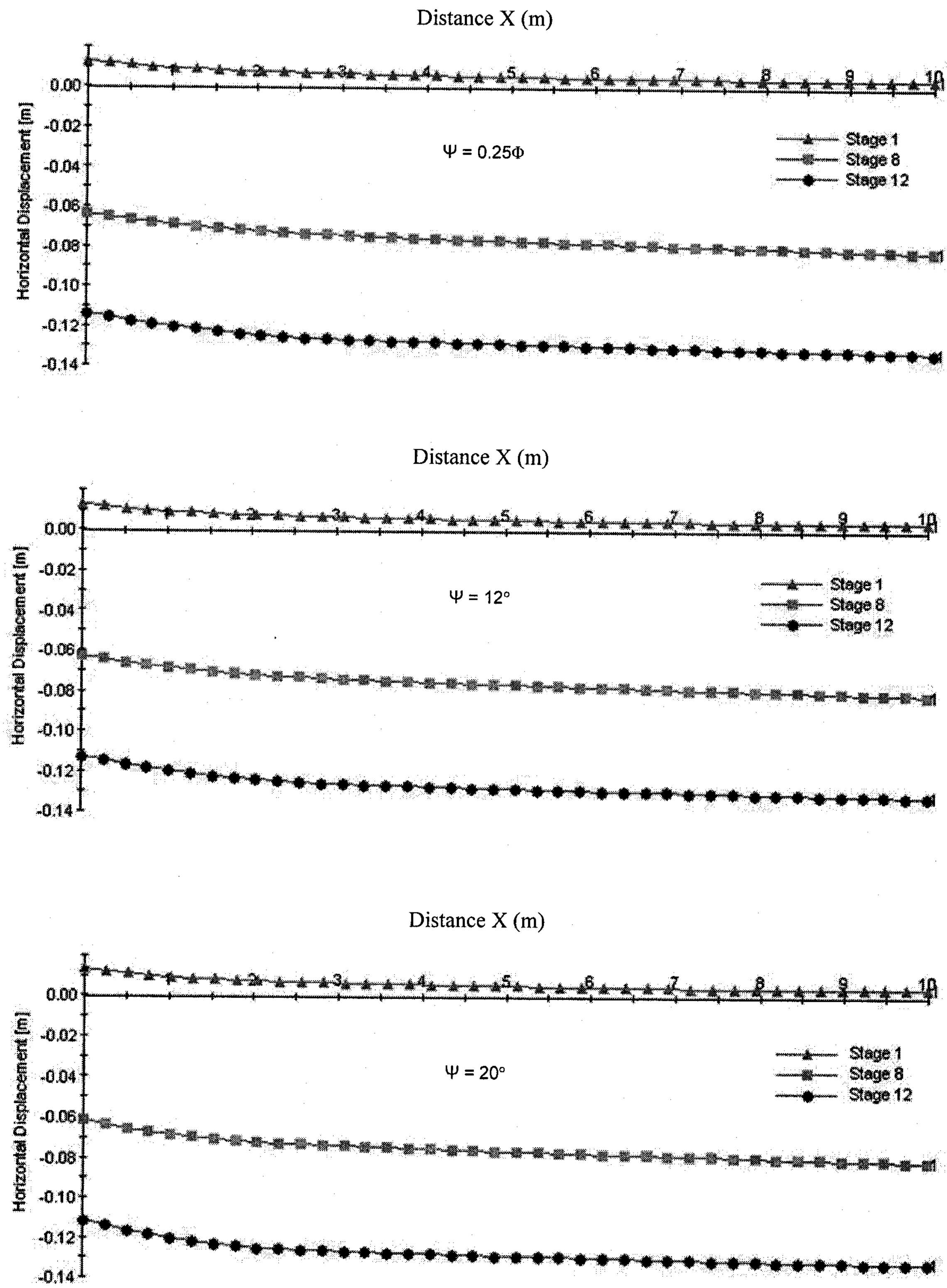

Figure 5. 17 Effect of dilation angle on horizontal displacements—Model 3, 2, and 1 (top to bottom)

5.8 Effect of drift shape

Model 1 and 31 (see Table 5.1) representing 3-centred arc drift (dimensions 4.5 m × 4.73 m) and rectangular drift (dimensions 4.5 m × 4.5 m), respectively, are used to examine drift shape effect in terms of development of yield zone, major principal stress distribution, and floor heave as well as roof sag at the distance of D = 50 m, mining depth of H = 2000 m, and dilation angle of $\psi = 12°$. In order to set up a comparable base for the usage of transportation and ventilation, these two geometric drift shapes are chosen to have the same cross sectional areas (20.25 m^2). Figures 5.18, 5.19, 5.20, 5.21, and 5.22 display the results of comparisons between Model 1 and Model 31.

Figure 5.18 shows the results of comparisons of floor heave and roof sag at centerline points of roof boundary and floor boundary from stage 1 to 13. It can be seen that the floor heave of Model 1 and 31 have exactly same response due to the same shape conditions on the floors, but the 3-centred arc roof centerline of Model 1 has 2-3 mm (10-15%) less sag than the flat roof (Model 31). It can also be noticed that backfilling stages (stages 3, 5, 7, 9, 11, and 13) do not have influence on floor heave and roof sag comparing with correspondingly preceding stope extraction stages (stages 2, 4, 6, 8, 10, and 12 correspondingly). The profiles in Figure 5.18 also prove previous discussions in sections 5.4.4 and 5.4.5 that the floor heave is monotonically increase and the roof sag is increase before stage 8 and retreat after stage 8.

Figure 5.19 demonstrates the results of yield zone comparisons at stage 1, 6, 8, and 12 for Model 1 and 31. It can be very easily to recognize that the 3-centred arc drift has more uniform yield zones around the haulage drift and less yield depths in the back at all stages. For example, at stage 8, 3-centred arc drift has 2.7 m maximum yield depth in the back compared to 3.5 m maximum yield depth in the back of rectangular drift; the latter is about 30% deeper than the former. Thus, 3-centred arc drift can improve roof yield condition.

Figure 5.20 illustrates the results of comparison of the major principal stress distribution or concentration for Model 1 and 31 at stage 1 (excavation of the haulage drift). It can be observed that 3-centred arc drift presents more uniform isotropic major principal stress flow lines, and more regular SCF contour lines, especially in the back. In this figure, the SCF = 1 lines also represent the isotropic major principal stress flow lines with $\sigma_1 = 51$ MPa. It can be seen that the lengths of the contour axes of 3-centred arc drift (horizontal and vertical) are about 10% shorter than rectangular drift, which implies the major principal stress disturbance after opening is lesser for 3-centred arc drift than rectangular drift.

Figure 5.21 compares the major principal stress distributions along left sidewall boundary (opposite the stope) starting from the floor to the roof at stage 1 and stage 8. It can be seen, at stage 1, the major principal stress near the roof corner of rectangular drift is about 3 times higher than the 3-centered arc drift. In both stages the 3-centred arc drift has more uniform stress distribution along the sidewall boundary.

Figure 5.22 exhibits the results of comparisons of major principal stress distribution along the roof boundary starting from left side to right side at stage 1 and stage 8. It is noted that the arced roof boundary has not only more uniform stress distribution, but most important (at stage 8) the arced roof maintains more than 3 MPa (minimum) compressive major principal stress while the flat roof (rectangular drift) presents lost of compressive major principal stress up to 3 m long. Lost of compressive major principal stress implies that the confinement diminishes and the roof is more collapse-prone.

Further studies of comparisons have shown the similar results for Models 2 and 32, Models 3 and 33, Models 4 and 34, Models 5 and 35, Models 6 and 36, Models 7 and 37, Models 8 and 38, Models 9 and 39.

As can be seen, 3-centred arc drift has following advantages over rectangular drift:

- More uniform yield zone;
- Less yield depth in the back;
- Less roof sag ratio;
- More uniform stress distribution and less stress concentration along sidewalls and roof;

- Less stress disturbance around the drift.

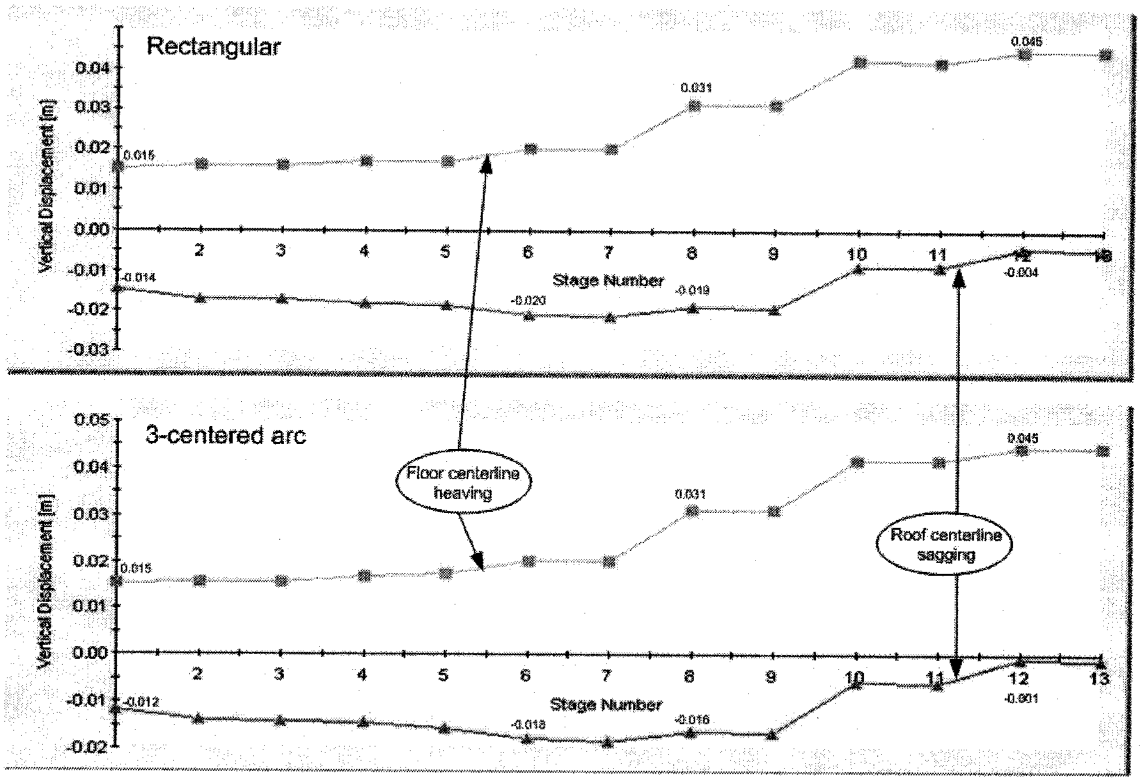

Figure 5. 18 Comparison of floor heave and roof sag at stage 1—Model 1 and 31

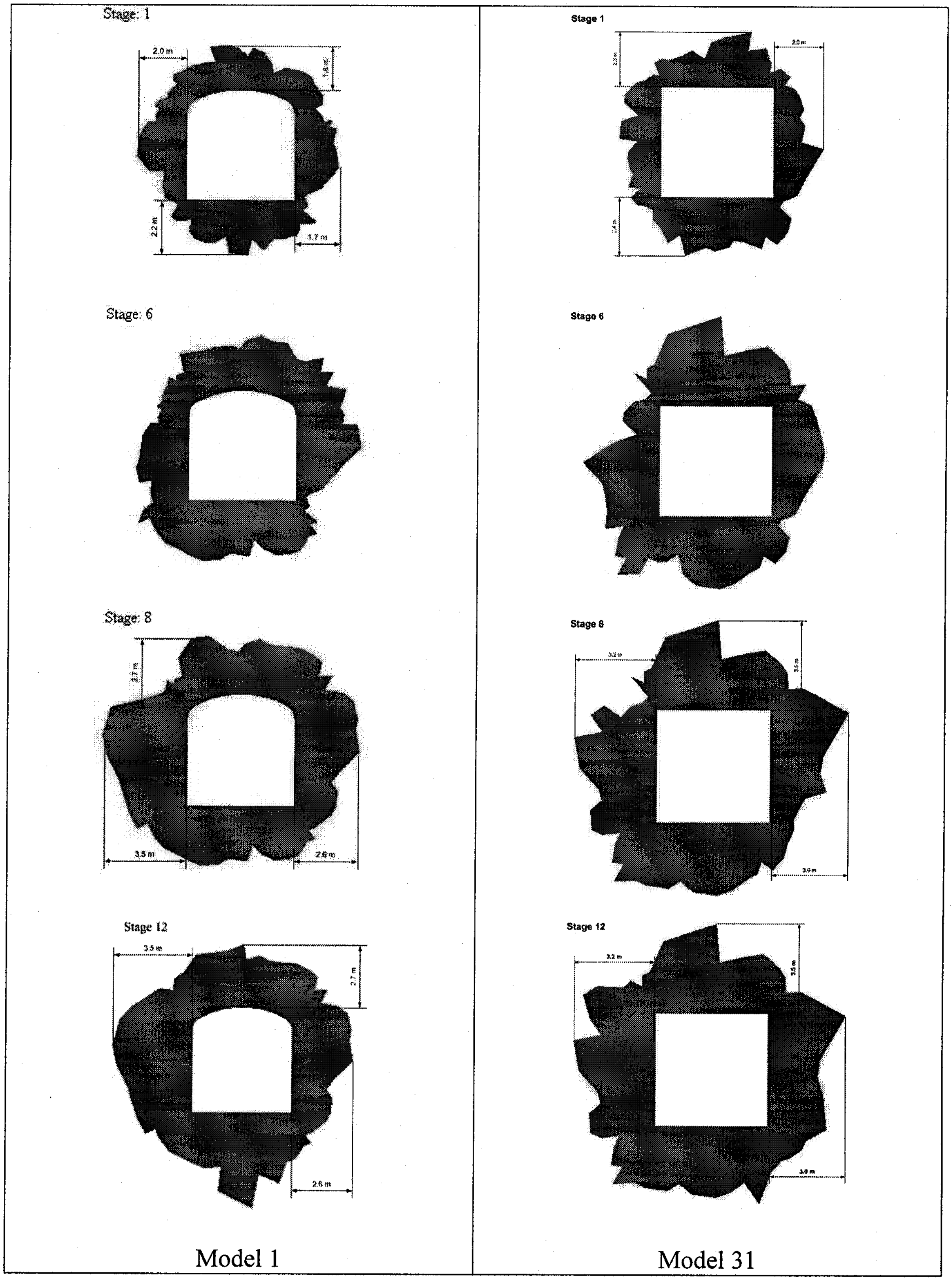

Figure 5. 19 Comparison of yield zones with different drift shapes

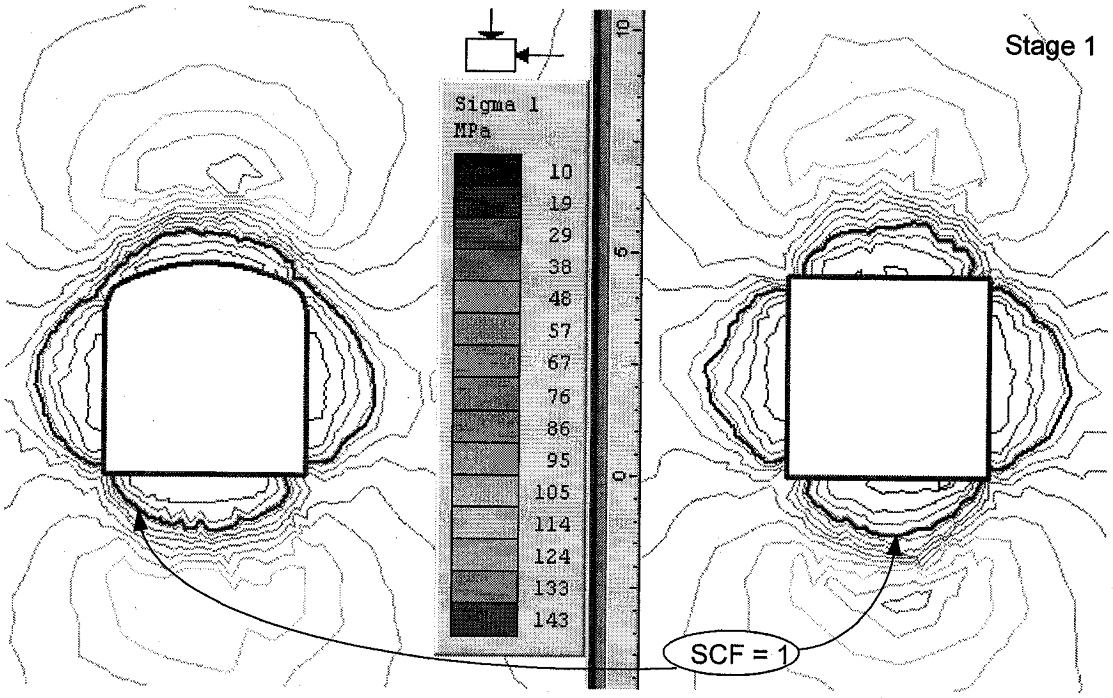

Figure 5. 20 Major principal stress distribution/concentration comparison at stage 1: Model 1 and Model 31

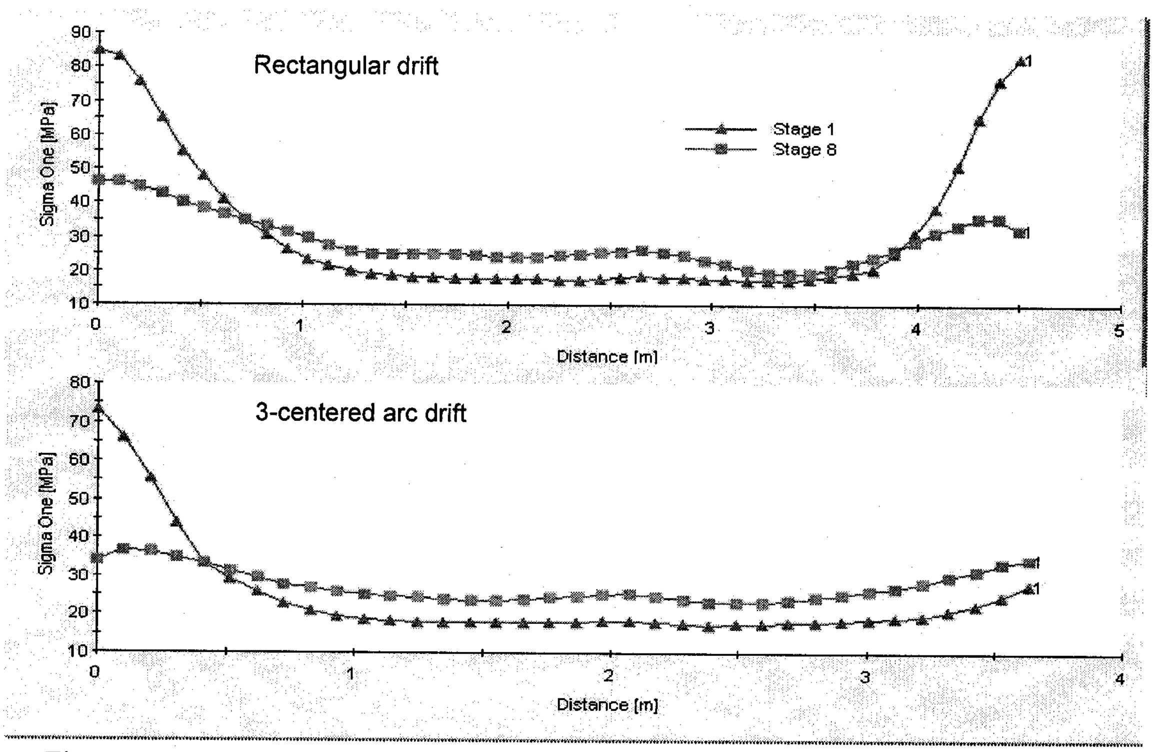

Figure 5. 21 Sidewall boundary stress distribution comparisons at stage 1 and 8: Model 1 and Model 31

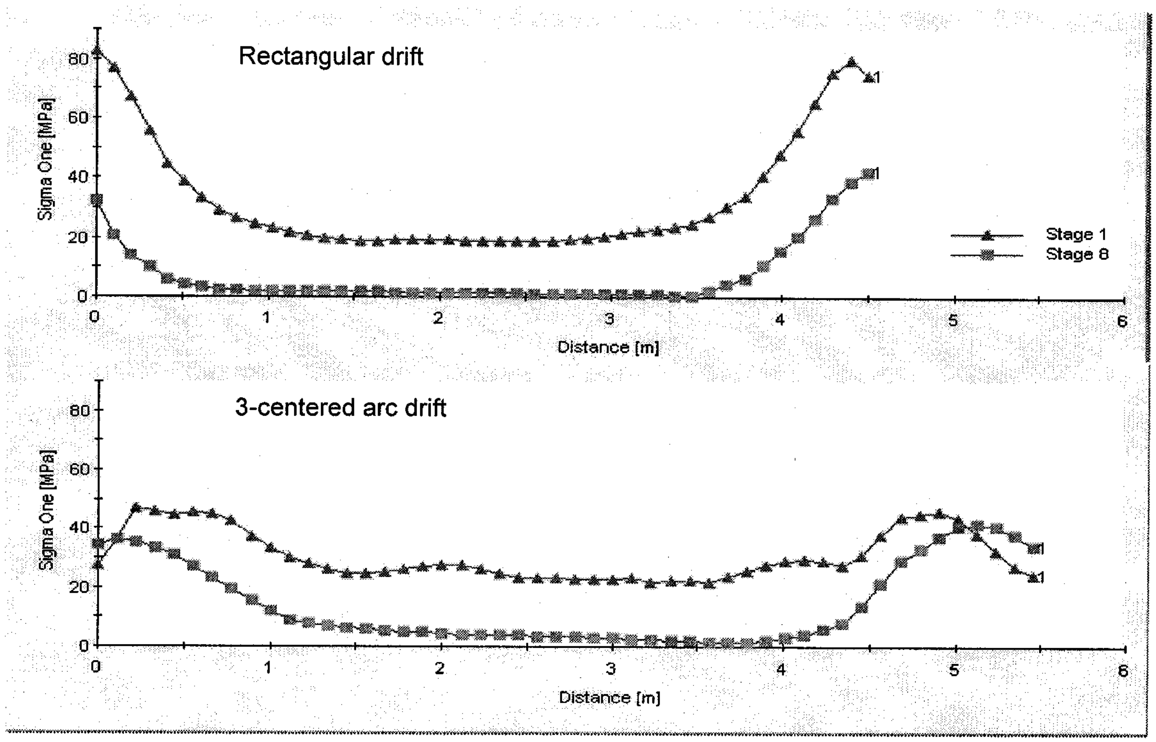

Figure 5. 22 Roof boundary stress distribution comparisons at stage 1 and 8 (Model 1 and Model 31)

5.9 Comparison of elastoplastic model to elastic model

Model 1 and 28 representing 3-centred arc drifts (Table 5.1) are used to compare the results of simulation from elastoplastic analysis and elastic analysis in terms of major principal stress distribution and SCF, roof sag and floor heave, as well as wall convergence at the mining depth of H = 2000 m and distance of D = 50 m. The results of comparisons are shown in Figures 5.23 to 5.25.

Figure 5.23 shows the results of major principal stress distribution and SCF contour lines of elastoplastic analysis vs. elastic analysis at stage 1. It can be noticed that:

- Two analyses have very different patterns of major principal stress distribution. The results of major principal stress distribution from elastoplastic analysis has more uniform pattern than elastic analysis. The SCF contour lines in the figure also represent the isotropic major principal stress flow lines. For example, SCF = 1 line represents σ_1 = 51 MPa isotropic major principal stress flow line.

- There exists a larger stress reduction zone surrounding the excavation (inside SCF < 1 zone) for elastoplastic analysis, in that after yielding the stress is redistributed. The maximum major principal stress located in the back with a value of 143 MPa. On the other hand, only two small regions near the middle of the sidewalls are in the state of stress reduction for elastic analysis, while the majority of other zones surrounding the opening are highly stress concentrated, especially near the roof and two floor corners with SCF > 3-5. The major principal stresses are in the range of 165-350 MPa (much exceed the material strength). It seems not in a realistic stress state.

- The results of elastoplastic analysis indicate that from the boundary to inside of the rock the major principle stresses are gradually increase in any directions with different gradients, after reach to peak values, then reduce to in situ stress (pre-excavation) state. But the results of elastic analysis give that in most directions the major principal stress distributions are from the highest values on the boundary to pre-mining (in situ) stress state except two small zones near the middle of the sidewalls.

Figure 5.24 shows the results of floor centerline heave and roof centerline sag of elastoplastic analysis vs. elastic analysis at all 13 stages. It can be seen that:

- Elastic analysis gives very small floor heave and roof sag magnitude than elastoplastic analysis. For example, at stage 1 the magnitude of floor heave is 4 mm from elastic analysis vs. 15 mm from elastoplastic analysis; at stage 12, the corresponding magnitude is 25 mm vs. 45 mm. For roof sag, elastic model shows the consecutive decreased magnitude of roof sag with mining activity progresses, and gives roof upwards results after stage 8 with maximum roof upwards magnitude of 19 mm at stage 12; while elastoplastic analysis gives the maximum roof sag magnitude of 20 mm at stage 8 and 0 mm at stage 12.

- The total effect of floor heave and roof sag (net height reduction of the drift) has less changes of magnitude with mining activity progression upwards for elastic analysis, but the total effect of floor heave and roof sag increases from stage 1 to stage 6 and decreases from stage 8 to stage 12 with mining activity progression upwards. It implies that the net height of the haulage drift is firstly shrinking then expanding with stoping upwards.

- The magnitude of total floor heave and roof sag effect from elastoplastic analysis (net reduction of height 27-55 mm) is 4.5-10 times greater than elastic analysis (net reduction of height 4-11 mm).

Figure 5.25 shows the wall convergence for both elastoplastic and elastic models at the middle points of sidewalls. It can be seen that:

- Elastic model gives smaller convergence magnitudes (0-15 mm) than the elastoplastic model (25-30 mm).

- The two models show the same trend that the drift is shifted towards the stope side from stage 6.

- The elastic model gives that the wall convergence diminished ($WCR = 0\%$) after stage 8, while elastoplastic model results that the wall convergence is still keeping some magnitude (WCR = 0.65%) with mining activity upwards.

Further model comparison studies for Models 10 and 29, Models 19 and 30 have shown similar results to Models 1 and 28.

From the above four aspects of comparisons, it can be concluded that:

- Elastoplastic analysis is more realistic than linear elastic analysis;

- Simulation results should be interpreted in quite different when only an elastic analysis is carried out.

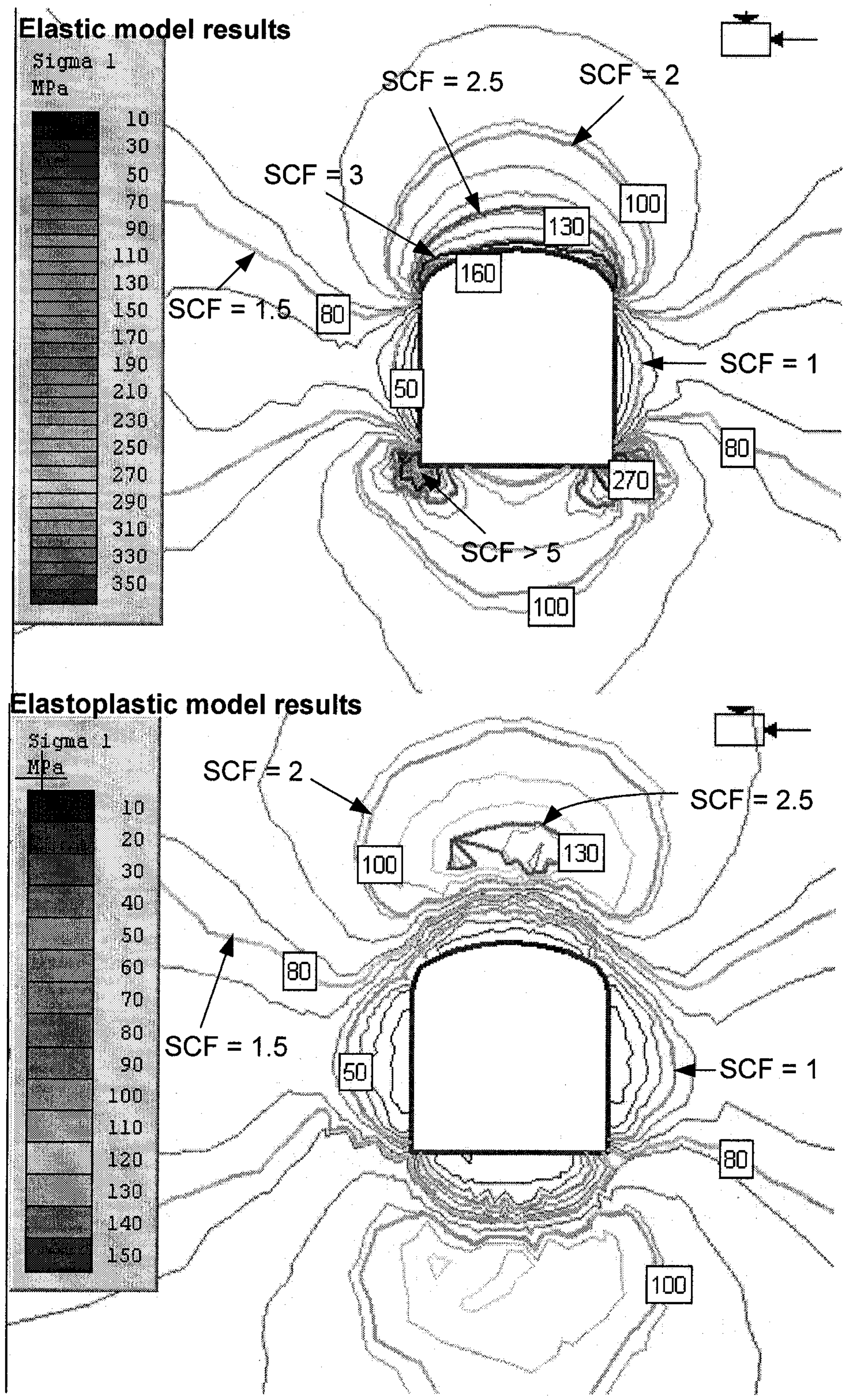

Figure 5. 23 Stress concentration comparison of linear and nonlinear model results at stage 1—Model 1 and 28

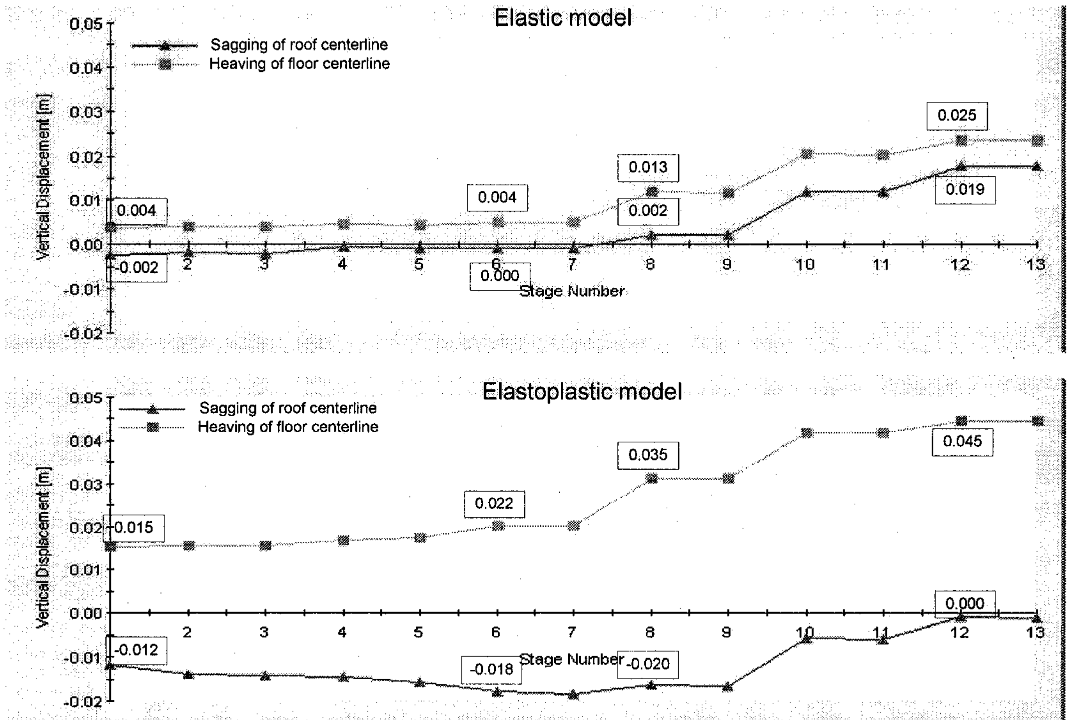

Figure 5. 24 Floor heave and roof sag comparison of linear and nonlinear model results at different stages—Model 1 and 28

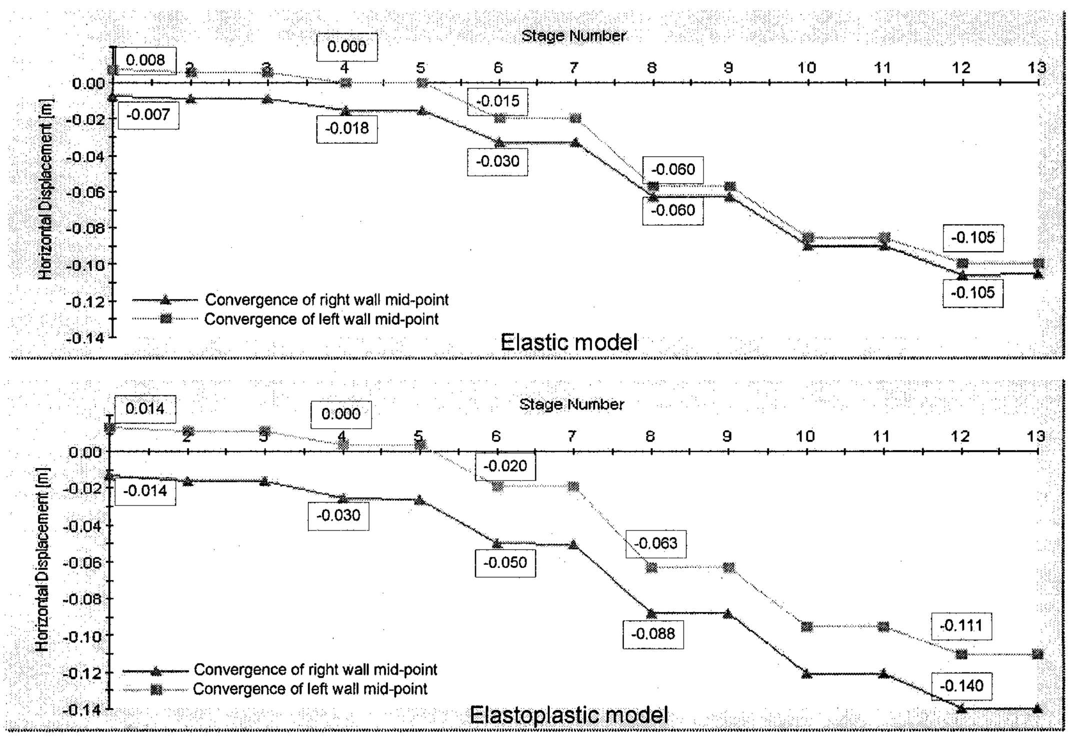

Figure 5. 25 Sidewall convergence comparison of linear and nonlinear model results at different stages—Model 1 and 28

Chapter 6 Conclusions

6.1 Summary and conclusions

The principal objective of this research is to better understand the stability of haulage drift during mining activities in sublevel stoping with delayed backfill in Canadian underground mines. Given that many rock materials exhibit elastic-plastic behaviour when subjected to mining-induced stresses, it is suggested that a good alternative for predicting the potential instability of underground openings and evaluating initial support design and feasibility study is to employ elastoplastic Mohr-Coulomb model combined with Drucker-Prager model and non-associated flow rule; together with combined tangent approach (Newton-Raphson method and Modified Newton-Raphson method) for obtaining the nonlinear solutions due to mining sequences, and unified initial strain (viscoplastic) method to generate right-hand (excavation) loads as an algorithm in solving finite element equations.

The characteristic models and the methodology for parametric study are intended to provide a measure for a site specific haulage drift and its support design. The characteristic models are based on data from Canadian mines, and also could be applied in similar mining environments.

The results of parametric studies of characteristic models can be summarized as follows.

- Stoping at the same level of haulage drift (stage 8) is the most critical stage for the stability of the haulage drift. It is a major contributor to the yield zone extending and it causes significant shifting of the drift towards the stope.

- Stoping or mining activities affect the stability of haulage drift. It dominates the stress redistribution patterns around the drift. With the progression of mining activity, the long-axis of stress reduction zone and the stress concentrated spots tend to rotate clockwise, from 0° (relative to horizontal) at drift opening (stage 1) to 120°-150° at stage 12 representing the last stope excavation. As the distance *D* becomes shorter, the stress rotation is more pronounced.

- Floor heave increases constantly with mining activity; the maximum value is reached at the last stope extraction (stage 12).
- As the distance to the stope decreases, the yield zone increases, with more yield development toward the stope.
- Increasing the mining depth causes the stress relaxation zone increase, but the maximum yield depth is not significantly changed.
- All backfilling and lower level stoping insignificantly affect yield zone around the haulage drift.
- Drift shape influences the stability of haulage drift. 3-centred arch roof and rounded boundary has the advantage of easing stress concentration, reducing yield depth in the back, and maintaining better stability state.
- Dilation angle is a sensitive parameter to yield depth. When dilation angle increases, the yield depth decreases.
- Elastoplasticity model gives more realistic interpretations for major principal stress distribution and magnitude of displacement than traditional linear elastic model. The results of elastoplasticity analysis show that there exists a larger stress reduction zone around the excavation boundary. From the boundary to inside the rock mass, the magnitude of major principal stress increases to some maximum value, then decreases to in situ stress state. While the linear elastic analysis gives maximum stress values are on the boundary and from the boundary decreases to in situ stress state.
- Both elastoplastic model and elastic model show the same trend of drift shifting toward the stope side as mining activity progress.

6.2 Recommendations

Based on this study, the following general recommendations can be made.

- It is important to use elastoplastic nonlinear analysis for the study of the stability of underground mine openings. The results, in terms of stresses and displacements, are radically different. This is particularly true when the mine opening under study is in the vicinity of an ongoing mining activity. Stress redistribution and yield zones continue to evolve as mining activity progresses

- The distance between the mine opening under study and the mining activity is one of the most critical parameters that affect the stability of the mine opening. Such distance representing the zone of influence of the mining activities should be carefully selected and assessed in the preliminary mine design stages.

- For the range of parameters and mine setting studied, the 3-centre arc shaped drift appears to be more stable than a rectangular drift of equal area in that the former provides more uniform confinement around the drift, less roof sag and lesser extent of yield zones

6.3 Suggestion for Future Work

The following are suggestions for future work to extend the present research work:

- The model parametric study was conducted with a series of nonlinear numerical models, which are based on typical Canadian mine conditions. An extension of this work could be to apply this methodology to examine specific mine sites. The result of such case studies could lead to validated stability guidelines for the mine and can be used for future mine planning.

- Cross cuts are as important as haulage drifts in the underground mining operation in terms of their functionality during the life of stope production. Therefore, equal attention should be paid to their stability. This can be done by adopting a similar approach to that presented in this thesis. The analysis however will have to be carried out as 3-dimensional as the junction of the draw point with the cross cut drift is the portion that is most prone to instability during production.

- The present work can be extended to derive dedicated stability graphs for mine haulage drifts in a fashion similar to the empirical methods such as the Q-tunnel index method and the Stability Graph Method.

References

Andrieux, P., & Simser, B. (2001). Ground-Stability-Based Mine Design Guidelines at the Brunswick Mine. In Hustrulid, W. A. and Bullock R. L. (Eds), *Underground Mining Methods--Engineering Fundamentals International Case Studies*. Littleton, CO: Society for Mining, Metallurgy, and Exploration

Archibald, J. F., & Hassani, F. (1998). *Mine Backfill 1998* (Vol. Special 48): CIM.

Arjang, B. (1991). Pre-mining Stresses at some Hard Rock Mines in the Canadian Shield. *CIM Bulletin, Vol.84*(945), 80-86.

AtlasCopco. (2005). Sublevel Open Stoping. http://www.atlascopco.com/Websites/RDE/website.nsf/$All/3545BB612F06FB8B4125674D004AC13E?OpenDocument.

Barton, N., Lien, R., & Lunde, J. (1974). Engineering Classification of Jointed Rock Masses for the Design of Tunnel Support. *Rock Mechanics: Journal of the International Society for Rock Mechanics, Vol.6*, pp. 189-236.

Bieniawski, Z. T. (1973). Engineering Classification of Jointed Rock Masses. *Transation of the South African Institution of Civil Engineers, Vol.15*, pp. 335-344.

Blake, W. (1971). Destressing test at Galena Mine Wallace, IDAHO. *AIME Contennial Annual Meeting*.

Brown, E. T., & Hoek, E. (1978). Trends in relationships between measured in-situ stresses and depth. *International Journal of Rock Mechanics and Mining Science & Geomechanics Abstracts, 15*(4), 211.

Carnavas, P. (2000). Mining geomechanics I, Post Peak Behaviour of Rock Samples in Uniaxial Compression (Course notes): University of Quensland, Australia.

Chan, S. L., & Chui, P. P. T. (2000). *Non-linear static and cyclic analysis of steel frames with semi-rigid connections*. Amsterdam ; New York ; Oxford :: Elsevier.

Chen, W. F., & Han, D. J. (1988). *Plasticity for structural engineers*. New York :: Springer-Verlag.

Cividini, A. (1992). Constitutive Behavior and Numerical Modeling. In *Comprehensive Rock Engineering*. Vol.1, pp.395-426.

Clough, R. W. (1960, Sept.). *The Finite Element Method in Plane Strain Analysis.* Paper presented at the Proc. 2nd ASCE Conf. Electronic Computation, Pittsburgh, PA.

Cormeau, I. C. (1975). Numerical stability in quasi-static elasto-visoplasticity. *Int J Numer Methods Eng, 9*(1), pp 109-127.

Coulomb, C. A. (1776). Essai sur une application des règles des maximis et minimis à quelques provblèmes de statique relatifs à l'architecture. *Mem. Acad., 5*(7).

Creus, G. J. (1986). *Viscoelasticity : basic theory and applications to concrete structures.* Berlin ; New York :: Springer-Verlag.

Cundall, P. A. (2005). Constitutive Models: Theory and Background. In *FLAC 5.0 User's Manual*: Itasca Consulting Group, Inc.

Deere, D. U., Hendron Jr., F. D., Patton, F. D., & Cording, E. J. (1967). Design of Surface and Near Surface Construction in Rock. In C. Fairhurst (Ed.), *Failure and Breakage of Rock* (pp. 237-302): Society of Mining Engineers of AIME.

Diederichs, M. S. (1999). *Instability of Hard Rockmasses: The Role of Tensile Damage and Relaxation.* University of Waterloo.

Drucker, D. C., & Prager, W. (1952). Soil Mechanics and Plastic Analysis or Limit Design. *Quarterly of Applied Methematics, 10*, pp 157-165.

Feder, G. (1979). Ultimate State Design of Deep Tunnel Under Anisotropic Conditions. *3rd International Conference on Numerical Methods in Geomechanics*, pp 621-625.

Gomez-Hernandz, J., & Kaiser, P. K. (2003). Modeling Rock Mass Bulking around Underground Excavations. Paper presented at the *ISRM 2003-Technology Roadmap for Rock Mechanics*, South African Institute of Mining and Metallurgy, Vol.1, pp.389-395.

Grant, D. & Dekruijff, S. (2000) Mount Isa mines-1100 Orebody-35 Years On. In: Australasian Institute of Mining and Metallurgy. *MassMin 2000.* Australia: Australasian Institute of Mining and Metallurgy Publication,Vol.1, pp. 591～600.

Griffiths, D. V. (1988). An iterative method for plastic analysis of frames. *Comput Struct, 30*(6), pp 1347-1354.

Griffiths, D. V., & Willson, S. M. (1986). An explicit form of the plastic matrix for Mohr-Coulomb material. *Commun. Appl. Numer. Methods, Vol.2*, pp. 423-529.

Hajiabdolmajid, V. R., & Kaiser, P. K. (2003). Brittleness of Rock and Stability Assessment in Hard Rock Tunneling. *Tunneling and Underground Space Technology, Vol. 18*, pp. 35-48.

Hajiabdolmajid, V. R., Kaiser, P. K., & Martin, C. D. (2002a). Mobilization of Strength in Brittle Failure of Rock-In Laboratory vs. In Situ. Paper presented at the *Proceedings of the 5th North American Rock Mechanics Symposium*, Toronto, Canada, pp. 227-234.

Hajiabdolmajid, V. R., Kaiser, P. K., & Martin, C. D. (2002b). Modelling Brittle Failure of Rock. *Int. J. of Rock Mech. Min. Sci., Vol.39*, pp. 731-741.

Hallbauer, D. K., Wagner, H., & Cook, N. G. W. (1973). Some Observations Concerning the Microscopic and Mechanical Behaviour of Quartzite Specimens in Stiff, Triaxial Compression Tests. *Int. J. Rock Mech. Min. Sci., Vol.10*, pp. 713-726.

Hamrin, H. (2001). Underground Mining Methods and Applications. In *Underground Mining Methods: Engineering Fundamentals and International Case Studies.* edited by Hustrulid, W. A. and Bullock, R. L. Littleton, CO: Society for Mining, Metallurgy, and Exploration.

Henning, J. G. (1998). *Ground Control Strategies at the Bousquet 2 Mine.* McGill University, Montreal.

Herget, G. (1987). Stress Assumptions for Underground Excavations in the Canadian Shield. *International Journal of Rock Mechanics and Mining Science & Geomechanics Abstracts, 24*(1), pp. 95-97.

Hoek, E. (1983). Strength of Jointed Rock Masses. *23rd Rankie Lecture, Géotechnique, Env., Vol.33*(3), pp 187-223.

Hoek, E. (1994). Strength of Rock and Rock Masses. *ISRM News Journal, Vol.2*(2), pp. 4-16.

Hoek, E., & Brown, E. T. (1980a). Empirical Strength Criterion for Rock Masses. *J. Geotech. Engng Div., ASCE, Vol.106* ((GT9)), pp. 1013-1035.

Hoek, E., & Brown, E. T. (1980b). Underground Excavations in Rock. Paper presented at the *Instn. Min. Metall.*, London, England.

Hoek, E., & Brown, E. T. (1988). The Hoek-Brown Failure Criterion—a 1988 update. Paper presented at the *15th Canadian Rock Mech. Symp*, Dept. Civil Engineering, University of Toronto, Toronto, Canada, pp. 31-38.

Hoek, E., & Brown, E. T. (1997). Practical Estimates of Rock Mass Strength. *Intnl. J. Rock Mech. & Mining Sci. & Geomechanics Abstracts, Vol.34*(8), pp. 1165-1186.

Hoek, E., Carranza-Torres, C., & Corkum, B. (2002). Hoek-Brown Failure Criterion—2002 Edition. Paper presented at the *Proc. 5th North American Rock Mechanics Symposium and the 17th Tunnelling Association of Canada Conference—NARMS-TAC*, University of Toronto Press, Toronto, Canada, pp. 267-271.

Hoek, E., Kaiser, P. K., & Bawden, W. F. (1995). *Support of Underground Excavations in Hard Rock*: AA Balkema: Rotterdam.

Hoek, E., Marinos, P., & Benissi, M. (1998). Applicability of the Geological Strength Index (GSI) Classification for Very Weak and Sheared Rock Masses: The Case of the Athens Schist Formation. *Bull. Engg. Geol. Env., Vol.57*(2), pp.151-160.

Hoek, E., Marinos, P., & Marinos, V. (2004). Rock Mass Characterisation for Molasses. *Int. J. Rock Mech. Min. Sci.*

Hoek, E., Wood, D., & Shah, S. (1992). A Modified Hoek-Brown Criterion for Jointed Rock Masses. Paper presented at the *Proc. Rock Characterization, Symp. Int. Soc. Rock. Mech.: Eurock'92*, London, Brit. Geotech. Soc., pp. 209-214.

Kaiser, P. K., Diederichs, M. S., Martin, C. D., Sharp, J., & Steiner, W. (2000). Underground Works in Hard Rock Tunnelling and Mining. Paper presented at the Keynote Lecture. *GeoEng2000 Conference.* Technomic Publishing Co., Melbourne, Australia, pp 841-926.

Lade, P. V., & Jackobsen, K. P. (2002). Incrementalization of a Single Hardening Constitutive Model for Frictional Materials. *Int. J. Numer. Anual. Meth. Geomech, Vol.26*, pp. 647-659.

Lorig, L., & Varona, P. (2004). Numerical Analysis. In D. C. Wyllie & C. W. Mah (Eds.), *Rock Slope Engineering: Civil and Mining* (4th ed.), pp. 218-244. London: Spon Press.

Martin, C. D. (1997). 17th Canadian Geotechnical Colloquium: The Effect of Cohesion Loss and Stress Path on Brittle Rock Strength. *J. Can Geotech, Vol.36*(1), pp.136-151.

Martin, C. D., Kaiser, P. K., & Creath, D. R. (1999). Hoek-Brown Parameters for Predicting the Depth of Brittle Failure around Tunnels. *J. Can Geotech, Vol.36(1)*, pp.136-151.

Mitri, H. S. (2005). Course Notes: Department of Mining, Metals and Materials Engineering, McGill University.

Mitri, H. S., & Hassani, F. P. (1988). Nonlinear Finite Element Analysis of Mine Roadway Arch Support Systems. *Computers & Structures, Vol. 29*(No. 3), pp. 335-364.

Mitri, H. S., & Tang, B. (2003). Stability Analysis of Mine Opening with e-z tools. Paper presented at the *4th Int. Conf. on Comp. Appl. in the Minerals Industry (CAMI)*, Calgary, Alberta, Canada.

Obert, L., Duvall, W. I., & Merril, R. H. (1960). Design of Underground Openings in Competent Rock. *Bulletin: US Bureau of Mines, 587*, pp. 9.

Owen, D. R. K., & Hinton, E. (1980). *Finite Element in Plasticity: Theory and Practice.* Swansea, U. K.: Pineridge Press Limited.

Pariseau, W. G. (1980). Finite Element Method Applied to Cut and Fill Mining. *Proceedings of the Conference on the Application of Rock Mechanics to Cut and Fill Mining.*

Pariseau, W. G. (1992a). Applications of Finite Element Analysis to Mining Engineering. In *Comprehensive Rock Engineering.* Vol. 1, pp. 491-522.

Pariseau, W. G. (1992b). Rock Mechanics. In *SME Mining Engineering Handbook, 2nd Edition.* Vol. 1, pp. 829-847.

Potvin, Y. (1988). Empirical Open Stope Design in Canada. Unpublished PhD, Dept. of Mining and Mineral Processing, University of British Columbia.

Ranken, R. E., & Ghaboussi, J. (1975). Tunnel Design Considerations: Analysis of Stresses and Deformations around Advancing Tunnels. *Report UILU-ENG 75-2016.*

Rao, S. S. (1989). *The Finite Element in Engineering*: Pergamon Press, U. K.

Smith, I. M., & Griffiths, D. V. (2004). *Programming the finite element method.* Hoboken, NJ :: Wiley.

Syvestre, M. (1999). *Heating and Ventilation Study of Inco's Creighton Mine.* McGill University, Montreal.

Tesarik, D. R., Seymour, J. B., & Yanske, T. R. (2003). Post-Failure Behavior of Two Mine Pillars Confined with Backfill. *International Journal of Rock Mechanics and Mining Sciences, 40*(2), 221.

Traina, L. A. (1983). Experimental Stress-Strain Behaviour of a Low Strength Concrete under Multiaxial States of Stress, *Technical Report AFWL-TR-82-92.* Kirtland Air Force Base, New Mexico: Air Force Weapons Laboratory.

Turner, M. J., Clough, R. W., Martin, H. C., & Topp, L. J. (1956). Stiffness and Deflection Analysis of Complex Structures. *A. Aeron Sci., 23*(9), pp 805-823.

Vermeer, P. A. (1998). Non-associated Plasticity for Soils, Concrete and Rock. In H. J. Herrmann (Ed.), *Physics of Dry Granular Media.* Vol. 350, pp. 163-196: Kluwer Academic Publishers.

Zienkiewicz, O. C., & Cormeau, I. C. (1974). Viscoplasticity, Plasticity and Creep in Elastic Solids: A Unified Approach. *Int. J. Numer. Methods Eng., 8*, pp 821-845.

Zienkiewicz, O. C., & Humpheson, C. (1977). Viscoplasticity: A generalized Model for Description of Soil Behaviour. In *Desai C. & Christian J. T. (eds.), Numerical Methods in Geotechnical Engineering.* London: McGraw-Hill.

Zienkiewicz, O. C., & Taylor, R. L. (1989). *The finite element method* (4th ed.). London ; New York: McGraw-Hill.

Zienkiewicz, O. C., Valliappan, S., & King, I. P. (1968). Elasto-plastic Solutions of Engineering Problems: Initial Stress Finite Element Approach. *Int. J. Num. Meth. Engng., Vol.1*, pp. 75-100.